University of Alberta

Properties and growth of thin films produced by Glancing Angle Deposition

by

Brian Allan Dick ©

A thesis submitted to the Faculty of Graduate Studies and Research in partial fulfillment of the requirements for the degree of Doctor of Philosophy.

Department of Electrical and Computer Engineering

Edmonton, Alberta
Fall, 2003

National Library
of Canada

Acquisitions and
Bibliographic Services

395 Wellington Street
Ottawa ON K1A 0N4
Canada

Bibliothèque nationale
du Canada

Acquisisitons et
services bibliographiques

395, rue Wellington
Ottawa ON K1A 0N4
Canada

Your file Votre référence
ISBN: 0-612-87962-3
Our file Notre référence
ISBN: 0-612-87962-3

The author has granted a non-exclusive licence allowing the National Library of Canada to reproduce, loan, distribute or sell copies of this thesis in microform, paper or electronic formats.

L'auteur a accordé une licence non exclusive permettant à la Bibliothèque nationale du Canada de reproduire, prêter, distribuer ou vendre des copies de cette thèse sous la forme de microfiche/film, de reproduction sur papier ou sur format électronique.

The author retains ownership of the copyright in this thesis. Neither the thesis nor substantial extracts from it may be printed or otherwise reproduced without the author's permission.

L'auteur conserve la propriété du droit d'auteur qui protège cette thèse. Ni la thèse ni des extraits substantiels de celle-ci ne doivent être imprimés ou aturement reproduits sans son autorisation.

Canadä

University of Alberta

Library Release Form

Name of Author: Brian Allan Dick

Title of Thesis: Properties and Growth of Thin Films Produced by Glancing Angle Deposition

Degree: Doctor of Philosophy

Year this Degree Granted: 2003

Permission is hereby granted to the University of Alberta Library to reproduce single copies of this thesis and to lend or sell such copies for private, scholarly or scientific research purposes only.

The author reserves all other publication and other rights in association with the copyright in the thesis, and except as herein before provided, neither the thesis nor any substantial portion thereof may be printed or otherwise reproduced in any material form whatever without the author's prior written permission.

a

June 24, 2003

It was the best of times, it was the worst of times, it was the age of wisdom, it was the age of foolishness, it was the epoch of belief, it was the epoch of incredulity

Charles Dickens, Tale of Two Cities

University of Alberta

Faculty of Graduate Studies and Research

The undersigned certify that they have read, and recommend to the Faculty of Graduate Studies and Research for acceptance, a thesis entitled *Properties and growth of thin films produced by Glancing Angle Deposition* submitted by Brian Allan Dick in partial fulfillment of the requirements for the degree of Doctor of Philosophy.

Dr. Michael Brett

Dr. Mark Freeman

Dr. Christopher Backhouse

Dr. Jeremy Sit

Dr. Al Meldrum

Dr. Garry Tarr
(External affiliation)

June 23, 2003
Date

To my parents

Abstract

Developing and commercializing applications for thin film devices fabricated by glancing angle deposition (GLAD) cannot be done without knowledge of the thin film's fundamental growth mechanisms and properties. This thesis presents data and analysis characterizing substrate preparation, growth mechanisms, and magnetic properties for films produced using the GLAD technique. Electron beam lithography (EBL) and plastic embossing are shown as viable processes to fabricate the seeding structures required to grow periodic GLAD pillars, oblique columns and helices. The key GLAD deposition parameters of flux incidence angle (α) and substrate rotational speed ($d\varphi/dt$) are qualitatively studied. It is found that GLAD structures are more readily formed when $\alpha < 87^\circ$, and best optimized when $\alpha < 85^\circ$. Al, Bi, Si, and SiO_2 GLAD films grown at $d\varphi/dt$ ranging from 0.0043 RPM through 42 RPM show that amorphous and high temperature materials follow the standard GLAD transition of oblique columns to helices to posts with increasing rotational speed. Crystalline and low-temperature materials are found to grow non-standard structures due to a decrease in adatom diffusion length with increasing substrate rotation speed. Data also suggests that for these latter materials, a poor microstructure is formed when the value for $d\varphi/dt$ lies between that required for the formation of either a helix or pillar. It is hypothesized that this is due to the occurrence of a non-equilibrium shadowing condition at the substrate surface. Evidence is presented confirming the ratio of pillar diameter to the average separation of surviving columns [s/δ (or s/p in periodic films)] – a descriptor for the onset of columnar competition – as an important factor governing GLAD film growth. Helices are observed to degenerate more readily to pillars at higher seed separations as $\Delta\alpha$ increases, where the aperiodic structure separation, s, appeared to govern the position of

the transitional region between pillar and helical growth. Finally, magnetic properties of GLAD films are studied and hysteresis measurements of several microstructure types are presented.

Acknowledgements

Like most things in life, this thesis could not have been completed in isolation.

First and foremost, I'd like to thank my supervisor, *Dr. Michael Brett*, for allowing me the freedom to pursue my own interests, and never turning down a request to enjoy the cuisine in "exotic" lands.

The Natural Sciences and Engineering Council of Canada (NSERC), Alberta's Informatics Circle of Research Excellence (iCORE), and the occasional scholarship and grant: for allowing me to focus on my research rather than my tummy.

The GLAD research group: for offering tips, diversions lying from and between the heights of mountains to the depths of the ocean, and, yes, even friendship. With time's progress, may we not drift too far apart.

Dr. Doug Vick: for offering measured criticism and guidance as my work progressed.

George Braybrook: the amazing SEM photographer, who so deftly revealed that hidden landscape which so demanded study.

Herbert Dexel, and the rest of the machine shop guys: who deciphered my hand-waving explanations, and produce workable devices.

Dr. Tom Smy: for both developing 3D-FILMS, and subsequently tweaking the growth parameters to give insight on how the GLAD film evolves

Martin O. Jensen, and particularly Miro Belov: for producing on short order the numerous EBL patterns I needed for growing the periodic GLAD structures shown in this thesis.

Of course, *my family* who have always supported me in my academic pursuits, and, more importantly, in life's other journeys which have changed me even more profoundly.

And last, but not least, *Raymond...* What can I say? For almost 4 yrs you have listened and suffered through my complaints and bitterness when research turned sour, and my droning when things turned around. Through it all, you have been my rock. And though our paths diverge now, may we be like ships sailing a meridian, rather than the opposite edges of a cube...

Table of Contents

Chapter 1 – Introduction 1
  1.1 History 1
  1.2 Motivation 1
  1.3 Scope 4

Chapter 2 – A Primer on Glancing Angle Deposition (GLAD) 6
  2.1 Film Nucleation and Growth 6
  2.2 Deposition at Oblique Flux Incidence 7
  2.3 Glancing angle deposition (GLAD) 9
    2.3.1 The Transition from Oblique to Glancing Incidence 9
      2.3.1.1 Beginnings 9
      2.3.2.2 Tait's Rule 10
      2.3.1.3 Substrate rotation 12
      2.3.1.4 Simple GLAD Structures 15
    2.3.2 Advanced GLAD structures 17
      2.3.2.1 Advanced Control System 17
      2.3.2.4 Other Advanced GLAD Structures 18
      2.3.2.5 Periodic Structures 19
  2.4 Simulation software 21

Chapter 3 – Substrate Preparation 26
  3.1 Introduction 26
  3.2 Electron-beam lithography 26
    3.2.1 Background 27
    3.2.2 1st Generation EBL Arrays 28
    3.2.3 2nd Generation EBL Arrays 29
    3.2.4 3rd Generation EBL Arrays 30
  3.3 Plastic Embossing 30
    3.3.1. Background 31
    3.3.2. Production of the seeds 31
    3.3.3. GLAD fabrication parameters 32
    3.3.4. Findings 33
    3.3.5. Conclusions from Plastic Embossing Study 34

Chapter 4 – Flux Incidence Angle and Substrate Rotation 35
4.1 Introduction 35
4.2 Investigation on Flux Angle Dependency 36
4.2.1 Film Morphology 36
4.2.2 Derived Expression for Film Density at Glancing Incidence 39
4.2.3 Conclusions from Flux Incidence Angle Study 41
4.3 Investigation oF substrate rotation and GLAD microstructures 42
4.3.1 Background 42
4.3.2 Experimental set-up 43
4.3.3 Observations 44
4.3.3.1 Si and SiO_2 44
4.3.3.2 Bismuth 47
4.3.3.3 Aluminum 49
4.3.4 Discussion 51
4.3.4.1 3D-FILMS modeling of Substrate Rotation and Adatom Mobility. 51
4.3.4.2 Crystallography and its effect on GLAD Microstructures 54
4.3.6 Conclusions of Substrate Rotation Study 56

Chapter 5 – Competition and Related Growth Mechanics 57
5.1 Background 57
5.1.1 A case for α-dependent film density 58
5.1.2 Constant Film Density and the Evolution of Pillar Microstructures 59
5.2 3D Simulation Work and Findings 62
5.2.1 Investigations on Film Density 62
5.2.2 Investigations on Pillar Diameter 64
5.2.3 Investigations on Flux Angular Distribution 65
5.2.4 Investigations on Seed Period 67
5.2.5 Conclusions 67
5.3 Experimental 68
5.3.1 Set-up 68
5.3.1.1 Evaporation 69
5.3.1.2 Sputtering 70
5.3.2 Investigations on Flux Angular Distribution 72
5.3.2.1 Growth of Aperiodic GLAD Films by Sputtering 72
5.3.2.2 Growth of Periodic GLAD films by Sputtering 73

5.3.3 Investigations on Competitive Growth 76
5.3.4 Investigations on Pillar Diameter 77
5.4 Conclusions 81

Chapter 6 – Study on the Magnetic Properties of GLAD films 83
6.1 Introduction 83
6.2 Theory and Principles 84
6.3 Film Characterization 85
6.3.1 GLAD Fabrication Parameters 85
6.3.2 Film Morphology 86
6.3.3 Magnetic Properties 87
6.4 Conclusions 90

Chapter 7 – List of Recommendations and Conclusion 92
7.1 List of recommendations 92
7.1.1 Fundamental Studies 92
7.1.1.1 Rotation 92
7.1.1.2 Density and Growth 94
7.1.1.3 Evolution of Helical and Oblique structures 94
7.1.2 Alternative seed lattice materials and fabrication processes 94
7.1.2.1 Poly(dimenthylsiloxane) mediums 95
7.1.2.2 Laser (Optical) Interference Lithography (LIL) 97
7.2 Conclusion 99
7.3 Final Word 101

Appendix A – Glossary 102

Appendix B – List of Publications 107
B.1 Referred journal publications 107
B.2 Conference proceedings/Submitted Articles to Refereed Journals 107
B.3 Conference Presentations 108
B.4 Other publications 108

References 109

List of Tables

Table 3.1. Comparison of Thermionic and Field Emission processes.............27
Table 4.1. Deposition parameters for substrate rotation study.....................44
Table 5.1. Adjusted parameter for 3D-FILMS simulations 62
Table 5.2. Effective angular flux distribution for the experimental set-up 71
Table 6.1. Investigations/Applications of selected GLAD film properties 83
Table 6.2. Film Deposition parameters for study on magnetic properties.......85
Table 6.3. Measurements of magnetic saturation and coercivity 89

List of Figures

Figure 1.1. Bifurcation and Shadowing at Oblique Incidence.. 3
Figure 1.2. Evolution of Oblique Columns. 4

Figure 2.1. Oblique Deposition of Thin Films. 8
Figure 2.2. The Tait model...11
Figure 2.3. Tait's predicated and measured column angle.........................11
Figure 2.4. SIMBAD simulator of film growth over a trench........................14
Figure 2.5. The GLAD system schematic. 18
Figure 2.6. The film growth geometry for aperiodic and periodic films.. 20
Figure 2.7. Examples of periodic GLAD morphologies grown at $\alpha=85^o$..........21
Figure 2.8. 3D-FILMS simulations of different GLAD film morphologies.........24
Figure 2.9. Plan view of both real films and 3D-FILMS simulations. 24
Figure 3.1. Processing steps for producing seed arrays by EBL...................28
Figure 3.2. EBL seed pattern. 29
Figure 3.3. Processing steps for producing embossed patterns in epoxy 32
Figure 3.4. Epoxy nanostructures before and after GLAD film growth 33

Figure 4.1. Simultaneous deposition of GLAD films at varying α 37
Figure 4.2. Effect of changing α on the GLAD film morphology 38
Figure 4.3. Normalized Density Functions...41
Figure 4.4. Measured and predicted film densities for SiO_2.........................41
Figure 4.5. Gearbox used to step up and down $d\varphi/dt$.................................44
Figure 4.6. Films of SiO_2 grown at various rotational speeds 46
Figure 4.7. Average deposition rates vs. rotational speed for Si and SiO_2......46
Figure 4.8. Films of Bi grown at various rotational speeds 48
Figure 4.9. Average deposition rates vs. rotational speed for Bi...................49
Figure 4.10. Films of Al grown at various rotational speeds.........................50
Figure 4.11. Average deposition rates vs. rotational speed for Al 51
Figure 4.12. 3D-FILMS simulation of a high mobility GLAD film 53
Figure 4.13. Effect of substrate rotational speed on adatom diffusion length 53
Figure 4.14. Angle of incident flux relative to the surface normal................54

Figure 5.1. Effect of competition on aperiodic GLAD films. 57
Figure 5.3. Evolution of the pillar diameter and separation. 60
Figure 5.4. 3D-FILMS simulations of density 63
Figure 5.5. Simulated periodic posts at progressive stages of growth 64
Figure 5.6. Effect of increasing the angular flux distribution width 66
Figure 5.7. Effect of increasing periodicity 67
Figure 5.8. Illustration of the deposition geometry for sputtered GLAD films .. 70
Figure 5.9. Aperiodic tungsten films grown by sputtering 73
Figure 5.10. Periodic tungsten films grown by sputtering at α=82.5° 74
Figure 5.11. Periodic tungsten films grown by sputtering at α=86.0° 75
Figure 5.12. Evaporated and sputtered periodic GLAD films 76
Figure 5.13. Pillar diameter and pillar count density for periodic SiO_2 films.... 78
Figure 5.14. Pillar diameter and pillar count density for periodic W films....... 79

Figure 6.1. The "major" hysteresis loop 84
Figure 6.3. Hysteresis curves for several GLAD microstructures.................. 88
Figure 6.4. Crystal analysis of the randomly seeded cobalt posts................. 90

Figure 7.1. Seed layer produced by PDMS 96
Figure 7.2. EBL-produced mould for production of seed layers in PDMS 97
Figure 7.3. Laser Interference Lithography (LIL) set-up. 98

List of Symbols

α	The angle of incident flux at the substrate measured relative to the substrate normal.
$\Delta\alpha$	A measure of the angular distribution in flux incident at the substrate.
a	The normalized column separation as determined by Tait's Rule.
β	Columnar angle measured relative to the substrate normal.
χ	Magnetic susceptibility
δ	The diameter of columns grown using the GLAD technique.
D	Surface diffusivity constant
H	Magnetization field vector
H_c	Magnetic coercivity
φ	Rotation angle about an axis located at the substrate centre, and parallel to its normal.
$d\varphi/dt$	Substrate rotation speed about the φ axis
κ	Ratio of the thickness of a film grown at an oblique incidence, α, and a film grown at normal incidence (i.e. $t(\alpha) / t(\alpha=0)$)
L	Adatom diffusion length
μ_o	Magnetic susceptibility
M	Magnetization vector
M_s	Saturation magnetization
P_c	Ambient chamber pressure. For evaporation, P_c is less than 10^{-5} torr (10^{-3} Pa), and typically on the order of 10^{-6} torr (10^{-4} Pa) for refractory metals. For sputtering, P_c is on the order of 10^{-3} to 10^{-2} torr (0.1 to 1.0 Pa)
p	The period of seed elements used to grow periodic GLAD structures.
θ	Angle between the film normal and the incident flux
r	deposition rate, radius of the shielding ring used in the sputtered film deposition apparatus
ρ	Thin film density
s	The "average" separation of randomly grown GLAD columns.

τ	Measure of the adatom burial rate ($\tau = \frac{1}{d\varphi/dt}$)
T	Substrate or film surface temperature
T_m	Melting temperature of the source material
t	time, film thickness
t_{ring}	Thickness of shielding ring used in the sputtered film deposition apparatus
x	Separation between adjacent plates in the multi-flux angle set-up
y	Separation between the flux source and substrate – referred to also as the throw distance

Chapter 1 – Introduction

1.1 HISTORY

The art and science of thin film technology has been in existence for several millennia. For most of this period, the technology, in the form of gold beating, was used to create ornaments [1]. For example, leaf samples from Luxor dating to the Eighteenth Dynasty (1567-1320 B.C.) measured 0.3 microns in thickness [2]. It is thought that the modern revolution in thin film development and application began in 1857 [3] when Faraday exploded metal wires in an inert atmosphere fabricating the first evaporated thin films. These and subsequent films were found to have properties that either did not exist in, or were significantly enhanced from, the bulk form of the evaporated material. Over time, the "state-of-the-art" for vacuum deposition techniques has expanded immensely from these early experiments. Typically, film depositions can now take place at extremely low pressures ($<10^{-10}$ torr or $1.3\text{x}10^{-8}$ Pa) using a variety of processes including physical [electron-beam evaporation, thermal evaporation (the progeny of Faraday's early experiments), molecular beam epitaxy, and sputtering with its process variants] and chemical [chemical vapour deposition, sol-gel] techniques. The development and application of such analysis tools as scanning electron microscopy (SEM), Auger spectroscopy, and atomic force microscopy (AFM) has helped encourage the modern, wide-spread application of these films in such fields as anti-reflection coatings, sensors, packaging, and, most significantly, micro- and nanoelectronics.

1.2 MOTIVATION

This thesis presents work related to the fundamental characterization of films grown using glancing angle deposition (GLAD). This advanced film deposition technique utilizes physical vapour deposition at extremely oblique flux incidence and was originally developed by Kevin Robbie (now at Queens University) and Dr. Michael Brett at the University of Alberta [4-7].

GLAD allows the user *in situ* control over substrate rotation and flux incidence angle to fabricate a variety of thin film microstructures including helices, pillars, and chevrons with either random or regular periodicity on a substrate surface. Because of their easily controlled morphology, GLAD films have been proposed and studied for applications in a number of diverse fields such as high-density magnetic storage media and unique magnetic structures [8-10], photonics [11] and liquid crystal displays [12, 13], chemical and humidity sensors [14], catalysis media [15], thermal barrier coatings [16], micro-resonators [17], and field emission displays [18].

Arguably, what has been lacking from these application studies is an in-depth and concentrated research program with the intent of characterizing the fundamental growth mechanisms and properties of these unique films. These studies are essential as the regime in which GLAD films are deposited is known to be extremely sensitive to growth conditions. For example, Vick *et al.* recently categorized the evolution of an obliquely grown SiO_2 film through its growth cycle [19]. Although the initial nucleation of these films is similar to that deposited at normal incidence, extreme self-shadowing at the substrate surface ensures that only local high points of surface relief capture the majority of incident flux. The anisotropic nature of shadowing maintains voiding between columns, which is amplified as the film grows. As long as columns remain unshadowed, their surface advances in a fractal-like manner, due to bifurcation of nanocrystallite growth (See Figure 1.1).

At a larger size scale, this growth appears to occur in a manner reminiscent of Huygen's principle of geometrical optics; namely, shadowing from neighbouring columns becomes significant only at points away from the column apex. The broad tops of columns evolve as if they are growing with constant velocity along the surface normal [20, 21]. Because of these growth mechanisms, columns exhibit a gradual lateral fanning, where adjacent columns can merge and form elongated structures along parallel axes (see Figure 1.2).

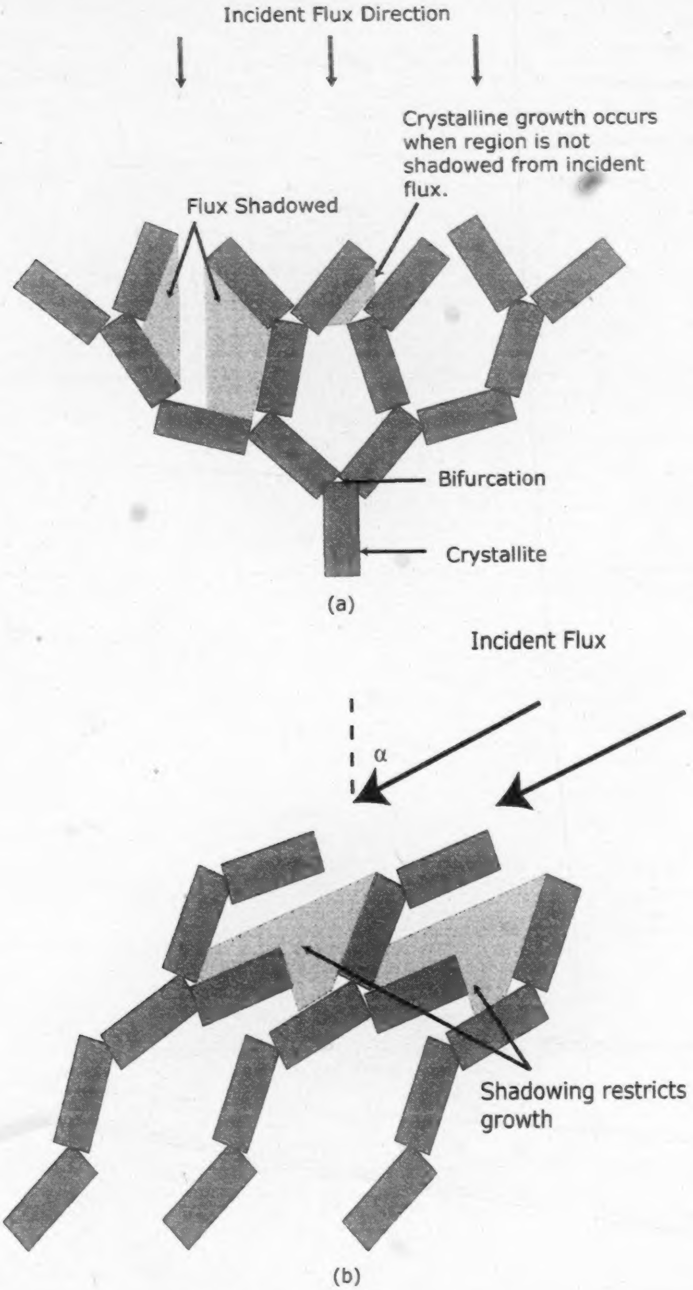
Incident Flux Direction
Crystalline growth occurs when region is not shadowed from incident flux.
Flux Shadowed
Bifurcation
Crystallite
(a)
Incident Flux
α
Shadowing restricts growth
(b)

Figure 1.1. Bifurcation and Shadowing at Oblique Incidence. To idealize the bifurcation process, the growth of the oblique column is illustrated as consisting of rectangular blocks representing individual crystallites. Each crystallite is presumed to bifurcate at its apex unless incident flux is restricted on that surface. In (a), the oblique column is observed looking down on the substrate, where normal incident flux encourages film to fan out perpendicular to its incoming direction. In (b), the film growth is observed parallel to the substrate plane. In this instance, the extreme shadowing from neighbouring columns, due to the non-normal flux angle, restricts fanning perpendicular to the incident flux direction.

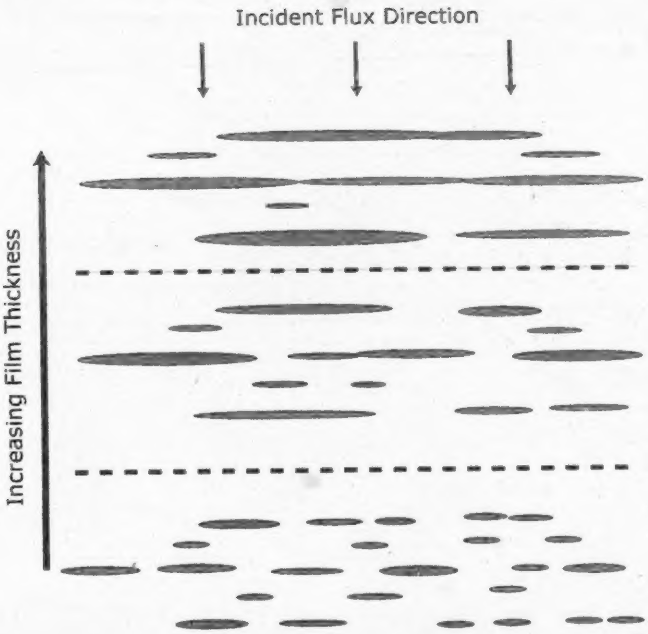

Figure 1.2. Evolution of Oblique Columns. Each panel in this illustration (separated by a dashed line) represent a plan view for a film at increasing thickness. Columns begin as nuclei that grow laterally due to anisotropic shadowing at the substrate surface. This mechanism, enhanced at extremely oblique incidence, encourages structures to elongate (and eventually join with their neighbours) along an axis perpendicular to the vapour flux direction, and, due to flux shadowing, restrict growth between the resulting columnar bands (Adapted from Figure 2 in Ref. [19]).

Fanning out of oblique columns is just one example of where understanding the characteristics of film growth at glancing incidence is important. Other examples include film density (examined in Chapters 2 and 5) and structure morphology (Chapter 4); both of these properties are significantly affected within the "glancing incidence" regime (i.e. $\alpha > 80^{o}$). Developing and commercializing GLAD applications cannot be made without knowledge of these fundamental growth properties. It is this gap in current GLAD research that this thesis intends to help fill, by both expanding the parameter space within which the growth mechanisms for GLAD films are understood, and providing a framework to guide future investigations.

1.3 SCOPE

Although a basic understanding of the GLAD technique is assumed in this thesis, Chapter 2 provides a brief primer to the history and basic processes underlying the growth of GLAD microstructures, including a background on the simulation tools that will be used in the thesis. Chapter 3 summarizes the two techniques – electron beam lithography and plastic embossing – that were used to fabricate the seed arrays used in my thesis research. The fundamental growth studies conducted are covered in Chapter 4 and 5. These two chapters have been split into "simple" and "advanced" growth mechanisms for GLAD films. Chapter 4 reports on the effects of flux incidence angle and substrate rotation on GLAD film morphology, while Chapter 5 shows research on the (interrelated) effects of flux distribution angle, seed period, and columnar competition on the growth of both random and periodic arrays of GLAD microstructures. In Chapter 6, observations on the magnetic properties of GLAD films are summarized.

To assist the reader, a List of Symbols has been included at the front of this thesis, and a Glossary of selected terms in Appendix A at its end.

Finally, some note should be made on nomenclature:

- Flux incidence angle, α, and column angle, β, are defined relative to the substrate normal. This definition is consistent with the majority of GLAD literature and the original paper defining the tangent rule [22]. Using these definitions, the flux angles used with the GLAD technique are typically in the regime of 75° or higher: GLAD films can be classified as "dense" for $75^\circ<\alpha<80^\circ$, "porous" for $80^\circ<\alpha<85^\circ$, and "super-porous" for $\alpha>85^\circ$ [13].

- The term "aperiodic films" refers to GLAD structures deposited using the standard deposition process (i.e. on a flat substrate). The term "periodic films" refers to those GLAD films deposited on a pre-defined seed layer.

Chapter 2 – A Primer on Glancing Angle Deposition (GLAD)

2.1 FILM NUCLEATION AND GROWTH[†]

A standard thin film process evaporates or sputters a source material onto the substrate such that the flux arrives at normal incidence (α=0°). Incident atoms efficiently transfer their kinetic energy to the lattice and become loosely bound "adatoms". These adatoms diffuse over the surface, exchanging energy with the lattice or adsorbed species, until they are either desorbed (through re-evaporation or sputtering), or become trapped at low-energy lattice sites. These incorporated adatoms subsequently readjust their positions within the lattice (referred to as bulk diffusion). Hence, films initiate as small nuclei randomly distributed on the substrate. Further flux deposition, coupled with the natural tendency of the system to minimize its total surface area (or chemical potential), causes the small nuclei to increase in size, and agglomerate into islands, eventually forming a continuous, dense, solid film [1, 23, 24].

Films deposited in this fashion exhibit columnar structure. The morphology of these columns is dependent on the conditions under which the structure was formed, and is particularly sensitive to the ambient chamber pressure (P_c), and the ratio of substrate temperature (T) to the melting point of the source material (T_m). This sensitivity should not be a surprise as the processes of desorption, surface diffusion, and bulk diffusion identified above are energy related. Each is dependent on characteristic diffusion and sublimation activation energies, and hence has a magnitude scaling directly as T/T_m.

To help understand and describe the resulting film morphology, structure zone models (SZMs) have been built based on P_c and T/T_m ([25, 26], see also [1] for a summary). The earliest of these zone models was proposed by Movchan and Demchishin and was based on almost ten years of study on thick coatings (0.3 to 2 mm) of Ti, Ni, W, ZrO_2, Al_2O_3, and Fe deposited at high rates (200 to 3000 Å/sec) and normal incidence by electron beam evaporation. In addition to the energy related processes above, their work concluded that an additional mechanism governing film growth is also present: atomic shadowing. Inherently, this mechanism does not depend on the ambient energy, but is rather a geometrical effect, determined solely by the surface roughness and the collimation of incoming flux. Atomic shadowing can be present even when films are deposited at normal incidence, resulting in a typical thin film having a density less than its bulk value. Taking both the energy and shadowing mechanisms into account, the Movchan and Demchishin SZM represents film growth as a function of T/T_m in terms of three zones:

[†] This chapter has been partially excerpted from my invited chapter to the *Encyclopedia of Nanoscience and Nanotechnology* entitled "NanoFabrication by Glancing Angle Deposition", H.S. Nalwa Ed. and is used with the permission of American Scientific Publishers, Los Angeles (2003).

Zone I ($T/T_m < 0.3$) – Film structure consists of tapered crystals with domed tops. Atomic shadowing effects predominate in this regime.

Zone II ($0.3 < T/T_m < 0.5$) – Columnar grains are separated by distinct, dense, intercrystalline boundaries. Surface diffusion is the primary growth mechanism in this temperature range.

Zone III ($0.5 > T/T_m$) – Consists of equiaxed grains with a bright surface. The structures and properties of Zone III films correspond to a fully annealed metal. Bulk diffusion is the primary growth mechanism.

The Movchan and Demchishin SZM, expanded by Thorton [26] to include the background argon pressure present during sputtering, will be used to help classify the films shown in this thesis.

2.2 DEPOSITION AT OBLIQUE FLUX INCIDENCE

The growth of a thin film becomes more intricate when the substrate is no longer perpendicular to the arriving flux. In this case, the non-normal flux incidence angle (α) magnifies the intrinsic shadowing mechanism on the substrate surface. SZMs do not explicitly account for variations in the arriving flux incidence angle, although they do exhibit the effect to a limited degree. Zone I morphology is observed to extend into higher T/T_m ratios at the higher argon pressure present during sputtering [26]. This observation is the direct consequence of the broadening of the angular distribution of vapour flux due to randomizing collisions with the background gas [5]. Obliquely deposited films exhibit considerable changes in their properties, which have orientation dependence. Film stress and density are altered (usually diminished) which introduces anisotropic dependencies into the thermal, electrical, magnetic, and optical properties of the film [27, 28]. Although early researchers did not have access to the necessary tools to directly observe thin film morphologies at sub-optical wavelengths, the origin of these anisotropic properties were speculated to be the result of a shadowing mechanism: "the area behind the crystallite is left vacant because it is in the crystallite's shadow" [29]). These speculations have now generally been accepted as accurate, and are graphically illustrated in the comparison between a normal and obliquely deposited film shown in Figure 2.1.

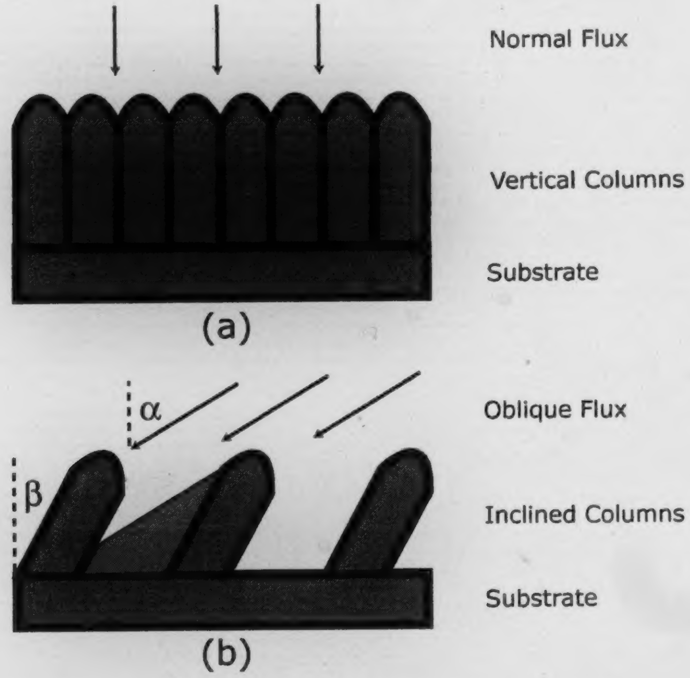

Figure 2.1. Oblique Deposition of Thin Films. In a standard thin film deposition process, vapour flux arrives normal to the substrate forming a columnar microstructure (a). If the substrate is tilted relative to the incident flux, the vapour arrives at an oblique angle (α) to the substrate normal. Under limited adatom diffusion, adatom shadowing at the substrate surface (shown as red in the lower panel) results in a porous film with columns inclined at an angle, β, towards the vapour source (b).

At oblique incidence, the columnar morphology of the film is tilted towards the direction of incoming flux. The angle of column growth, β, is a monotonically increasing function of α, where $\beta<\alpha$. This function depends not only on α, but also other deposition parameters including the choice of material, the flux angle angular distribution ($\Delta\alpha$), chamber pressure (P_c), substrate temperature, and source to substrate separation (y). The tangent rule, derived empirically by Nieuwenhuizen and Haanstra [22] and shown in Equation 2.1, adequately describes the relationship between α and β for $\alpha<60°$ [30, 31].

$$\tan(\alpha) = 2\tan(\beta) \qquad [2.1]$$

Some researchers, notably Dirks and Leamy [32], have attempted to explain the tangent rule with varying degrees of success. Generally, however, "it is good to state that this rule does not have any physical meaning, it is merely a description which seems to fit a number of measurements" [33].

2.3 GLANCING ANGLE DEPOSITION (GLAD)

2.3.1 The Transition from Oblique to Glancing Incidence

2.3.1.1 Beginnings

Before 1996, most studies on oblique deposition had taken place at $\alpha<60^o$, where the tangent rule is known to be reasonably accurate [33]. Given the tangent rule prediction that $\beta\rightarrow 90^o$ as $\alpha\rightarrow 90^o$ (see Figure 2.2(a)), the amount of film grown at higher flux incidence would be expected to be extremely small [34]. Hence, little interest was taken in the "glancing flux incidence" regime. There were a few exceptions to this rule, including an early paper by Holland (1953) [35] investigating the reflectivity of aluminum deposited at a flux incidence of $\alpha\leq 85^o$, and a paper by Cohen (1961) [36] who experimented with the magnetic anisotropy of films deposited at a "grazing angle" of $\alpha\sim 83°$. Although lacking extensive imaging of the film surface through such tools as scanning electron microscopy, the highly oblique incidence of their depositions leads me to believe that their films were the first to exhibit the highly porous structure characteristic of glancing angle deposition (GLAD) morphology.

Much later, a few studies [30, 37] continued this earlier work by examining the nature of the film morphology at these higher incidence angles. These researchers found that the shadowing mechanism was enhanced, resulting in highly separated columns and a resulting increase in film porosity. Contrary to the tangent rule, however, they found that the columnar angle did not approach

90° with increasing flux incidence, but rather reached a maximum somewhat less (typically β=60°).

2.3.2.2 Tait's Rule

A simple geometrical approach showed that α and β could be related for evaporated thin films grown at high incidence angles (α>60°) and limited surface diffusion [30]. This argument was based on observations of ballistic deposition models, which were found to closely resemble real thin film behaviour. Hence, it was believed that a discrete particle, shadowing-based expression for columnar angle could be derived [38]. The expression [30], referred to as Tait's rule and shown in Equation 2.2, assumed deposition on hemispherically topped columns (the most energetically favourable geometry for low temperature depositions). The centre of the column portion receiving flux was then used to determine the direction of growth. A comparison between Tait's rule and the tangent rule is shown in Figure 2.2(a).

$$\beta = \alpha - \sin^{-1}\left(\frac{1-\cos\alpha}{2}\right) \qquad [2.2]$$

Neither material effects, such as faceting, nor variance in column size (both are observed in real films) were considered in Tait's analysis. Nevertheless, this equation has been shown to predict $\beta(\alpha)$ well for Fe and MgF_2 films and correctly reproduced the general observation that β approaches a value less than 90° as $\alpha \rightarrow 90°$ [34].

Further measurements on columnar angle were made using cobalt, silicon dioxide, titanium, and titanium dioxide as source materials. The results of these experiments are shown in Figure 2.3. To minimize discrepancies between film deposition cycles, several substrates were held at different angles in the chamber so that each series could be grown simultaneously. The maximum distance between the outer substrate sample and the axis normal to the melt was kept to less than 10% of the effective separation between the substrates and source. Thus, the resulting variation between incident flux at the central and outer sample was limited to 0.5% and so was considered negligible. These series show that for α>82° the trend for columnar angle follows Tait's rule.

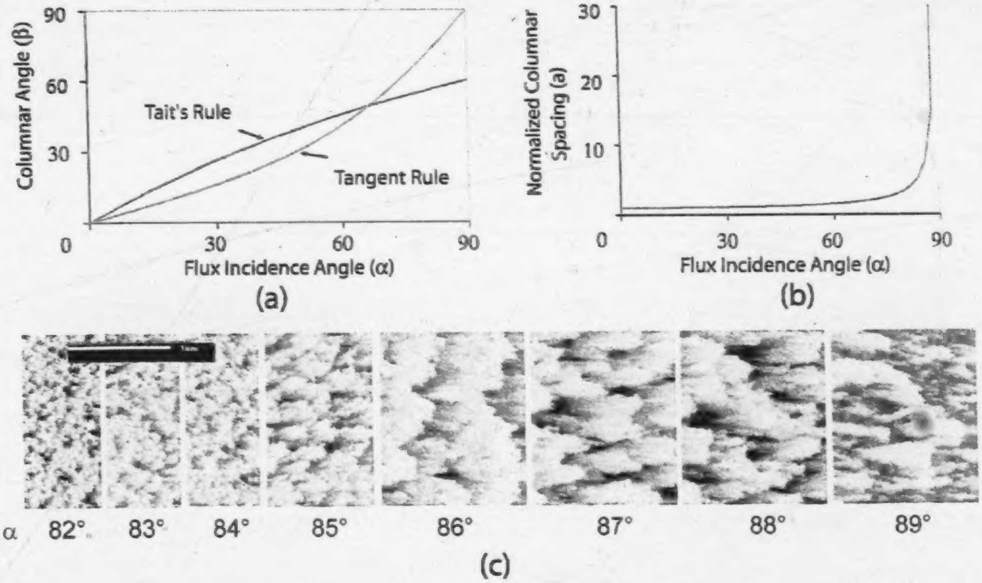

Figure 2.2. The Tait model can be used to predict the effects of deposition angle, α, on both (a) the column angle, β, and (b) the normalized columnar spacing, a. A comparison between Tait's rule and the tangent rule is shown in panel (a). Note that the β curve describing Tait's rule reaches a value of 60º as α→ 90º. In the lower panel, plan views of titanium films deposited at increasingly oblique angles of incidence is used to demonstrate these effects.

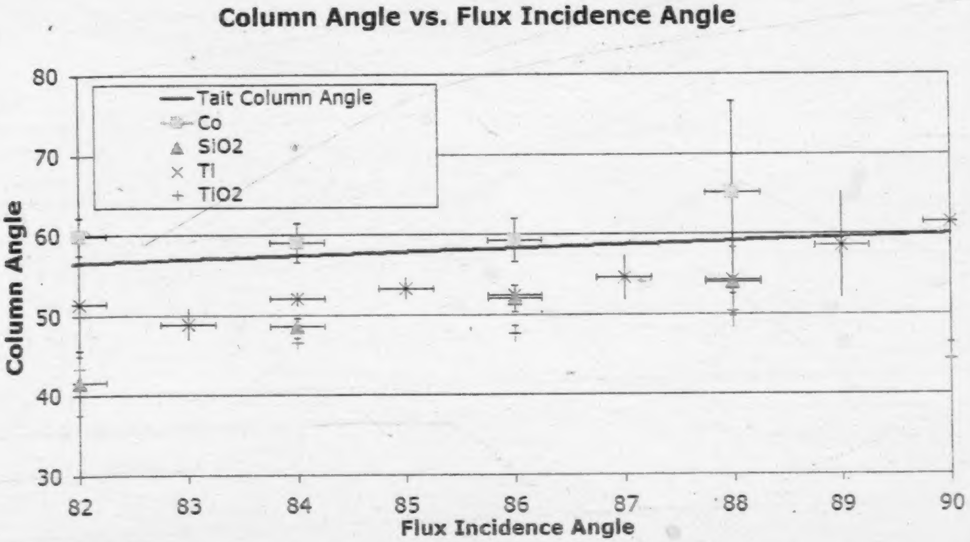

Figure 2.3. Comparision between Tait's predicated column angle and measured values. Column angles of cobalt, silicon dioxide, titanium, and titanium dioxide films were measured for increasingly oblique incidence angles. Each film series was deposited simultaneously using substrate samples held at slightly different angles. Although the general trend of columnar angle for these films follows that described by Tait, the values differ depending on the source material used.

An alternative approach describing $\beta(\alpha)$ has been adopted by Hodgkinson [37] to correct for a weakness inherent in both Tait's rule and the tangent rule; that is, their being generalized functions of $\beta(\alpha)$ irrespective of the material being deposited. Hodgkinson replaced the co-efficient of ½ in Equation 2.1 by an empirically determined function of α to take into account the known dependence of column angle on source material. Although this method does allow flexibility for material specific growth, to simplify the treatment of the GLAD technique, in this thesis only the generalized case, $\beta=\beta_{Tait}$, will be used as the predicted column angle.

In addition to being inclined relative to the substrate normal, columns grown at oblique incidence also exhibit separation from each other if the flux incidence angle is sufficiently large. A similar geometric model for the derived form of $\beta(\alpha)$ can be applied to obtaining the normalized column separation, a, as a function of α. This function is shown in Equation 2.3, and assumes that the incident adatoms are small compared with the column diameter. This assumption results in a relatively small spacing between individual columns.

$$a=\frac{1}{2}\left[1+\frac{1}{\cos\alpha}\right] \tag{2.3}$$

This expression shows that a dramatic increase in intercolumnar spacing occurs when $\alpha>80^\circ$ (i.e. the glancing angle regime). This effect is shown clearly in Figure 2.2, where both a plot of a vs α and a titanium film deposited at progressively more oblique angles is illustrated: both α and the columnar separation, a, are observed to correspondingly increase for $\alpha>80^\circ$. This property of increased separation of columns can be used to control the film growth and its resulting microstructure. Films deposited at $\alpha<80^\circ$ may be viewed as relatively dense by comparison.

2.3.1.3 Substrate rotation

In 1959, Young and Kowal observed optical activity and circular Bragg reflection in fluorite films deposited with active rotation of the substrate about an axis normal to its center [39]. The angle of rotation about this axis will be subsequently referred to as φ.

> *The possibility of evaporating in vacuum an optically active film of an otherwise isotropic material, by oblique deposition*

> *on to a flat glass substrate revolving about its normal as an axis, is confirmed. The helically deposited fluorite films ranged up to about 18μm thick and turned the plane of polarization of a normally incident beam by as much as 2.25° at λ=0.546μm* [39].

At the time, scanning electron microscopy (SEM) was not available to directly observe the films fabricated by Young and Kowal, although the relatively conservative incidence angle (α<70°) of their deposition indicates that the structures would have been reasonably dense. However, this work represents one of the first attempts to 'sculpture' a growing film through substrate rotation to enhance or change the resulting material properties. Unfortunately, their attempt went relatively unnoticed until recently.

In 1989, Motohiro and Taga [40] deposited columns at an oblique incidence angle of α=70° and showed that these films undergo an abrupt transition when the substrate is rotated through 180° in the φ-axis. For the initial portion of the film evolution, the column grows at a set angle β towards the flux source. At the point the substrate is rotated by 180°, the column abruptly changes direction so that the column inclination again points towards the incoming flux. Essentially, the column forms a chevron structure (i.e. a 'V' lying on its side) where the interface between the two distinct column directions is typically referred to in the literature as the Motohiro-Taga interface [41]. A stacked series of Motohiro-Taga interfaces thus forms a zig-zag structure. By significantly increasing the flux incidence angle, these zig-zag/chevron structure can be grown isolated from each other as a highly porous medium [4].

Theoretical work by Azzam [42], later expanded on by Lahktakia and Weiglhofer [43], continued the work of Motohiro and Taga by suggesting that a chiral response suitable for unique optical applications may be fabricated by coupling substrate rotation with oblique incidence. After experimental development of highly porous film structures [4] the term 'sculptured thin film' (STF) [44] was coined to describe films where the microstructure is actively adjusted during deposition to manipulate its properties. This term is gaining some acceptance in the literature, and is often used to describe relatively dense films fabricated using oblique incidence (α<75°) and substrate rotation [37, 45-47] Earlier films such as the Young and Kowal experiments mentioned previously are considered to be among the first STFs fabricated.

Independent of this research, a more deliberate study of thin films deposited at glancing angles with substrate rotation was undertaken at the University of Alberta under Dr. Michael Brett. By examining SIMBAD [48] simulations of film growth over trenches and vias, the possibility that isolated columnar structures may be formed using highly oblique flux incidence was suggested due to the appearance of these structures along the trench or via sidewalls (See Figure 2.4).

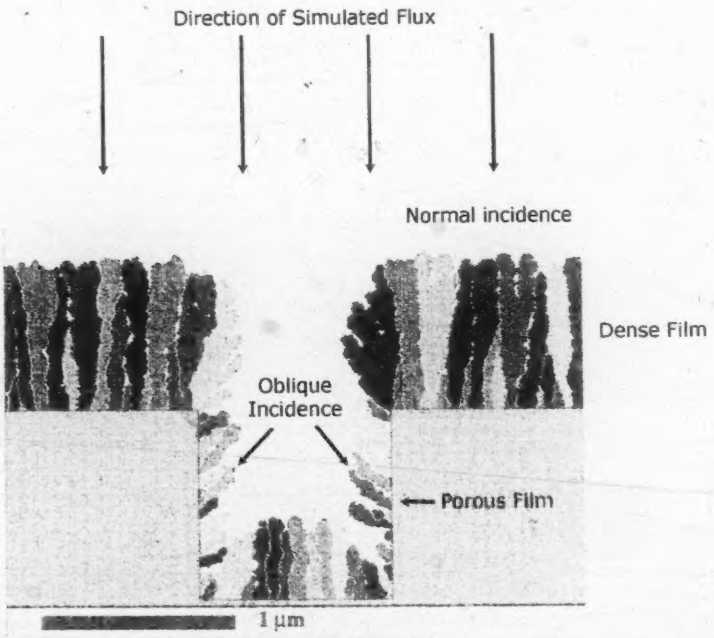

Figure 2.4. SIMBAD simulator of film growth over a trench. Film is deposited with a higher porosity along the trench sidewalls due to the higher incidence angle of arriving flux [49]

Subsequent work by Tait *et al.* [50] experimentally confirmed these findings, and led to a consequent paper (described in §2.3.2.2) which used a geometric model to describe the angle and separation of these isolated columns based on the flux incidence angle. Robbie *et al.* [4] later showed that rotating the substrate during deposition could abruptly change the growth direction of these columns to form zig-zag or chevron structures. Although similar to the Motohiro-Taga interface described previously, this result is unique in that Robbie grew *isolated* chevron structures rather than a chevron structure within an otherwise dense film. The term glancing angle deposition (GLAD) [6] was created to explicitly describe these high porous thin films with controlled microstructure deposited with extremely or glancing flux incidence. This terminology will be consistently used throughout the remainder of this document.

2.3.1.4 Simple GLAD Structures

Earlier, an image of an obliquely deposited film was shown to demonstrate the inclination of columns with respect to the flux incidence angle, α (see Figure 2.1). The growth of a structured thin film can be described succinctly by noting that columnar growth occurs in the plane parallel to that defined by the trajectory of the incoming vapour and the substrate normal, and is henceforth referred to as the deposition plane. If this plane is moved (either by rotating the substrate and keeping the source fixed, or by rotating the source and keeping the substrate fixed) the columnar growth direction can be controlled.

The first porous chiral structures were fabricated by Robbie *et al.* utilizing highly oblique, or specifically glancing angle flux incidence to separate the chiral structures and more actively control their resulting porosity and morphology [51]. From Figure 2.2(a), it is clear that the difference ($\Delta = \alpha - \beta$) in columnar angle and flux incidence angle increases with increasing α. More highly separated columns, and the resulting increase in film porosity, is a direct consequence of this observation. In the case were $\Delta = 0$, columns are inclined towards the source and yield no separation. An example of this circumstance is a film deposited at normal incidence. Here, the resulting columns are tightly packed and normal to the substrate. By choosing a point on the β vs. α plot, the porosity of the film can be easily tailored due to the increasing effect of shadowing on the substrate surface.

The GLAD technique has since been used to fabricate a range of porous thin film morphologies with isolated microstructures, many of which have been built upon the four simple structures shown and described below. For these and subsequent examples, the deposition rate, *r*, refers to the amount of film deposited at the position of the substrate, but on a plane that is held normal to the arriving flux. This definition is used because it describes the standard geometry for film growth measurements by a crystal thickness monitor.

Oblique Columns / Slanted Posts

Formed when substrate rotation about φ is zero. Porosity is introduced by glancing incidence flux

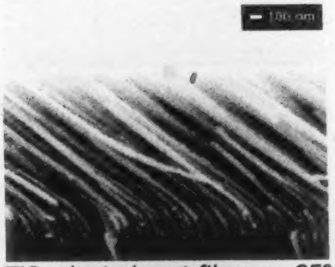

TiO_2 slanted post film: α=85°

Chevron / zig-zags [4]

Stacked Motohiro-Taga interfaces deposited at glancing incidence whereby a rotation about φ of 180° occurs for each arm of the chevron.

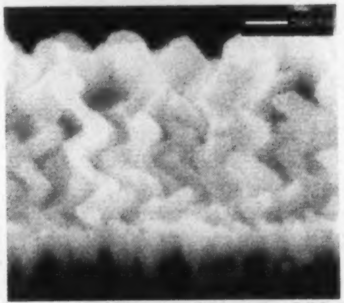

Cobalt chevron film: α=85°

Helices [51]

Formed when the substrate is rotated slowly and continuously relative to the deposition rate, *r*. Each complete turn of the substrate results in a single turn of the helical structure. The speed of rotation determines the pitch length (i.e. slow rotation = longer pitch, fast rotation = smaller pitch).

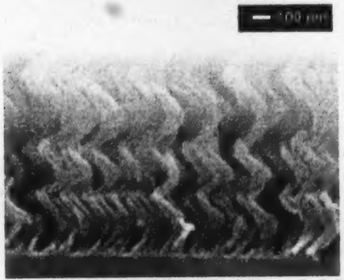

SiO_2 helical film: α=85°, $d\varphi/dt$ = 0.069 RPM, r=10Å/sec

Pillars / posts [52]

A special case of helical growth, though usually treated as its own structure type. If rotation is sufficiently fast, the pitch of the helix is so small that it is indistinguishable. The structure appears as a vertical column.

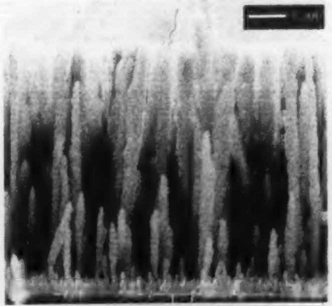

SiO_2 pillar film: α=85°, $d\varphi/dt$ = 8.3 RPM, r = 13Å/sec

The structural details for all the above film-types inherently depend on the source material being used, the substrate, crystallography, and other factors. For example, low melting point materials tend to have higher surface diffusion allowing adatoms to migrate further on the growing film to fill in much its fine structure, including the helical arms. Hence, vertical columns in these materials can be formed at a smaller rotational speed than those materials which have a high melting point (i.e. lower surface diffusion). This observation will be further explored in Chapter 4.

2.3.2 *Advanced GLAD structures*

2.3.2.1 Advanced Control System

The power of the GLAD technique does not arise from simply rotating the substrate at oblique incidence, but rather through the dynamic changing of the substrate through α and/or φ during deposition at glancing incidence [53]. The external control apparatus for growth of GLAD films has evolved considerably since the early "proof-of-concept" experiments. Individual stepper motors, each controlled externally by software running on a single computer, allow the user to adjust both α and φ independently while the film is being grown. Hence, a variety of microstructure forms can be programmed into the computer and subsequently grown. In addition, the control system can adapt to changing conditions within the deposition chamber through feedback provided by *in situ* measurement of film growth by a crystal thickness monitor. This growth is reported back to the computer software, which adjusts α and φ accordingly. Figure 2.5 shows a schematic of the current GLAD set-up without the feedback control blocks shown.

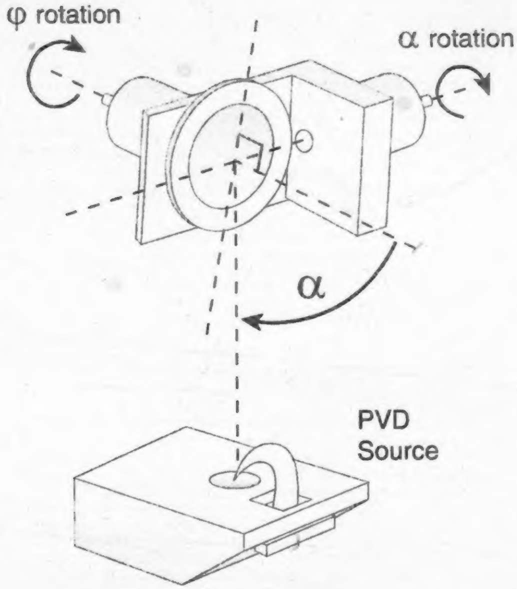

Figure 2.5. The GLAD system schematic. Stepper motors are used to control both the tilt (polar) angle α and the rotation (azimuthal) angle φ of the substrate holder. In this example, an electron beam evaporation source is depicted.

2.3.2.4 Other Advanced GLAD Structures

A number of film microstructures can be developed utilizing the advanced GLAD control system, including square spiral staircases (where each arm of the spiral is grown at 90° from the preceding arm) [11], super-helices (where a helical film is modulated by helical growth of higher pitch) [54], twisted ribbons (arguably pillars with a highly ellipsoidal cross section and relatively large pitch) [13], or microstructures with a capping layer [55]. Pause-spin growth, whereby the substrate rotation is paused at a particular φ allowing film growth to accumulate in that direction, can be used to modify columnar cross-sections and columnar angle [13]. Capping layers can be grown to provide encapsulation and protection to the porous films beneath them, while also allowing for multi-layer structures [56, 57], while square spirals, particularly when arranged as components in a lattice, have possible application as three dimensional photonic band-gap filters [58]. Some of these structures will be re-visited later in this thesis, while for the others the interested reader is referred to the appropriate references.

2.3.2.5 Periodic Structures

This section is intended to only briefly introduce the reader to periodic films as advanced GLAD structure examples. These films are described in more detail later in this thesis (see, for example, Chapter 3 for seed lattice preparation and Chapters 4 and 5 for film growth characteristics).

Typically, microstructures fabricated by GLAD are randomly distributed on the substrate. This feature is not detrimental for such applications as sensors, thermal barrier coatings, and catalytic devices. However, some optical (e.g. photonics crystals) [59-61] and magnetic applications [62] require a periodic lattice of structures in order to operate effectively. In addition, some of the fundamental properties of GLAD films are more easily acquired when the exact density of structures per unit area can be calculated [17].

The formation of randomly distributed GLAD structures on the substrate surface is inherently due to the nucleation stage of film growth, when energetically stable clusters of atoms seed randomly on the substrate and subsequently shadow the surrounding area. In collaboration with Marek Malac from the Department of Physics, it was shown that near identical structures can be formed by enforcing this shadowing effect at the initial stages of film deposition through the use of substrates with a pre-fabricated seed layer [63]. In this case, the seed structures were created using electron beam lithography. More recently, periodic pillars and oblique columns have been grown on plastic embossed substrates [64], while Kennedy *et al.* have fabricated square spirals on seeds produced using standard photolithography [11]. It is anticipated that any process that creates small, regular mounds out of an appropriate material may serve as seed layers for a subsequent GLAD deposition to form periodic microstructures. One possible example of another technique that may be used to form seed topography is laser interference lithography (see Chapter 7) [65].

If the seed morphology is optimized with regards to material parameters (e.g. melting point), substrate temperature, and the flux incidence angle, growth initially occurs predominantly at the seed sites. These microstructures can then grow regularly for some time.

For most materials deposited by GLAD, surface shadowing is the dominant growth mechanism, allowing the optimal seed separation to be approximated by:

$$p = t_{seed} \tan(\alpha) \qquad [2.5]$$

p and t_{seed} are the seed separation (edge-to-edge) and height, respectively. Figure 2.6 illustrates the geometry of this expression, while examples of periodic GLAD structures are shown in Figure 2.7. Note that for the remaining sections of this thesis, p will refer to the centre-to-centre spacing of seeding elements. This definition is accurate if the seed diameter is much smaller than p.

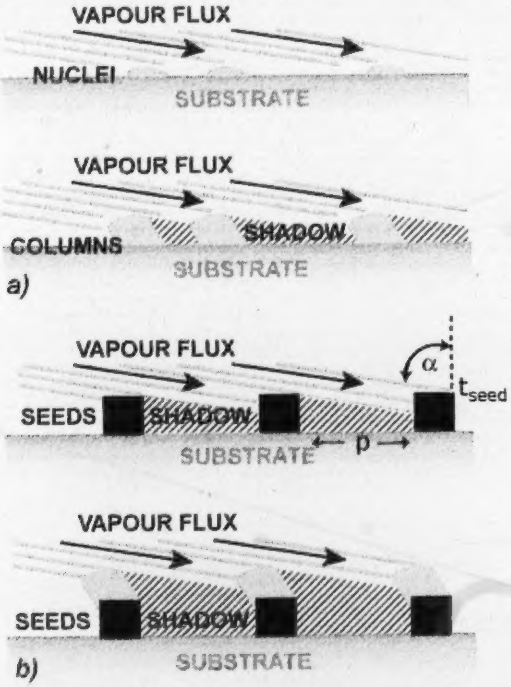

Figure 2.6. The film growth geometry for aperiodic (a) and periodic (b) films. If the seed separation (p) is optimized relative to the height of the seed (t_{seed}) and the angle of flux incidence (α), film growth occurs primarily at the seed sites. This seed separation is loosely based on Eq. 2.5. If p is much larger than the shadow cast by the seeds, or no seeds are present on the substrate, self-shadowing initializes film growth.

The growth by electron beam evaporation of periodic structures, particularly those of helical microstructures, is found to be quite robust. Defects introduced into the lattice in the form of missing seeds or lines of seeds have little effect on the growth of structures surrounding the defect [63]. Defects transfer to the film (the extreme flux incidence angle ensures that there is no flux coverage of the seedless defect area), while the uniformity of the film is preserved outside of the defect area. Structures along the edge of defects tend to increase in density or thicken slightly to take up the flux that would otherwise have gone into the growth of their neighbours. This effect is marginal if the number of missing lattice points is limited to the distance enclosed by one or two seed periods. The demonstration of low defect periodic GLAD arrays is of particular significance, as these films may be applied to the introduction of light-guiding structures for use in photonic band gap devices [11].

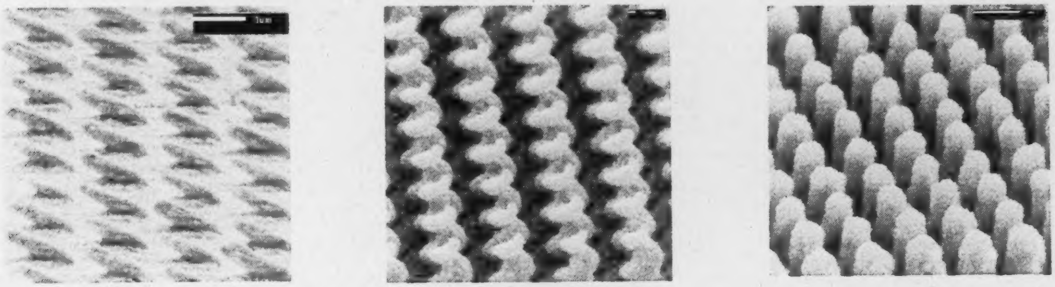

(a) (b) (c)

Figure 2.7. Examples of periodic GLAD morphologies grown at α=85° are shown above: (a) nickel oblique columns with a lattice period of 2μm; (b) SiO_2 helices with a lattice period of 600nm; and (c) SiO_2 posts with a lattice period of 900nm.

2.4 SIMULATION SOFTWARE

Simulations have been used as tools to describe obliquely deposited films at least since the pioneering work by Dirks and Leamy [32], and is continued in the present work. Although a number of simulation paradigms exist including continuum models [32], conservation of parallel momentum (primarily supported by a group of Japanese researchers starting with [66] and summarized in [67]), and angular dependent growth [68-70], ballistic deposition (BD) simulations have proven the most successful in describing the growth of thin films deposited with limited adatom diffusion and high mean free-path (the typical conditions in a GLAD chamber). In these simulations, particles are serially launched from just above the growing film. Each particle is allowed to follow a straight-line trajectory until it strikes the substrate or the film. An equilibrium model whereby each particle is allowed to aggregate into the film after diffusing a distance determined by an algorithm that minimizes the surface curvature-dependent chemical potential describes the subsequent surface diffusion.

Throughout most of the history of thin film simulation, insufficient computing power has limited software to simple two-dimensional [31, 71] and three-dimensional models [72, 73] which tended to exclude the effects of surface diffusion of adatoms over large scales. This exclusion is critical since it is generally accepted that surface diffusion is very important to the growth of obliquely deposited films. Over the last decade, the increase in computer power has significantly lifted this limitation, allowing for the creation of three-dimensional (3D) simulation programs to more properly model both adatom diffusion and the resulting porous thin film structures created at glancing incidence [74, 75]. Typically, for example, even films evaporated obliquely onto *stationary* substrates grow anisotropically, with flake-like morphology and significant growth fanning in the direction perpendicular to the incident flux and parallel to the substrate plane [19, 30, 33, 76].

Although a number of software packages have recently been developed, the Monte-Carlo ballistic simulator program, 3D-FILMS, has proven quite successful in the modeling of films deposited at glancing angles [74]. The progeny of the two-dimensional simulation package, SIMBAD [77], 3D-FILMS was developed in part to model several aspects of porous thin films. In its simulations, 3D-FILMS models a film as a large number of identical units. Each unit has cubical geometry and represents the statistically averaged behaviour of a large number of atoms (typically 1000). Nucleation, self-shadowing, adatom mobility, and a variety of other physical effects are all incorporated into this model, and simulated films can be displayed in a complete three-dimensional depiction including its microstructure, local film density, and differential and total surface area.

To model a deposition process, both the deposition parameters and substrate topography are specified. Substrate topography is represented by an initial distribution of cubes, enabling a variety of configurations; for example, flat substrates, trenches, vias, and steps. In addition, these configurations can be arranged as individual elements in a periodic lattice. Film 'deposition' occurs by serially launching particles from just above the growing film. The particles follow straight-line trajectories until they strike the substrate or the film, while their angular distribution and the angular coordinates of the substrate can be dynamically altered during the simulation based on either a pre-set or user-defined function. Periodic boundary conditions are typically used during 3D-FILMS simulations meaning particles that pass outside the simulation boundaries before striking the film/substrate, emerge on the opposite boundary edge. Surface diffusion in the growing film is described using an equilibrium model where each cube is allowed to aggregate into the film after diffusion a short distance along the surface according to an algorithm that minimizes a surface curvature-dependent chemical potential.

The simulated growth of GLAD films can be obtained using 3D-FILMS by introducing a temporal dependence to the incidence flux (i.e. $\alpha(t)$, $\varphi(t)$) under limited surface diffusion. Specifying a substrate topography consisting of a pre-defined seeding array can simulate periodic GLAD structures. Apart from the general film structure, 3D-FILMS has proven capable of reproducing peculiarities evident in the structure of individual columns including rounded elbows and bifurcation in chevron structures, columnar growth competition, and extinction [74]. Further, post-processing of these simulations allows for insight into such evolving film properties as film density (Figure 2.8) and cross-sectional area (Figure 2.9).

In addition to 3D-FILMS, a second 3D simulator, Virtual Film Growth System (VFIGS), has been recently reported [75]. This simulator, also built around the basic SIMBAD system and following a similar development framework as 3D-FILMS, was primarily created to understand the surface area of STFs (referred to in their work as dynamically obliquely deposited, or DOD, films). By simulating the growth of various film morphologies from α=0° through α=82°, VFIGS found no significant dependency of either packing density or effective surface area on $d\varphi/dt$. These properties were found to be primarily a function of α, and, although the packing density diminished in the expected fashion, the effective surface area was observed to increase sharply to a maximum at α=70°.

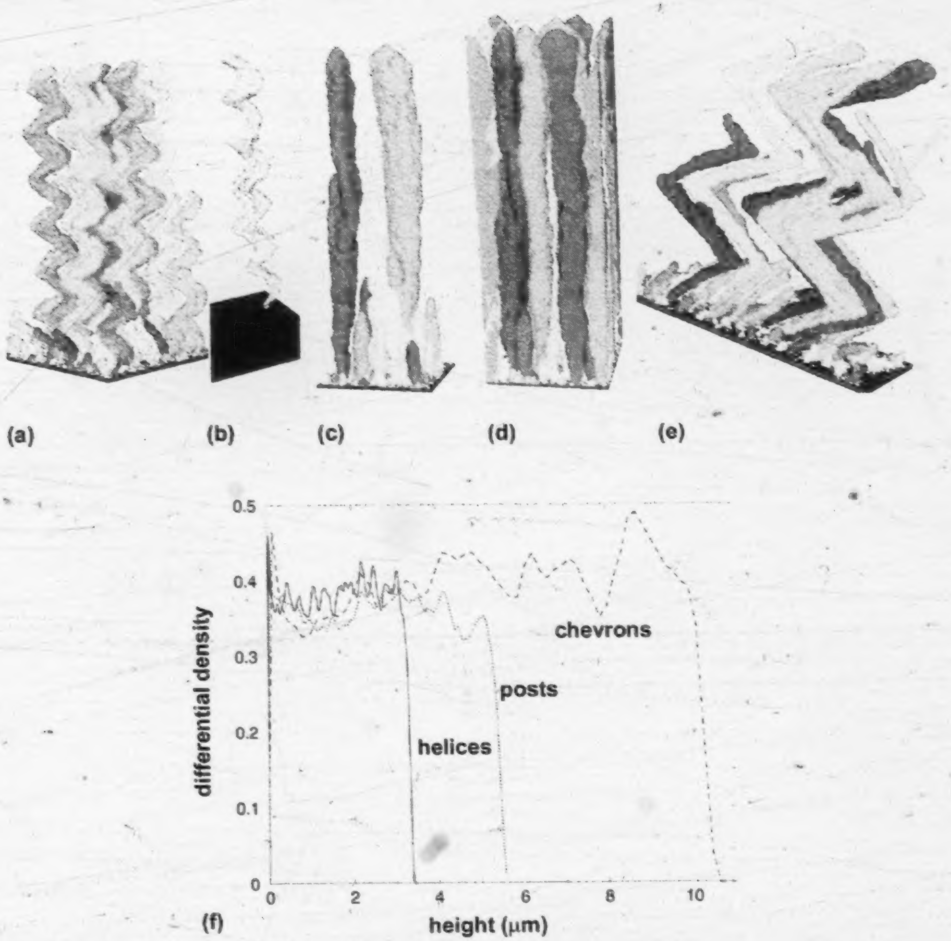

Figure 2.8. 3D-FILMS simulations of different GLAD film morphologies deposited at the same flux incidence angle. These morphologies include: (a) helices; (b) a single helix from the simulation of (a); (c),(d) posts; (e) chevrons. A plot of the differential density as a function of height for the simulations at the left is shown in (f). Note that the simulation predicts that the resulting average film density is not dependent on microstructure form.

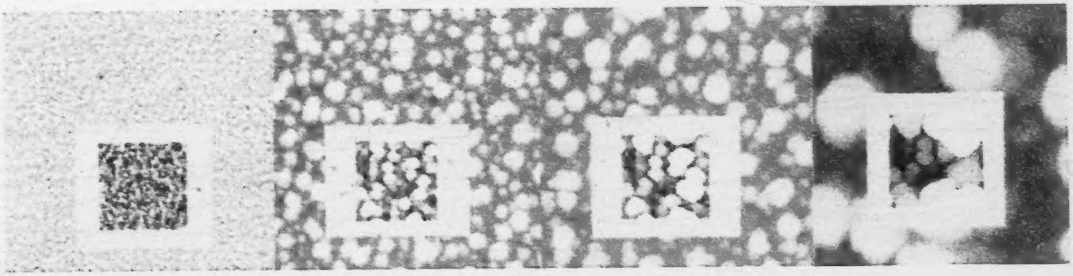

Figure 2.9. Plan view of both real films and 3D-FILMS simulations. The background image is an SEM image of a deposited film. Pseudo-SEM images were obtained using a plan perspective of 3D-FILMS simulations, and are placed as insets in each panel.

In the following chapters, the 3D-FILMS simulator will be used as a powerful tool for modeling and guiding the experimental research into the fundamental growth characteristics of GLAD films.

Chapter 3 – Substrate Preparation

3.1 INTRODUCTION

The fabrication of periodic nanostructures by GLAD is inherently dependent on the enforced shadowing of adatoms incident on the film surface through the use of a pre-fabricated seed layer (see §2.3.2.5). Previous chapters have described and demonstrated the growth of periodic columnar, helical, and pillar nanostructures grown using this methodology.

A number of techniques may be used to produce seed structures suitable for growing periodic films including:

1. Focussed ion beam (FIB) Patterning [78, 79]
2. Photolithographic patterning [11, 80, 81]
3. (Achromatic) Interferometric Lithography (AIL) [82-84]
4. X-ray Nanolithography [85]
5. Anodized Aluminum Oxide [86, 87]
6. Electron beam lithography (EBL) [88, 89]
7. Plastic/Hot embossed patterning / Nanoimprint lithography [90-92]

This chapter examines two of these processing tools: Electron beam lithography, which was used to produce most of the seed topography shown; and, plastic/hot embossed patterning, which is presented as a potential means for high throughput production of seed lattices.

3.2 ELECTRON-BEAM LITHOGRAPHY

Although many of the periodic films presented in this thesis were grown on initial seed layers prepared by an electron beam lithographic (EBL) process, the present work was limited to specifying the required array geometry. The lithographic processing was completed by Marek Malac and Miro Belov of the Department of Physics (University of Alberta), and Martin O. Jensen (currently a Ph.D. student within the GLAD research group at the University of Alberta). In what follows, a brief overview of the EBL technique is given as well as the specific structures and geometries used to fabricate the periodic films shown in this thesis.

3.2.1 *Background*

Electron beam lithography, combined with electrodeposition and/or a lift-off process, has been used as a means of creating prototype patterns for a variety of proposed applications (e.g. high density magnetic storage media [93]). Its strength as a research tool lies in the ability of the user to design specific patterns and produce them with features sizes of 10nm and above.

EBL utilizes an electron source with high intensity and uniformity, small spot size, good stability, and long life for either mask generation or direct writing of patterns on a wafer. Although electrons are occasionally ejected via photoemission, typically a thermal process (referred to as thermionic emission), field emission, or combination is used. Each of these emission processes has its strengths and weaknesses including:

Table 3.1. Comparison of Thermionic and Field Emission processes

Emission Process	**Strengths**	**Weaknesses**
Thermionic Emission	brightness, cheap	low coherence
Field Emission	high coherence	brightness, high cost

In many respects, EBL is similar to photolithographic processes, except that the relatively small wavelengths of emitted electrons allows for smaller feature sizes to be fabricated. Electromagnetic lenses focus the emitted electrons onto a substrate containing a polymer sensitive to the incident electrons (e.g. polymethyl methacrylate, or simply PMMA). This polymer is an analog to the photoresists used in photolithography. Figure 3.1 illustrates the basic steps in EBL processing.

Throughput remains, however, a primary difference between photolithography and electron beam lithography. Where photolithography processes expose the entire pattern on the wafer simultaneously, EBL utilizes raster scanning to accurately define small features. The low throughput of EBL was the motivation for studying plastic embossing process as a means to increase the throughput of seed production without compromising the feature sizes observed (see §3.3ff).

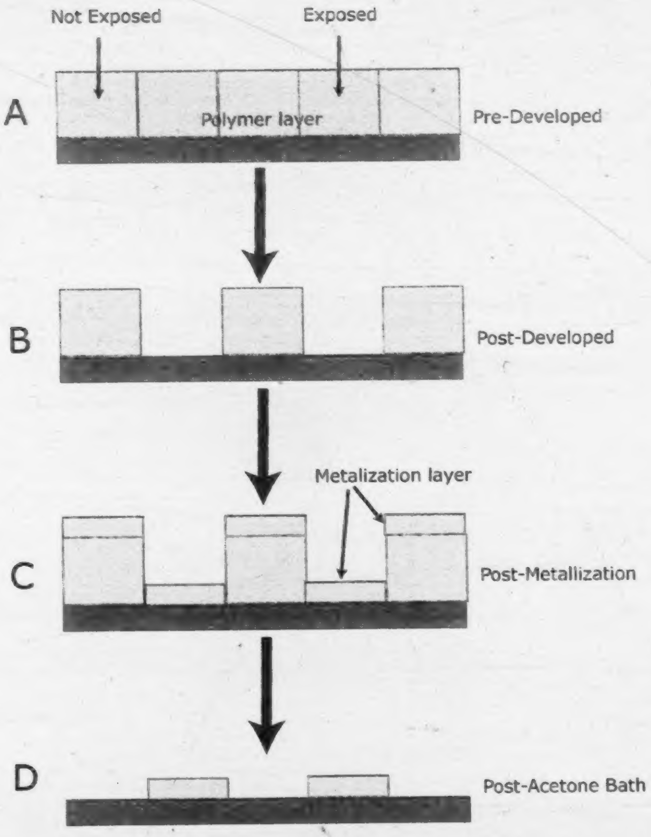
Not Exposed
Exposed
A
Polymer layer
Pre-Developed
B
Post-Developed
Metalization layer
C
Post-Metallization
D
Post-Acetone Bath

Figure 3.1. Simplified processing steps for producing seed arrays by electron beam lithography. In most instances (such as the 1^{st} generation EBL arrays given in §3.2.2), processing is taken to Stage D where seeds are the remnants of the metallization layer after lift-off. For many of the seed arrays used in this thesis, Stage B structures are sufficient. In this case, seeds consist of the developed PMMA pattern before a metallization layer is applied.

3.2.2 1^{st} Generation EBL Arrays

The seed array used for determining the magnetic properties of GLAD films (see Chapter 5) consisted of a 1000x1000 seed array with lattice period of 500nm. Individual seed elements were fabricated using a lift-off technique, with titanium as the metallizing layer (see Figure 3.1, Stage D for the resulting seed topography). Individual seed diameters were chosen to be 200nm, while their thicknesses were nominally 200nm.

Elements were fabricated using a Philips 505 scanning electron microscope operated at 30kV and driven by a digital raster. An external computer running the SMART program [94] provided the digital raster control.

3.2.3 2^{nd} Generation EBL Arrays

One of the weaknesses of the 1^{st} generation arrays was the inability to determine how seed period effects growth without constructing an entirely new array with a revised lattice constant. In addition, accurate comparisons between films grown in different deposition cycles is not possible due to the potential for minute changes in film deposition rate, ambient chamber pressure/residual gasses, and flux incidence angle.

To help correct for this deficiency, an EBL pattern was designed consisting of seed elements arranged in 5 arrays each containing a 10x10 seed matrix (see Figure 3.2). Miro Belov at the University of Alberta NanoFab subsequently fabricated these arrays. Centre-to-centre separation between elements increased between individual arrays, each of which was set to 150, 300, 600, 900, or 1200nm periodicity. Each seed element was cylindrical with height and diameter of approximately 80nm (measured via SEM), and was fabricated directly from the PMMA used during the lithographic process, thereby saving the additional processing steps required for lift-off. The lower robustness of the films deposited on the PMMA medium (compared with a film deposited on a metal layer) was not a concern for this work.

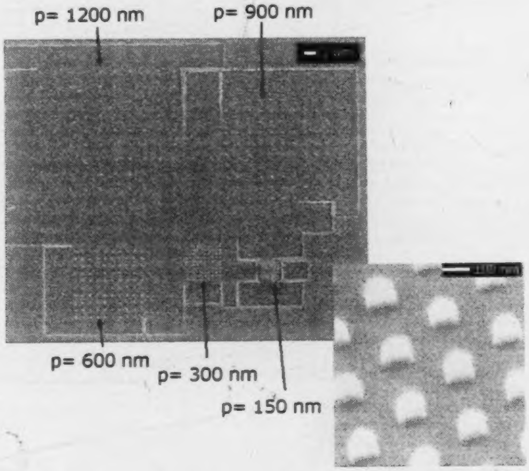

Figure 3.2. EBL seed pattern used for studies on the effect of periodicity on film growth. The overall pattern consists of 5 sets of 10x10 arrays, with varying periods (i.e. p=1200nm etc..). Each seed element is fabricated directly in the PMMA (as per Stage B of Figure 3.1). A selection of these seeds is shown in an oblique view as an inset.

3.2.4 3rd Generation EBL Arrays

The epoxy novolak SU-8 [95] chemically amplified (CA) resist has recently been introduced for use in a wide range of applications requiring high aspect ratio structures by optical lithography. Although typically applied as a thick layer, Wong et al. recently demonstrated that thinner layers of SU-8C (a revised formulation of SU-8) can be used to fabricate optical waveguides by EBL [96]. This work been continued at the University of Alberta NanoFab by Aktary *et al.* [97] who have fabricated high-resolution grating structures with a 30nm line-width.

Students and research associates in the GLAD research group have used SU-8 to create seeding arrays due to its high sensitivity and robustness, excellent material and optical properties, and ease of processing (i.e. processing steps are similar to standard PMMA but no lift-off is required). These characteristics are complimented by the EBL raster control software (NPGS from JC Nabity Lithography Systems) installed on the University of Alberta NanoFab's LEO-440 SEM. This software system integrates movement of the SEM stage, allowing larger and more complex dot patterns to be created.

Based on the design shown in §3.2.3, Martin O. Jensen has fabricated several samples of seed patterns consisting of arrays of 900x900 seed elements, each cylindrical element measuring 175nm in diameter and 130nm in thickness.

3.3 PLASTIC EMBOSSING[†]

The EBL technique described above has proven to be the most suitable for my research on the growth of periodic GLAD micro- and nanostructures due to the ease of which seed geometries can be adjusted between different patterns. Unfortunately, one of the deficiencies of this technique, as has already been identified, is the low throughput, which makes EBL undesirable for use in large area applications.

[†] This section has been partially excerpted from the article: B.Dick, J.C. Sit, M.J. Brett, I.M.N. Votte, C.W.M. Bastiaansen, "Embossed Polymeric Relief Structures as a Template for the Growth of Periodic Inorganic Microstructures", Nano Letters, **1**, 71 (2001)., and is used with the permission of the American Chemical Society (2003).

Conventional embossing processes in thermoset resins may be used as an alternative means of producing these relief structures reliably and quickly over large areas. In the section that follows, the procedure by which periodic lattices of both silicon dioxide pillars and oblique nickel columns were fabricated over arrays consisting of seeds of 2μm periodicity is described. These seeding elements were fabricated by Dr. I.M.N. Votte and Dr. C.W.M. Bastiaansen at the Eindhoven University of Technology (The Netherlands). Deposition of the GLAD structures occurred at the University of Alberta.

3.3.1. Background

The reproduction of nano- and microrelief structures in polymers with embossing is extensively used in the large-scale production of, for example, compact disks and holograms. Moreover, it was shown by Chou *et al* that it is possible to reproduce nanostructures with typical dimensions as small as 20 nanometers in polymers over areas as large as 16cm^2 [90-92] with a high throughput.

3.3.2. Production of the seeds

Films of poly(tetrafluoroethylene-co-hexafluoropropylene), or Teflon FEP 100 (T_m = 260°C) were produced by compression moulding (24.5 N, 1 min) at 330°C between two cover slips. The resulting thickness of the films was estimated to be on the order of 200μm. Silicon calibration gratings for a scanning probe microscope (SPM) patterned with different grating sizes and shapes were used as masters. These masters were placed on the top of the FEP film, which was heated to 330°C and subjected to a pressure of 1 MPa over 9mm^2 for 1min. Subsequently the pressure was relieved and the sample was quenched to room temperature. The master was then removed from the FEP film.

The embossed FEP films were used as masters for the embossing of the resins. The epoxy resins were prepared from a mixture of diglycidyl ether of bisphenol-A (DGEBA) with 4,4'-methylen-bis-(3-chloro-2,6-diethylaniline)(M-CDEA) in a stoichiometric concentration of 100 parts per weight of DGEBA for 51 parts per weight of MCDEA. The selection of the epoxy resin as the material for the microrelief structure was predominately motivated by the high temperatures used in the growth of inorganic nanostructures using GLAD. The mixture was degassed at 60°C for 2 hours under reduced pressure. A drop of resin was deposited onto a glass slide and covered with a FEP mask with "spike" nanostructures. The samples were subsequently placed in an oven at 125°C and subjected to the following curing cycle: 4 hours at 125°C, 4 hours at 175°C and 4 hours at 225°C under reduced pressure in order to obtain a glass transition temperature on the order of 200°C. After the curing cycle, the samples were quenched to room temperature and the FEP master was removed from the embossed epoxy resins. This process is shown schematically in Figure 3.3.

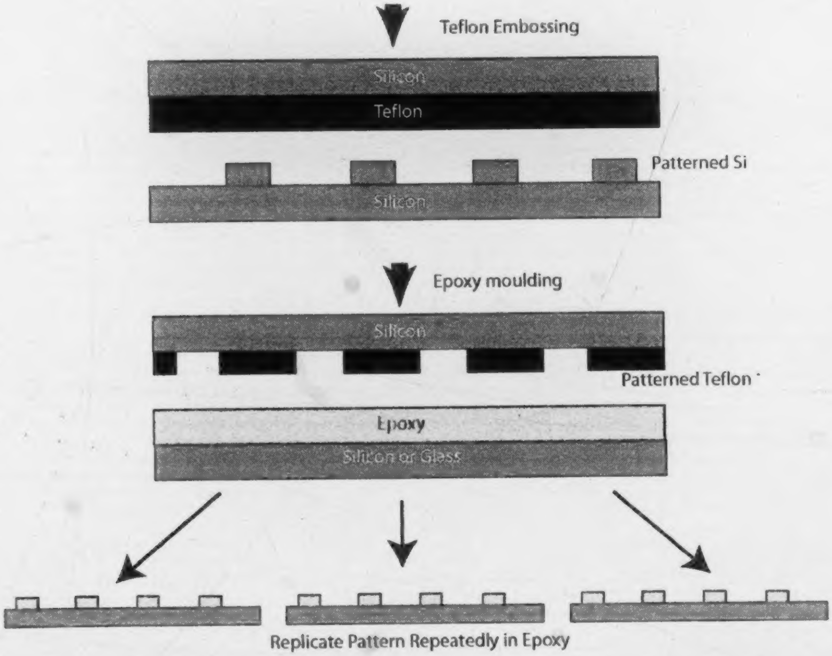

Figure 3.3. Schematic of the production steps undertaken to fabricate embossed patterns in epoxy. A silicon template is first produced, and subsequently 'stamped' into a layer of Teflon under heating. The resulting Teflon pattern serves as a master embossing template for pattern creation in epoxy. Multiple identical epoxy patterns can be fabricated quickly using this process.

3.3.3. GLAD fabrication parameters

Two types of source materials (nickel @ 99.995% purity and silicon dioxide @ 99.99% purity) deposited by electron beam evaporation were used for my 'proof-of-concept' experiments. These two materials and the deposition process were chosen because their combination has been used successfully in the formation of periodic microstructures grown on PMMA seed arrays [8, 63]. Before deposition, the system base pressure was typically 2.5×10^{-4} Pa, while the deposition pressure was 2.7×10^{-3} Pa for SiO_2 and 3.0×10^{-4} Pa for nickel. The deposition angle, α, was set to 85°, and the average growth rate (at normal incidence) was measured as 15Å/sec for both SiO_2 and nickel. The growth rates were measured *in situ* using a Sycon STM-100 crystal thickness monitor.

3.3.4. Findings

Figure 3.4(a,b) shows an array of epoxy 'bumps' that serve as seeding sites for the later growth of GLAD nanostructures. The seed periodicity in both images is 2μm. These images were obtained using scanning electron microscopy (SEM). Both posts and oblique columns were grown on these epoxy arrays, and the resulting nanostructures are shown in Figure 3.4(c,d).

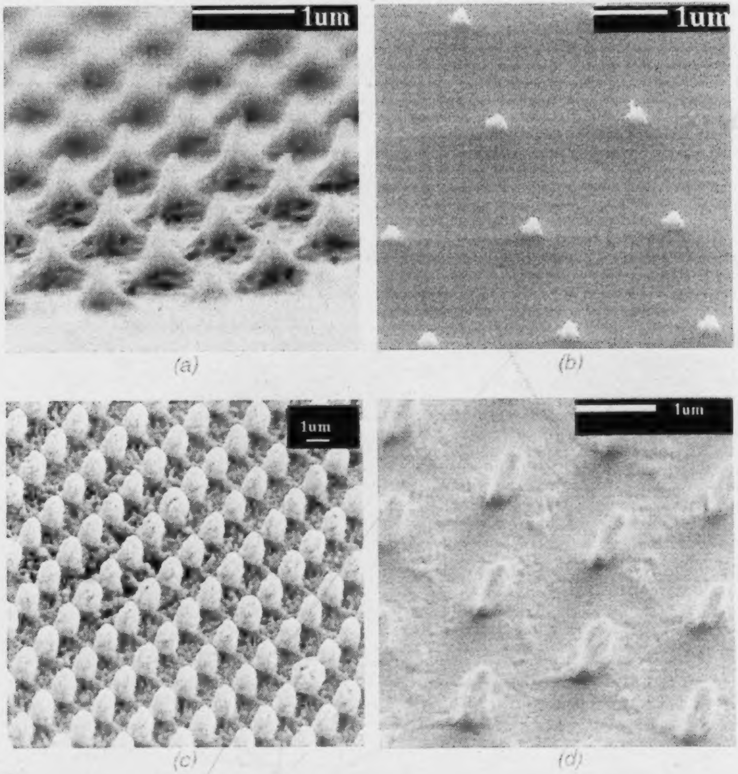

(a) (b)

(c) (d)

Figure 3.4. Two types of epoxy nanostructures prepared by embossing and shown before (a,b) and after film growth by GLAD (c,d). Both types have the same periodicity and pyramidal geometry though with different sizes: Approximate feature height of (a) 0.60±0.01μm, and (b) 0.15±0.3μm. (c) is an oblique image of SiO_2 pillars grown on the patterned array shown in (a). The thickness of these pillars was determined by SEM to be 1.58±0.13μm. (d) is an oblique image of oblique columns of nickel grown on the epoxy seed array shown in (b). The thickness of this film was measured to be 0.60±0.03μm

In these images, the film in Figure 3.4(c) has been grown using the seed images in Figure 3.4(a), while the film in Figure 3.4(d) corresponds to the seed array in

Figure 3.4(b). Note that for both nanostructure types shown, the nanostructure periodicity matches that of the underlying seed, and only a small amount of film growth between individual nanostructure elements can be observed. This observation is expected due to the shadowing of the substrate surface by each seed element. Small striations of film growth occur when at specific angular orientation when the flux is lined up with the hexagonal array.

The area of the film arrays shown in Figure 3.4 is approximately 3.6mm^2, containing over 10^6 individual elements. Although in this demonstration both the area and the number of elements is not very large, with respect to both typical wafer sizes and other lithographic techniques [65], a large number of arrays can be stamped by the embosser quickly, and subsequent use depends only on the epoxy curing time. Previously, other authors were mentioned who have demonstrated both larger area arrays (up to 16cm^2) and smaller periodicities between seed elements without noticeable degradation of the embossed pattern or increase is processing time [92]. Hence, it is possible that larger area embossed patterns can be realized by step-and-repeat embossing.

3.3.5. *Conclusions from Plastic Embossing Study*

The use of epoxy seeds coupled with the GLAD technique represents a simple and efficient way of manufacturing periodic arrays of unique nanostructures including posts, helices, and zig-zags. The latter two structural examples are not known to be easily fabricated by other nanoimprinting techniques. As shown in Figure 3.4, the size of individual seed elements can be made less than 75nm in diameter, and it is foreseen that this dimension can be reduced further. In addition, periodicities of less than 100nm for embossed structures have previously been reported [90, 91]. Once the FEP master is optimized and fabricated for a particular application, large area arrays of epoxy mounds can easily be embossed. Fabrication of periodic nanostructures (e.g. pillars, oblique columns, or helices) of densities greater than 10^{10} elements per square inch then require only one subsequent processing step using the GLAD technique.

Chapter 4 – Flux Incidence Angle and Substrate Rotation

4.1 INTRODUCTION

The isolated structures of GLAD films allow for the study of fundamental thin film growth behaviour, particularly in regards to self-shadowing processes and surface energy considerations. For example, by observing that the diameter of a helix arm gradually increases during deposition, one might assume a number of processes to be at work, including [98]:

1. An increase in adatom diffusion length due to an increase in substrate temperature during growth
2. An increase in the amount of material deposited on a given helix due to the suppression of neighbouring structure growth (i.e. columnar competition)
3. Bifurcation within a helix arm due to anisotropic shadowing (see Figure 1.1)
4. Preferential growth of fast growing crystal planes whereby the fast growing crystal plane dominates the resulting film microstructure form and texture [99].

These processes suggest that not only is the geometry of the deposition system a factor during growth (due to its imposed effect on the shadowing mechanism at the substrate surface), but material properties such as crystallography, vapour pressure, and the deposition technique itself (either sputtering or evaporation) all have strong roles to play in the resulting film microstructure. In order to properly apply the GLAD process to commercial products/applications, a more in-depth understanding of the fundamental growth characteristics of these films is required.

In the following two chapters (nominally split into "basic" and "advanced" GLAD), a few of these process and geometry parameters are explored, including flux incidence angle (α) and substrate rotation ($d\varphi/dt$) in Chapter 4, and seed periodicity (p) and flux angular distribution ($\Delta\alpha$) in Chapter 5.

Unless otherwise stated, films shown in this and the subsequent chapter have been deposited with the following parameters:

- Process = electron beam evaporator
- Film growth rates measured *in situ* using a Sycon STM-100 crystal thickness monitor (CTM)
- Substrate temperature during deposition measured at 175±25°C, as determined with a thermocouple fastened to the substrate during similar depositions, but without substrate motion [100]
- Distance between source and substrate was 42 cm

4.2 INVESTIGATION ON FLUX ANGLE DEPENDENCY

4.2.1 Film Morphology

One of first control parameters for glancing angle deposition is the dependency of film growth on the angle of incident flux. As was noted in Chapter 2, columns become increasingly separated as α is increased. This effect becomes even more dramatic as α passes from highly oblique to extremely oblique or so-called glancing incidence (typically defined as α>75°).

Although the effect of flux angle on film morphology has been noted elsewhere (See §2.3f, and also [4, 101]), these studies have not been extensive. This section presents a means to quantitatively study the effect of this parameter on film growth.

Recently, Doug Vick (a research associate in the GLAD research group at the University of Alberta) designed a substrate holder, which held a series of six 1 cm x 4 cm sized samples at varying angles to the incident flux. The angular range of this design was 10°, or 2° between samples. Using this device, he was able to show the trend of increasingly oblique incidence angle on slanted posts for a variety of materials including, for example, titanium and titanium oxide. An example of this work was shown previously in Figure 2.2(c), where a collage of titanium films representing an angular range from 82° to 89° was shown. This device was further used to evaluate β_{Tait} for selected materials (see Figure 2.3).

The primary advantage of evaluating films deposited simultaneously over a range of deposition angles is the consistency of system characteristics (i.e. flux angle drift, oxygen content, deposition rate variance), which is difficult to control precisely between different deposition cycles. One may argue, however, that the disadvantage of his design is that it allows the user to quantify the effects on film growth due to obliquely incident flux on a *stationary* substrate only. To correct for this possible disadvantage, an apparatus was designed to allow for growth evaluation on a *rotating* substrate. This design consisted of a series of substrate plates held at adjustable distances from the axis parallel to incident flux (see Figure 4.1).

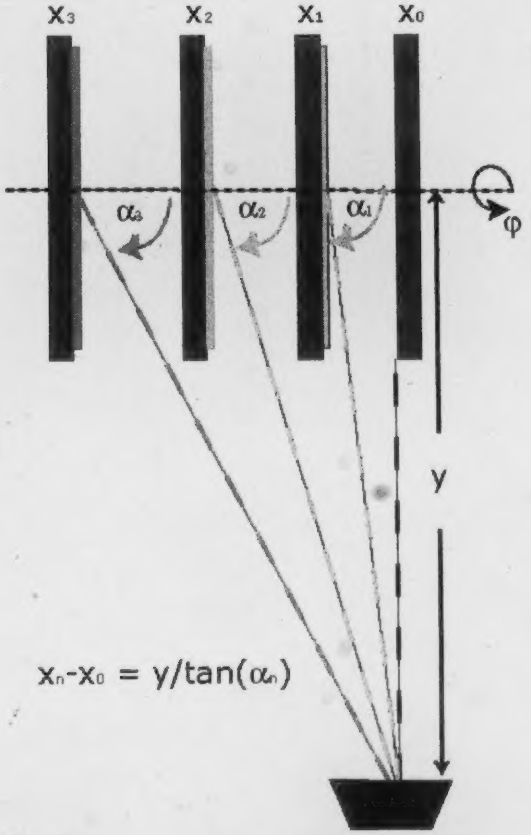

Figure 4.1. Simultaneous deposition of GLAD films at several incident angles. By adjusting the position of individual substrate plates (i.e. x_3 through x_1 on this diagram), different incident angles can be obtained. The minimum distance between adjacent plates can be approximated by $(x_{n+1}-x_n) \geq yl/(x_n-x_0)$ where l is the substrate plate radius. If this condition is not met, then incoming flux to substrate x_{n+1} is shadowed by plate x_n.

Using the device shown in Figure 4.1, the effective flux incidence angle on up to four substrate surfaces could be controlled. For example, one of the GLAD electron beam evaporators has a throw distance of approximately 42 cm. Hence, a range in substrate plate location may consist of 0.73 cm ($\alpha_{effective}$=89°) to 5.2 cm ($\alpha_{effective}$=83°). This variance in incident flux (calculated using the cosine law) across this lateral range is less 0.8%, and hence is expected to have little appreciable impact on the rate of flux incident on the individual substrate surfaces. An example of one of the film sets grown using this device is shown in Figure 4.2.

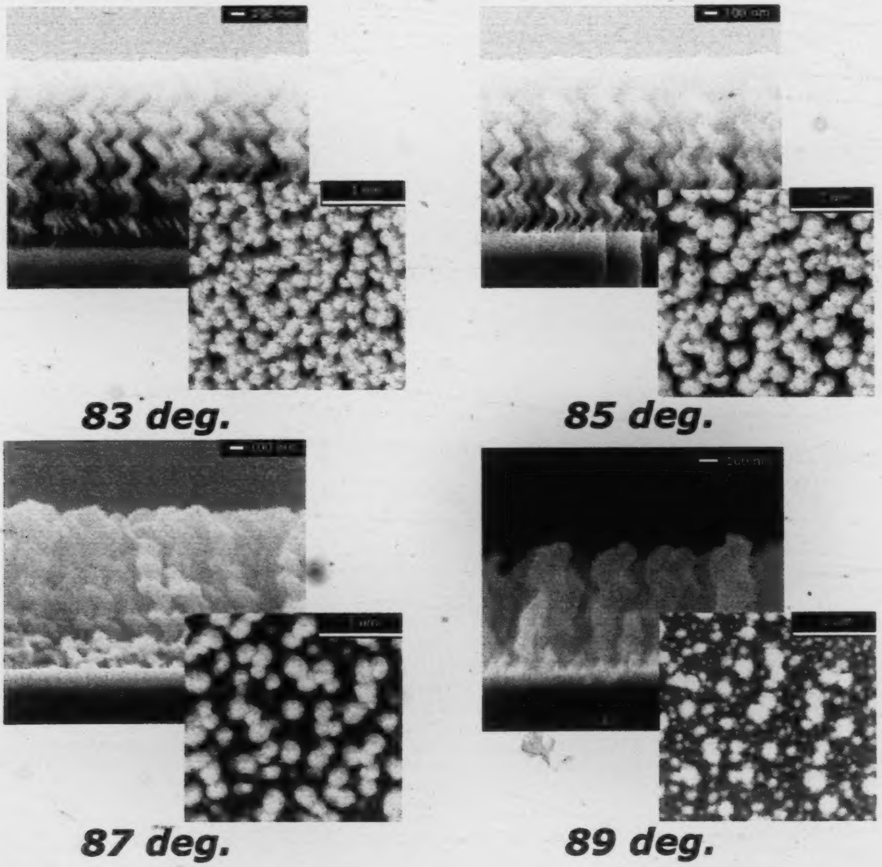

Figure 4.2. Effect of changing flux incidence angle on the morphology of GLAD films. This film set was grown using the apparatus shown in Figure 4.1, with $d\varphi/dt \sim 0.1$ *RPM. Film density decreases significantly from* α=83° *to* α=89°, *as is apparent from the more widely separated structures in the bottom right panel compared to those in the upper left.*

The decrease in film density (at least based on a plan view) with increasing flux incidence angle is clearly apparent from Figure 4.2. This result supports earlier simulation and experimental results published elsewhere [30, 74, 102-104]. In this set of films, however, because they were deposited simultaneously, only the flux incidence angle changes between neighbouring panels. Here, all films were rotated at $d\varphi/dt \sim 0.1$ RPM. The deposition rate, r, was 15Å/sec as measured based on a film deposited at normal incidence. At α=83°, the helical microstructure is well formed with a small separation between individual elements. At α=85°, the structure is also well formed, although the element separation has increased (corresponding to a decrease in film density presuming that the material in individual structures does not change its density). As the flux incidence angle is increased further, the structure form degenerates significantly. Enhanced shadowing at α=89° increases the sensitivity of film growth to structural differences in adjacent columns, and translates into a few dominant columns capturing the majority of flux incident at the film surface. This flux "fills-in" the helical coils, resulting in structures that do not differ significantly from pillars.

4.2.2 Derived Expression for Film Density at Glancing Incidence

One of the film characteristics affected by flux incidence that can be evaluated using the above experimental set-up is film density.

While studying the density of GLAD films, a simple method for approximating density variance at oblique incidence was developed. Here, area exposed to incident flux at normal incidence (α=0°) is expanded by a factor of cos(α) for a substrate tilted to α degrees. In addition, a factor taking into account the material being deposited must also be considered. To correct for microstructural or material dependencies on film growth, the thickness of the film grown on an oblique substrate (i.e. $t(\alpha)$) relative to that grown on a normally aligned substrate (i.e. $t(\alpha=0)$) is used. Hence, the thickness ratio of the film is introduced where $\kappa=t(\alpha)/t(\alpha=0)$. This additional factor results in a rough estimate for the film density:

$$\rho = \kappa\rho_{(\alpha=0)}\cos(\alpha) \qquad [4.1]$$

Earlier, the geometric derivation of β by Tait *et al* (see §2.3.2.2) was described. In their published article, a normalized density function of film grown at oblique incidence was also expressed [30]:

$$\rho_{normalized} = \frac{1}{a} = \frac{1}{1 + \frac{1}{\cos\alpha}} \qquad [4.2]$$

where a is the average spacing between individual columns defined in Eq. 2.3.

The expression in Equation 4.1 can be reduced to a purely geometrical interpretation (along the lines of Tait) by letting $\kappa = \sin\beta$, where β is given by Equation 2.2. This substitution can be made if the length of the oblique column is treated as equal to the thickness that the film *would have grown* if deposited with normal incidence. The thickness of the obliquely deposited film can then be determined by geometry. Hence, Equation 4.1 becomes:

$$\rho_{normalized} = \sin\left(\alpha - \sin^{-1}\left(\frac{[1 - \cos\alpha]}{2}\right)\right)\cos(\alpha) \qquad [4.3]$$

Plotting both Equation 4.2 and 4.3 (see Figure 4.3), it is found that they yield approximately the same density factor within the highly oblique to glancing flux incidence regime.

The Tait function shown in Equation 4.2 has been compared successfully to simulation studies of growing films. To compare how the expression in Eq. 4.3 describes the density trend observed in real films, the SiO_2 film set shown in Figure 4.2 was carefully measured on a microbalance, and then measured again after the film was etched away. The film thickness before etching was determined by scanning electron microscopy. The resulting values (normalized over substrate area) are shown in Figure 4.4.

The film densities predicted by Equation 4.1, and those measured on the SiO_2 film set show a similar trend (excluding only those films deposited with flux nearly parallel to the substrate), although a value difference between the two curve is clearly apparent even if measurement error is considered.

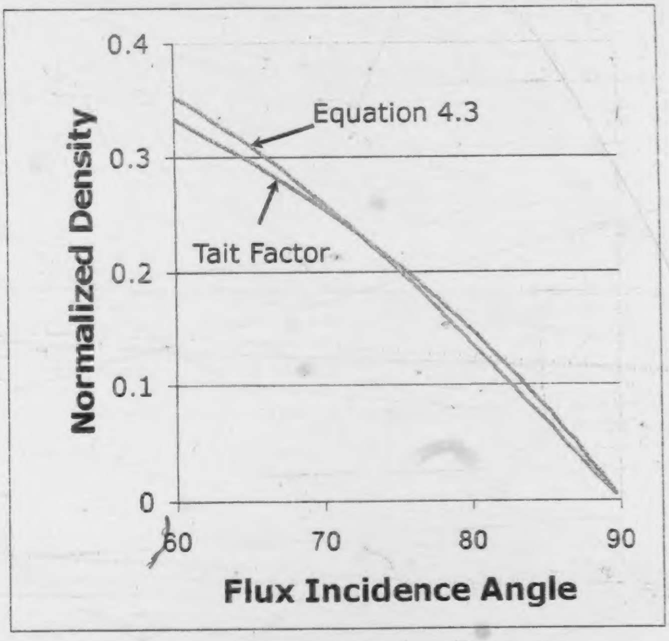

Figure 4.3. Normalized Density Functions. Note the similarities between the normalized density functions given by Tait [30] and Equation 4.3 for α>60°.

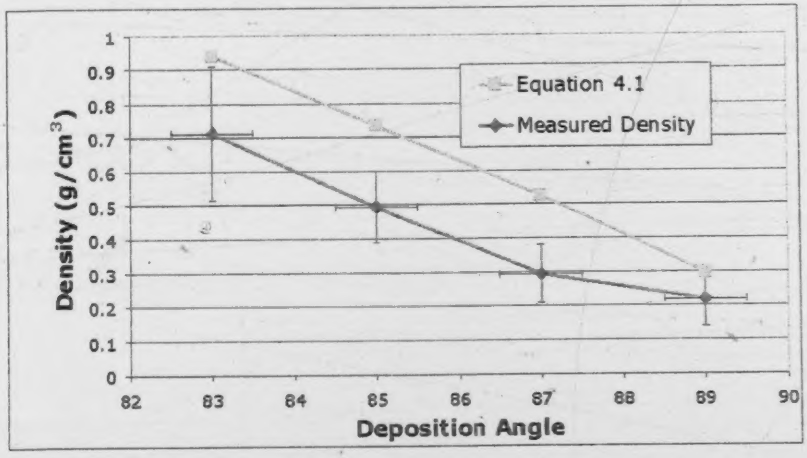

Figure 4.4. Measured and predicted film densities for SiO_2. A comparison between the measured densities for the SiO_2 (here $\rho_{(\alpha=0)}$ = 2.2 g/cm^3) film set shown in Figure 4.2 and the predicted values given by Eq. 4.1 show a similar trend with deposition angle.

4.2.3 Conclusions from Flux Incidence Angle Study

In §4.2, the effect of increasing flux incidence angle on the growth of GLAD microstructures is shown. Using the multi-angle deposition apparatus illustrated in Figure 4.1, it was shown that for SiO_2 with a substrate rotation of approximately 0.1 RPM (r=15Å/sec), helical growth is well formed to α=85°, and begins to degrade for higher incidence angles as enhanced shadowing increases the sensitivity of film growth to structural differences in adjacent columns. The resulting morphology becomes dominated by only a few structures, which capture the majority of flux incident at the film surface. The resulting film geometry more closely resembles sparsely separated pillars rather than helices.

The density of films grown within the glancing incidence regime was also examined, both experimentally and theoretically. Observations in the literature describing a decrease of film density with increasing flux incidence angle were confirmed. A modification of Tait's rule for film density was made, and describes the trend in SiO_2 film density between α=83° to α=89°.

Although not quantitative (the focus here on a single material), the tools developed within this section allow for a further, in-depth study on material dependence on both the film morphology and density within the glancing incidence regime.

4.3 INVESTIGATION OF SUBSTRATE ROTATION AND GLAD MICROSTRUCTURES[†]

4.3.1 Background

In addition to flux incidence angle, the geometric form of microstructures grown within the GLAD regime is dependent on a number of additional factors including the substrate temperature (T), the melting point of the source material (T_m), substrate rotation ($d\varphi/dt$), and the distance between source and substrate (y). Within a single deposition cycle, most of these factors, including the flux incidence angle, are constant – i.e. the material being deposited is not changed, and the substrate is typically held at a stationary α. Hence, the speed of substrate rotation about the φ axis (measured relative to the film deposition rate) is the key parameter determining film microstructure geometry.

[†] This section has been partially excerpted from the article: B. Dick, M.J. Brett, T. Smy, "Effect of Substrate Rotation on the Growth of Microstructures at Glancing Incidence"; Submitted to JVST B (Apr/03).

Generally, substrate rotation affects GLAD morphology in the following fashion: Isolated posts are fabricated when flux arrives isotropically from all azimuthal angles (i.e. $d\varphi/dt$ is 'infinite'); helices form at various pitch lengths for lower substrate rotation speeds; and, finally, oblique columns are formed when $d\varphi/dt = 0$. This general relation between morphology and $d\varphi/dt$ can be gleaned from several experimental [4, 40, 51, 52, 54, 105] and simulation papers [74, 75], and has already been briefly summarized in §2.3.1.4.

Recent research suggests another morphological trend. Liu *et al.*, at the University of Alabama's Center for Materials for Information Technology (MINT), observed that given otherwise identical deposition conditions, the deposition rate of cobalt films increased with increasing $d\varphi/dt$ [10]. This observation was derived from measurements of the film's packing fraction, although data scatter makes it difficult to state that their results are conclusive. In an earlier publication, these same researchers report iron films which display leaf-like columnar growth [9] at high rotational speeds ($d\varphi/dt \sim 30$ RPM, $\alpha=75°$). Although fractal-like growth does occur in stationary, obliquely deposited films, generally it is manifested more compactly, and in a more structured form when the substrate is rotated. Liu *et al.* did not offer an explanation for its occurrence.

In this section, it is shown that the growth behaviour observed by Liu *et al.* also occurs for films deposited at glancing incidence (the present study took place at $\alpha=85°$). An initial explanation of the growth mechanism behind this behaviour is further offered. Although a direct comparison between the work of Liu *et al.* and the depositions at glancing incidence cannot be made, the growth mechanisms identified here are also consistent with the film structure they observed.

4.3.2 Experimental set-up

For this study, several sample sets of aluminum, silicon, bismuth, and silicon dioxide were prepared by electron beam evaporation using the GLAD technique. To ensure each set of films was deposited under identical conditions, a gearbox was designed and constructed to allow the simultaneous deposition of six separate films over two orders of magnitude of rotation speed by stepping up or down the rotation about φ_n relative to the central driving axis, φ_c. These step-up and step-down ratios (relative to the central axis) were 7:1 (i.e. the substrate rotates seven times faster than the central axis), 7/3:1, 1:1 (central axis), 1:2, 1:4, and 1:16. This apparatus is shown in Figure 4.5.

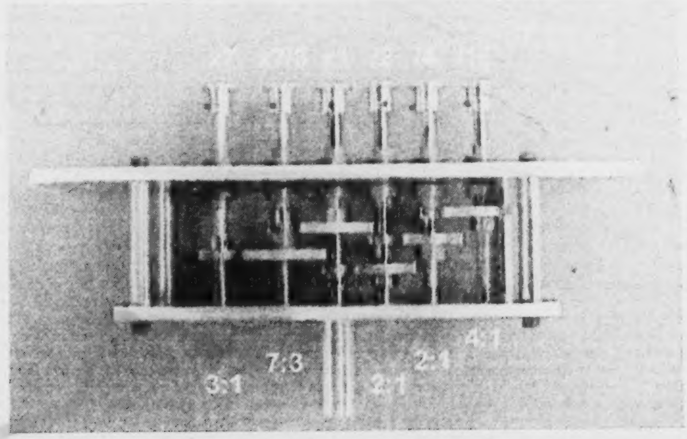

Figure 4.5. Gearbox used to step up and down the substrate rotational speed, dφ/dt. The numbers on the top of image show the relative rotation speed (compared to the central axis) at that point, while the numbers below show the gear ratio between an axis and its immediate neighbour.

Using this experimental set-up, several sets of films were deposited at α=85° with the set of parameters shown in Table 4.1. The system base pressure for all these films was typically 4.5×10^{-5} Pa (3.3×10^{-7} torr).

Table 4.1. Deposition parameters for substrate rotation study

Run	Mat.	Pitch at φ_c	Pressure during Deposition	Dep. Rate
1a	Al	400 nm	1.2×10^{-3} Pa (1.0×10^{-5} torr)	10 Å/sec
1b		5 nm		
2a	Si	400nm	2.2×10^{-4} Pa (1.7×10^{-6} torr)	10 Å/sec
2b		5 nm		
3a	SiO_2	400nm	2.2×10^{-3} Pa (1.7×10^{-5} torr)	10 Å/sec
3b		5 nm		
4a	Bi	400nm	2.6×10^{-4} Pa (2.0×10^{-6} torr)	15 Å/sec
4b		5 nm		

4.3.3 *Observations*

4.3.3.1 Si and SiO_2

Generally, films deposited at low substrate temperatures compared to their melting point, such as Si and SiO_2, can be described as Zone I films in the Movchan and Demchishin structure zone model [25, 26]. These films tend to exhibit a small-scale structure which is either nanocrystalline or amorphous, and have growth which is governed primarily by adatom shadowing at the substrate surface. Transmission electron microscopy (TEM) analysis seems to confirm this description for GLAD columns, which typically consist of bundles of fibres with material dependent diameters [98, 106]. Consequently, the resulting film structure can be interpreted primarily using geometrical models and, hence, more easily predicted and controlled.

Figure 4.6 shows a typical SEM micrograph collage of silicon dioxide films grown at varying rotational speeds. The pitch and number of turns in the GLAD helices shown agree with that expected given the deposition rate of the film and the rotational speed. The set of films shown here were deposited in two separate cycles (φ_c = 5 nm and 400 nm respectively), under almost identical deposition conditions. The distance between the substrate and the source was much larger than the width across the gear-box controlling the rotation for individual samples; the resulting variation in incident flux ranges from 0.5% (from φ_c to the fastest rotating gear) and 0.7% (between φ_c and the slowest rotating gear). Hence, all samples within a given deposition cycle can be considered as being subject to the same, constant incident flux. The resulting deposition rate, based on film thicknesses measured in the SEM, was observed to be constant for all the samples tested, and suggests that the underlying crystal structure of the film and its resulting density is not significantly affected by substrate rotation. Consequently, the pitch is observed to decrease with increasing rotational speed. As this pitch approaches the size scale for the diameter of the helix arm (typically 50-100nm), the film morphology evolves toward a pillar. The images in Figure 4.6 display the progression from post or pillar growth at $d\varphi/dt > 1$ RPM, and helical growth at smaller rotational speeds. Quasi-oblique columnar growth is observed at $d\varphi/dt = 0.00428$ RPM, but only because the substrate has not been allowed to rotate significantly before the deposition was halted. Silicon films exhibit a similar morphological evolution with $d\varphi/dt$.

Figure 4.7 explicitly plots the change in the deposition rate for SiO_2 and Si films at the substrate surface with rotational speed. Here, the deposition rate is taken as the average rate during film growth. It was calculated by measuring the thickness of the film using scanning electron microscopy and dividing by the time deposited.

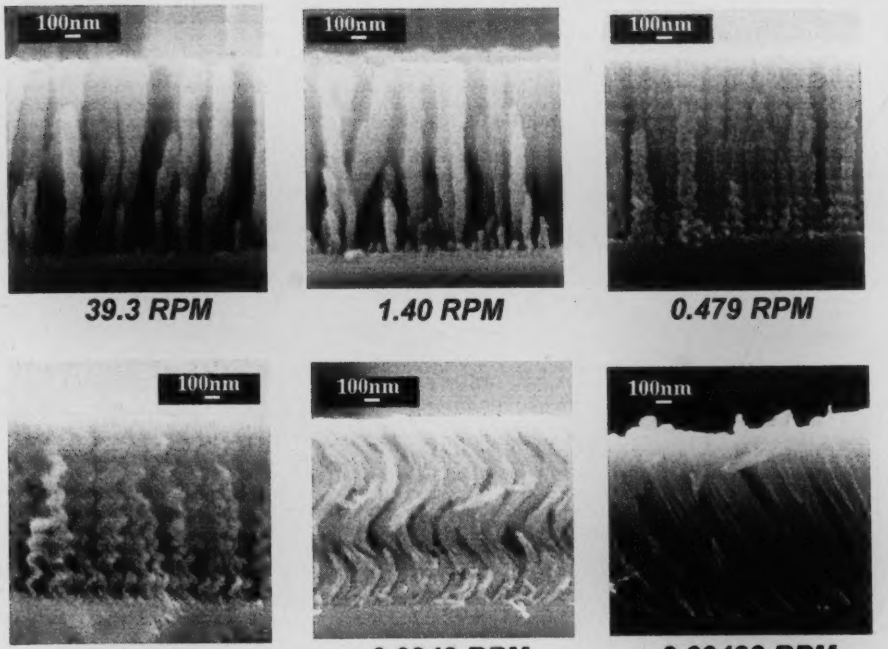

39.3 RPM 1.40 RPM 0.479 RPM

0.159 RPM 0.0343 RPM 0.00428 RPM

Figure 4.6. Films of SiO_2 grown at various rotational speeds (shown below each image). Pillar growth occurs when $d\varphi/dt$ > 1RPM (at a deposition rate of 10Å/sec for normal incidence), while helical growth occurs more clearly for $d\varphi/dt$ < 0.5 RPM.

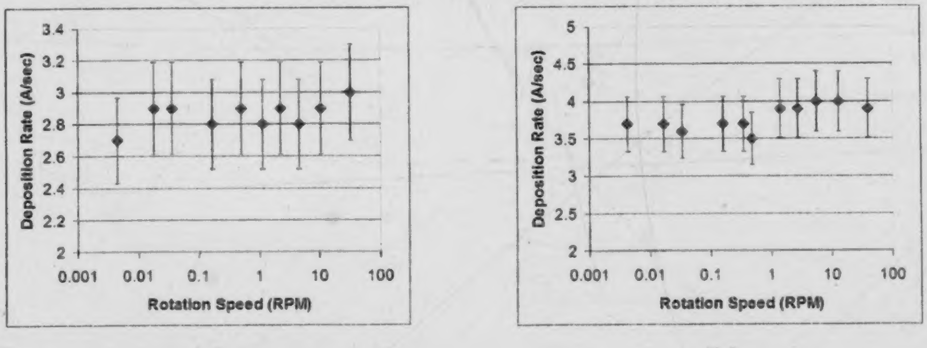

(a) (b)

Figure 4.7. Average deposition rates vs. rotational speed for (a) silicon, and (b) silicon dioxide. Slight variation between $d\varphi/dt$ < 1 RPM and $d\varphi/dt$ > 1RPM may be expected due to changes in the system conditions for the two deposition cycles required to cover the rotation range shown.

These plots show that despite the increase of *dφ/dt* from 0.00428 to over 40 RPM (over four orders of magnitude), no appreciable variation in the average deposition rates (i.e. film thickness) at the substrate was observed. This conclusion contrasts the results of Liu *et al.*, which noted that increasing the rotation speed during film growth resulted in a slight increase in cobalt film thickness[†] [10] and the growth of a leaf-like microstructure for iron [9]. I believed that a similar material dependency on structure form and evolution might occur during film growth at glancing incidence. The results of my investigation are shown in the next section.

4.3.3.2 Bismuth

Silicon and silicon dioxide films both have a relatively high melting point – T_m=1687 K and ~1710 K respectively – allowing them to fall more traditionally into the Zone I structure described by the Movchan and Demchishin SZM. Bismuth, with its significantly lower melting point of 544 K, has a $T/T_m \sim 0.8$ which typically is classified as a Zone III structure (using a similar modeling scheme). However, this model described films deposited onto substrates at *normal* incidence, a key difference from these films, which have been deposited at *glancing* incidence. The shadowing effect at oblique angles is enhanced, and shifts the classification boundaries for the standard SZMs towards higher substrate temperatures. In other words, it takes a higher ambient temperature for adatoms to obtain sufficient energy to overcome the inherent shadowing on the substrate surface.

Figure 4.8 shows a typical SEM micrograph collage of bismuth films grown at varying rotational speeds deposited under the conditions given in Table 4.1. Bismuth follows a similar morphological trend as silicon and silicon dioxide, although its structure is not as clearly defined due to the ability of adatoms to move and re-organize within the growing film (i.e. geometrical shadowing may govern the initial growth mechanics and film porosity, but bulk diffusion governs the ability of incident molecules to form a cohesive crystal structure and/or fill in pores that may exist on the film surface). Pillars are grown for $d\varphi/dt$ > 1.5 RPM, and exhibit widening of the structure with film thickness. This broadening may be due to heating of the substrate, which, due to the relatively low melting point of bismuth (in comparison to the other materials used in this study) increases the diffusion length for adatoms on the film surface.

[†] Their reported change in film thickness amounted to ~20% for a change in $d\varphi/dt$ of 0.22 to 22.2 RPM. However, the considerable scatter in their data makes this percent change in thickness suspect, if it exists at all

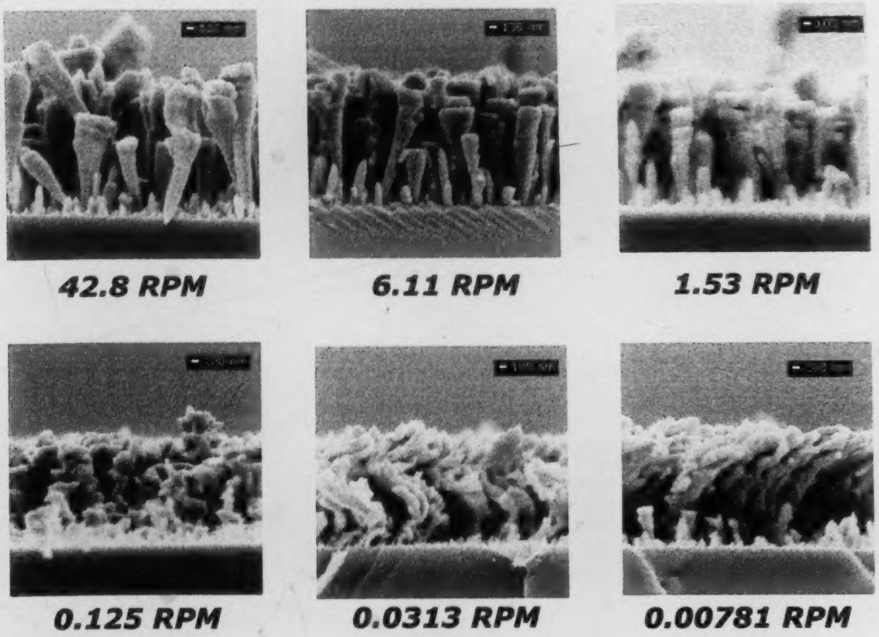

42.8 RPM **6.11 RPM** **1.53 RPM**

0.125 RPM **0.0313 RPM** **0.00781 RPM**

Figure 4.8. Films of Bi grown at various rotational speeds (shown below each image). Although not as clearly defined as the SiO_2 films shown previously, helical growth appears to occur for $d\varphi/dt < 0.125$ RPM, while pillar growth appears at higher rotational speeds.

Figure 4.9 explicitly plots the change in the deposition rate for Bi at the substrate surface with rotational speed. The rate of film deposition at the substrate is observed to change with rotation speed, reaching a minimum value of around 5Å/sec at $d\varphi/dt \sim 0.1$ RPM. This substrate rotation speed appears to correspond to the point of transition between helical and pillar growth: for lower and higher rotational speeds, this deposition rate increases. The mechanism behind this observed behaviour around the transition between helical and pillar growth is not well understood. It is believed, however, that this effect is related to the creation of a stable shadowing condition at the substrate surface due to the quasi-stationary direction of incident flux. At both low and high $d\varphi/dt$, the flux source can be thought as stationary from the perspective of the substrate: In the former, the flux source arrives from one direction, while in the latter, the flux can be thought to arrive simultaneously from all points along the azimuth described by α. Within the transitional region between pillar and helical growth, however, the flux direction will noticeably shift from the substrate's perspective, giving rise to an unstable shadowing condition and a poorly defined structure.

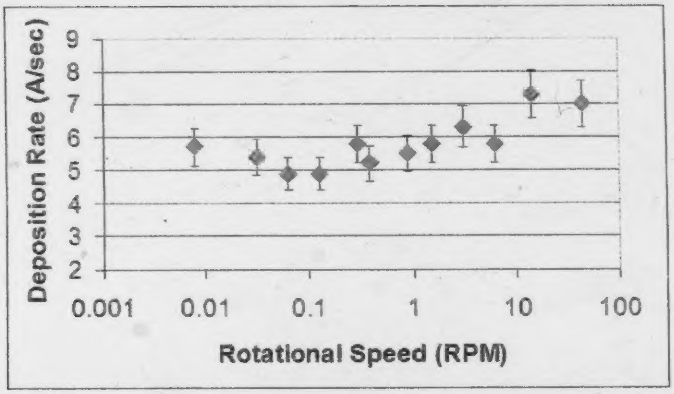

Figure 4.9. Average deposition rates vs. rotational speed for bismuth. The deposition rate appears to reach a minimum value at the point of transition between helical and pillar growth (dφ/dt ~ 0.1 RPM). This rate increased slightly for smaller rotational speeds, and upwards of 40% of its minimum value for higher dφ/dt.

4.3.3.3 Aluminum

Aluminum GLAD films are shown in Figure 4.10. Some adherence of these films to the general morphological evolution observed in previous film sets is seen. For example, pillar like structures are observed for *dφ/dt* > 1 RPM, while helical-like structures are observed when *dφ/dt* < 0.1. However, the occurrence of both an increase in deposition rate of the film with increasing rotational speed, and the dependence of faceting occurring within the pillar film structure, is considerably different than that observed in either Figure 4.6 or Figure 4.8. TEM analysis of these films showed them to have a face-centred cubic, monocrystalline structure. This crystal structure is consistent with its bulk form [107] and measurements on normally deposited aluminium thin films [108].

At slow rotational speeds, the aluminium films have a helical microstructure, which degrades as *dφ/dt* increases to 0.28 RPM. At *dφ/dt* = 1.5 RPM the aluminum film has a "mushroom" structure where its base is thin and appears to spread out with increasing film thickness. The tops of these structures are both flat and consistent in height with their neighbours. As *dφ/dt* increases, the number of structures with a facetted peak increases relative to those that have a planar top. Correspondingly, there is an increase in the film's average thickness as *dφ/dt* increased. At a rotational speed of *dφ/dt* = 42 RPM, the peaked structures are in the majority, and the thickness of the film is approximately twice that of the film grown at lower rotational speeds.

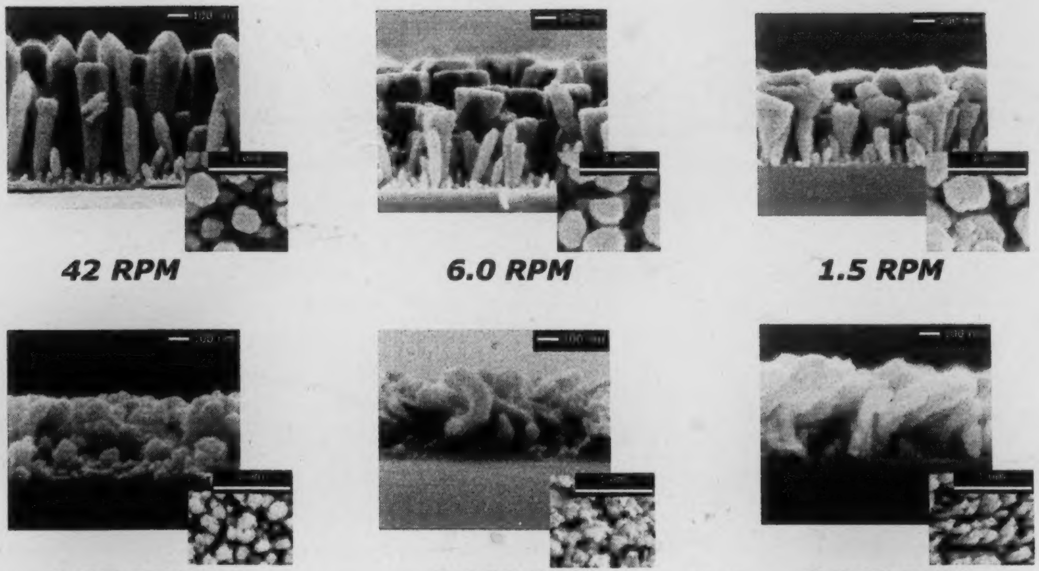

42 RPM **6.0 RPM** **1.5 RPM**

0.28 RPM **0.069 RPM** **0.017 RPM**

Figure 4.10. Films of aluminum grown at various rotational speeds (shown below each image). The films deposited at dφ/dt=1.5 RPM shows a flat top structure while the film deposited at dφ/dt = 42 RPM shows peaked structures. Helical growth begins to appear for dφ/dt =0.07 RPM. Faceting is clearly visible in all the films, particularly those grown above 1 RPM. TEM analysis showed the crystal structure of the film to be simple cubic.

The thickness of the aluminum films show a decrease of greater than 50% over less than two orders of magnitude change *dφ/dt* (see Figure 4.11). These deposition rates at the substrate reach a minimum between 0.1 and 0.3 RPM before recovering somewhat at lower rotational speeds. Similar to the bismuth films discussed in the last section, these results appear to occur at the transition between helical and pillar growth. Hence, a clear dependency of the deposition rate on *dφ/dt* exists, despite all samples being subjected to same density of flux. These observations are consistent with the cobalt and, particularly, the iron films grown by Liu *et al.* (although the latter research was undertaken at a significantly lower flux incidence angle) but are in sharp contrast with the earlier results shown for both Si and SiO_2. This issue shall be discussed in the next section.

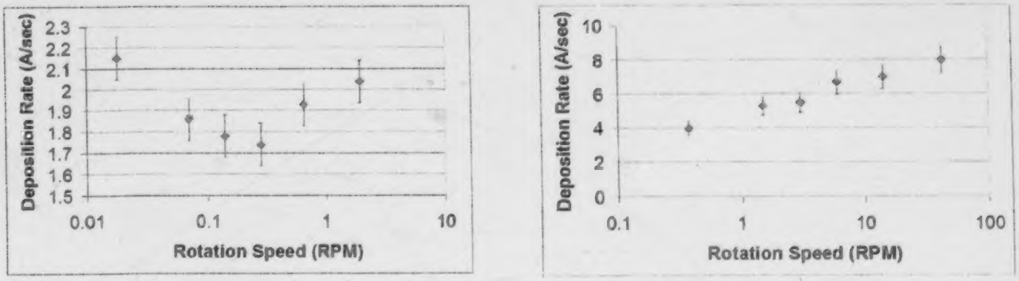

(a) (b)

Figure 4.11. Average deposition rates vs. rotational speed for aluminum. The deposition rate appears to reach a minimum value at the point of transition between helical and pillar growth (dφ/dt ~ 0.3 RPM). Because these two deposition cycles had a lengthy time interval between them, they cannot be directly compared due to potential changes in system conditions. The 400 nm pitch cycle is shown in (a), while the 5 nm pitch cycle is shown in (b).

4.3.4 Discussion

The melting point of the material being deposited, relative to the substrate temperature, is one of the differences between the aluminum (T_m =933 K), bismuth (T_m=544 K), silicon (T_m =1687 K), and silicon dioxide films (T_m =1710 K). Each material follows the standard morphological trend to form slanted posts, helices, and, finally, pillars with increased substrate rotation. The occurrence of a 'clear' helical or post structure (as compared to Figure 4.6) appears to be more due to the material properties of the film being grown, as opposed to a simple application of geometric shadowing.

For example, why does aluminum, which has a higher melting point than bismuth, not exhibit a helical or pillar structure that is more clearly distinguished? The following sections describe the growth evolution observed in aluminium films shown in Figure 4.10 with the assistance of Dr. Tom Smy (Carleton University) and 3D-FILMS, the ballistic film growth simulator described in detail elsewhere [74] and briefly in §2.4. In §4.3.4.2, the possible effects of crystallinity on the resulting film morphology for both aluminium and bismuth films are examined.

4.3.4.1 3D-FILMS modeling of Substrate Rotation and Adatom Mobility

The investigation of the growth evolution of aluminium films proceeded in an empirical fashion – the simulator's growth parameters were manipulated in a consistent fashion to reproduce the observed aluminium film structures at a specific substrate rotation speed. Hence, the conclusions derived *suggest* rather than determine the mechanisms present during the growth of the aluminium films. In addition to the background details on the 3D-FILMS simulator given in §2.4, the following assumptions were made to further simplify this work:

1. The simulation accounted for only three preferred crystal planes (0°, 45°, and 90° – the latter two being natural planes within the 3D-FILMS simulator).
2. The preferred growth plane has a short diffusion length (i.e. a small adatom lifetime)
3. The diffusion length decreased with increasing rotational speed based on $L = \sqrt{D \times \tau}$, where L is the diffusion length, D is the surface diffusivity, and $\tau = \dfrac{1}{d\varphi/dt}$. This statement is based on an assumed increase in adatom burial rate with increasing substrate rotational speed.

Generally, the interaction between surface potential, anisotropic mobilities and GLAD shadowing is very subtle and was difficult to capture in the simulations. However, this work was able to capture the actual film's morphology by simply adjusting the simulator's adatom mobility parameter. A trend relating the rate of adatom mobility and rotational speed was thus observed; namely, that the mobility must be decreased as the rotation speed is increased to reproduce the structures observed in the aluminium films. These results, shown in Figure 4.12, have morphologies that compare favourably with the actual films shown earlier in Figure 4.10.

The simulated films shown in Figure 4.12 capture both the peaked facetted growth at higher $d\varphi/dt$ and flat structures at low $d\varphi/dt$. In addition, the thickness variation and structure spreading (i.e. mushroom formations) were observed in both the simulation and experimental aluminum films. These structures appear to arise naturally in the simulated film suggesting that the change in film morphology is due to an increase in adatom mobility on the surface causing growth along one crystal plane to dominate over another.

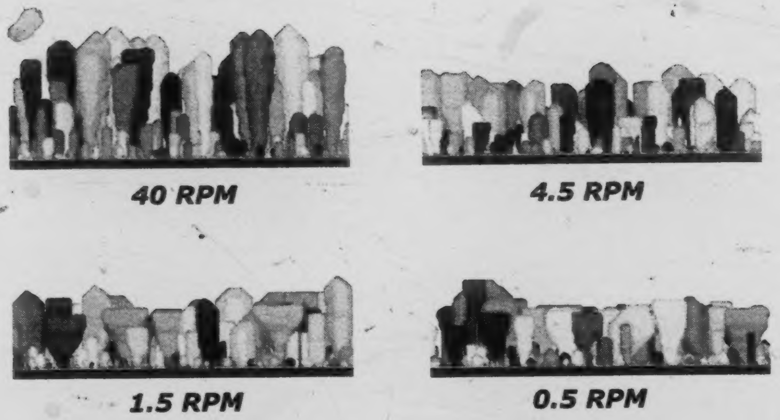

40 RPM 4.5 RPM 1.5 RPM 0.5 RPM

Figure 4.12. 3D-FILMS simulation of a high mobility film deposited at glancing angles with varying dφ/dt. The relative mobilities are μ=2 units for the 40 RPM film, μ=6 units (4.5 RPM), μ=12 units (1.5 RPM), and μ=18 units (0.5 RPM).

To support the conclusion that increasing substrate rotation speed inhibits the surface diffusion of adatoms within films displaying strongly preferred crystal planes, depositions of chromium at the relatively conservative angle of 65° were undertaken. Figure 4.13 shows that at high rotational speeds, the film surface consists of a number of small, facetted peaks. At low rotation speeds, the surface shows a smaller number of peaks with long channels linking film regions, indicating a longer effective diffusion length is required to achieve a smoother surface microstructure.

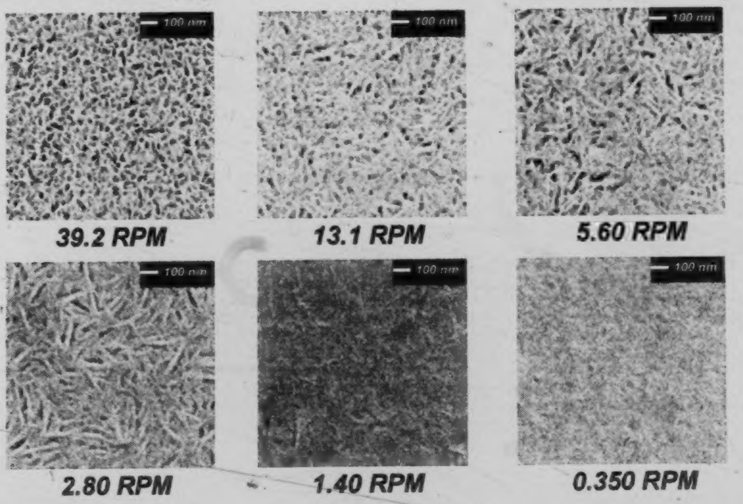

39.2 RPM 13.1 RPM 5.60 RPM 2.80 RPM 1.40 RPM 0.350 RPM

Figure 4.13. The potential effect of substrate rotational speed on adatom diffusion length is apparent from these images of chromium films deposited at α=65°. At low rotational speeds, the film surface is smooth, while at faster speeds the surface roughness increases.

4.3.4.2 Crystallography and its effect on GLAD Microstructures

Considering the capture rate along the film column can provide one explanation for the growth of peaked and flat tops. For unshadowed portions of a growing pillar, the capture rate of flux is proportional to cos(θ), where θ is the angle between the film normal and the incident flux (See Figure 4.14).

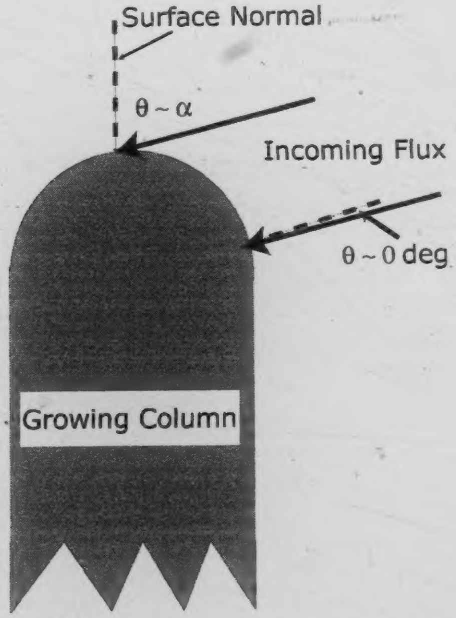

Figure 4.14. Angle of incident flux relative to the surface normal.

Typically, $\theta \sim 5^o$ at the side of the pillar, while $\theta \sim \alpha = 85^o$ at near the pillar apex. Consequently, the level of adatom diffusivity at the sides of the columns induces a "spreading" rate and growth rate of the column. This is particularly true for the flat tops. Thus high diffusivity at low $d\varphi/dt$ would cause the spreading that creates flat top microstructures.

A closer consideration of the GLAD film's crystal structure suggests an alternate (possibly complementary) explanation for the growth mechanism. Epitaxial growth of aluminum on Si(100) substrates has been well documented, and is generally believed due to a lattice matching across four Al[110] and Si[011] plane spacings [109-113]. Lattice matching over the larger cell block changes the 25.5% lattice mismatch between these structures to only a 0.7% mismatch [113].

For example, Hasan *et al.* [113] monitored the growth of thermally evaporated aluminum on Si(100) using reflection high energy electron diffraction (RHEED) and low energy electron diffraction (LEED) during the film's initial growth, and SEM and TEM for the as-deposited thicker films. They found that at four monolayers, an Al(110) bulk diffraction pattern was observed, resulting in structures which consist of regular flat portions separated by inclined surfaces. These inclined surfaces represent imperfect Al(111) surfaces. The low base/deposition pressure (5×10^{-11} torr and 7×10^{-10} torr respectively) and deposition rate (~0.01 monolayer/sec), indicate that their results (confirmed by Zhu *et al.*[109]) should represent a description for the aluminum's preferred thermodynamic state.

A comparison between the film structures reported by Hasan *et al.* and those shown in Figure 4.10 suggest that for low substrate rotation speeds the resulting GLAD film may form the thermodynamically preferred crystal structure. As the substrate rotation speed increases, atoms do not have time to maneuver into their preferred energy position, thus forming an unstable kinetically formed structure. The transition of the GLAD structures from a thermodynamic to kinetic system is supported by the simulation results shown in §4.3.4.1. Here, the 3D-FILMS simulator suggested that the structure form observed in the aluminum films might be due to a decrease in adatom mobility on the film surface caused by an increase in the probability that the adatom is buried by subsequent flux at increasing rotational speeds.

Modification of the film morphology due to a change in preferred crystal orientation may not occur in bismuth. Although some work suggests that epitaxial growth of Bi(111) on Si(111) can occur at low deposition rates (<0.01 nm/sec) and room temperature (i.e. no substrate heating or cooling) using molecular beam epitaxy (MBE) [114], it is generally found that bismuth does not easily form a crystalline structure [115]. In comparison, aluminum reverts relatively easily into a crystalline structure requiring substrate preparation to ensure that the resulting film structure is amorphous.

4.3.6 Conclusions of Substrate Rotation Study

Low mobility films with weak crystalline growth preference show little or no deviation from the general morphological trend at high rotational speeds. These films (in the present examples, silicon and silicon dioxide) form oblique columns, helices, and, finally, pillars as $d\varphi/dt$ increases from 0.00428 to 42 RPM, with no corresponding increase in film thickness.

Low melting point materials, such as aluminum, which exhibit facetted growth due to either surface diffusion or the enhanced growth of preferred crystal planes, show a strong dependency on the speed of substrate rotation as it relates to the rate adatoms are buried by incoming flux. The initial nucleation is thought to be a key in understanding the growth of these films – the glancing incidence of flux tends to multiply any slight growth advantage along crystal planes.

In contrast, low melting points materials that do not exhibit facetted growth (e.g. bismuth) fall between these two types of morphological trends. Slight variations in film thickness with increased substrate rotation, and enhanced pillar thickening as the film grows is observed. However, the appearance of oblique columns, helices, and pillars are more easily discernable than aluminum structures.

It is believed that the growth mechanism identified for aluminum (and to a lesser degree, bismuth) may be an explanation for the cobalt and iron films described in Ref. [10] and [9]. If so, it suggests that the limiting factor on controlling GLAD microstructure growth may be a combination of both material temperature and the crystal structure of the resulting film. The ballistic growth simulator, 3D-FILMS, has shown that when growth along preferred crystal planes is present, the mobility of adatoms is strongly influenced by the rotational speed due to flux burial. This result has been supported by preliminary work on chromium films deposited at varying substrate rotational speeds. The Cr films, although deposited at the relatively conservative deposition angle of α=65°, tend to exhibit a similar growth mechanism. Further studies will be necessary to completely characterize these effects.

Chapter 5 – Competition and Related Growth Mechanics

5.1 BACKGROUND[†]

In common with conventionally dense thin films, GLAD microstructures exhibit self-affine or self-similar behaviour [106, 116]. To illustrate this concept and give some insight into how a GLAD film evolves during its deposition, a SiO_2 post film (deposited at α=85° with normal pitch set to 10nm) is shown in Figure 5.1. The left side of the image shows the complete growth evolution as a side view, while on the right, slices of the film taken at various thickness intervals are displayed.

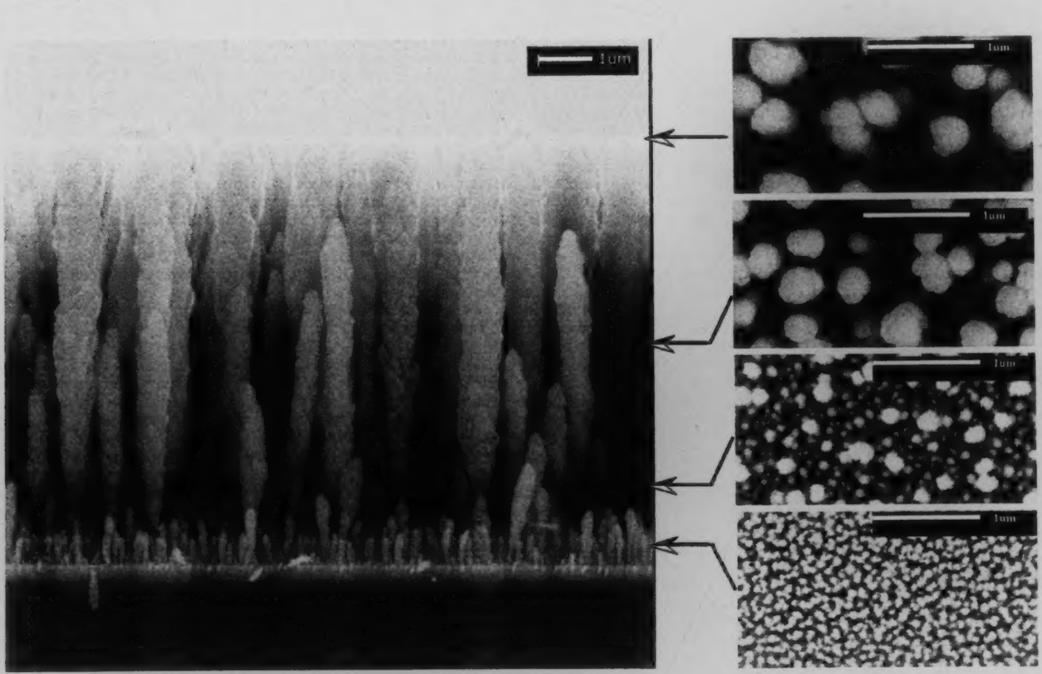

Figure 5.1. Effect of competition on GLAD film grown on non-seeded structures. Slices of the film have been taken at intervals and are shown on the right. The total film thickness shown for the image on the left is 3.89 μm.

Note that the separation of columns occurs early in the growth evolution, as the extreme shadowing at the substrate surface inhibits adatoms from filling in the voids between columns. This behaviour is an extreme example of what is classically referred to as Zone I behaviour: self-shadowing is the dominant growth mechanism, and adatom diffusion is limited [26]. A simple analogy, referred to as the 'grassy lawn' model, is often used to capture the essential concepts of these growth conditions [117]: Blades of grass (representing the columns) grow proportional to the amount of light they receive (i.e. flux density). This circumstance introduces positive feedback into the growth; if a blade overgrows its neighbour, it receives more light flux, and has a higher likelihood of shadowing its neighbours, thus suppressing their rate of growth. For thin films, adatom diffusion tends to smoothen out the surface in the length scale over which it operates, while shadowing tends to magnify surface roughness [118].

[†] This chapter has been partially excerpted from the articles: B. Dick, M.J. Brett, T. Smy, "Controlled Growth of Periodic Pillars by Glancing Angle Deposition"; J. Vac. Sci. Technol. B **21**, 23 (2003), and B. Dick, M.J. Brett, T.J. Smy, M. Belov, M.R. Freeman, "Periodic Sub-Micron Structures by Sputtering"; J. Vac. Sci. Technol. B **19**, 1813 (2001). Used with permission of the American Vacuum Society (2003).

Column competition, extinction, and broadening are typically observed in films deposited by the GLAD technique (e.g. the SiO_2 pillar film shown in Figure 5.1). Transmission electron microscopy (TEM) images suggest that column broadening correlates on the nanometer scale with bifurcation of the fibres that constitute the columns [98], and, due to the observed similarity in column morphology, appears to result in film growth following a scaling law [119].

The effect of columnar competition and thickening may pose a fundamental limitation on engineering microstructures. In addition, these effects may be detrimental for those applications that require a consistent microstructure throughout the film thickness. However, recent work has suggested that the onset of competition and columnar thickening effects in GLAD films may be delayed through the use of a pre-fabricated seed layer and an in-depth understanding of how the film density is affected by flux incidence angle.

5.1.1 A case for α-dependent film density

Both simulated and experimental studies show that the film density (ρ) is primarily a function of flux incidence angle [30, 74, 102-104]. Clearly, measured densities reported between different laboratories can vary widely due to differences in the respective deposition processes and source materials. In addition, some laboratories reported the film density as a normalized value i.e. $\rho_o = \rho / \rho_{bulk}$. Regardless of how these densities are reported, film density is generally observed to fall with increasing flux incidence angle (see §4.2).

Decreases of up to 50% are commonly reported in ρ for films deposited between α=50° and α=85°. This decrease in film density is most clearly apparent for α>75°, as has been shown in Figure 2.2, i.e. in the extremely oblique to glancing angle regime. In this regime, evaporated manganese has shown a reported change in ρ_o from 0.71 at α=75° to 0.40 at α=87° [104] while sputtered tungsten has shown a change in ρ_o of over 40% between a film deposited at α=75° and a film deposited at α=85° [30, 50].

5.1.2 Constant Film Density and the Evolution of Pillar Microstructures

To maintain a constant density at a given flux incidence angle, increases in the surviving pillar diameter, δ, have been shown to be compensated by a corresponding increase in the average pillar separation, *s*. The ratio of these two parameters is thought to be thickness invariant and dependent on the flux incidence angle (α), i.e. $s/\delta = \eta(\alpha)$ [119]. This property arises through the competitive effects linked to the arrival of flux at a given region on the substrate surface. This incoming flux rate is dependent only on its incident angle.

To better clarify microstructure evolution, films grown on pre-patterned substrates have been studied. It was thought that the columnar competition may be minimized by optimizing the seed topography to the observed s/δ factor in similar structures grown on flat substrates.

The average separation of aperiodic columns can be determined by scanning probe measurements of GLAD film topography, and is dependent on the thickness of film (see Figure 5.1). This separation (governed theoretically by Tait's equation) was obtained using a Digital Instruments Dimension 3100 Scanning Probe Microscope (SPM) by explicitly measuring the distances between surviving columns and averaging the results. These measurements resulted in *s* values on the order of a few hundred nanometers for film thicknesses of one to two microns at $\alpha \sim 85°$. The average diameter of columns at a given film thickness was calculated using a JEOL 6301F (Field Emission Scanning Electron Microscope) to obtain a plan image of the film, which was analyzed using the computer software program, ScionImage, to separate regions of columnar growth from the voids.

Using the assumption that the column tops are circular, their average diameter could then be calculated by measuring the pillar count density.

With the procedure described above, the s/δ factor was obtained for each of the thickness slices of the SiO_2 pillar film shown in Figure 5.1. The ratios are presented in Figure 5.3

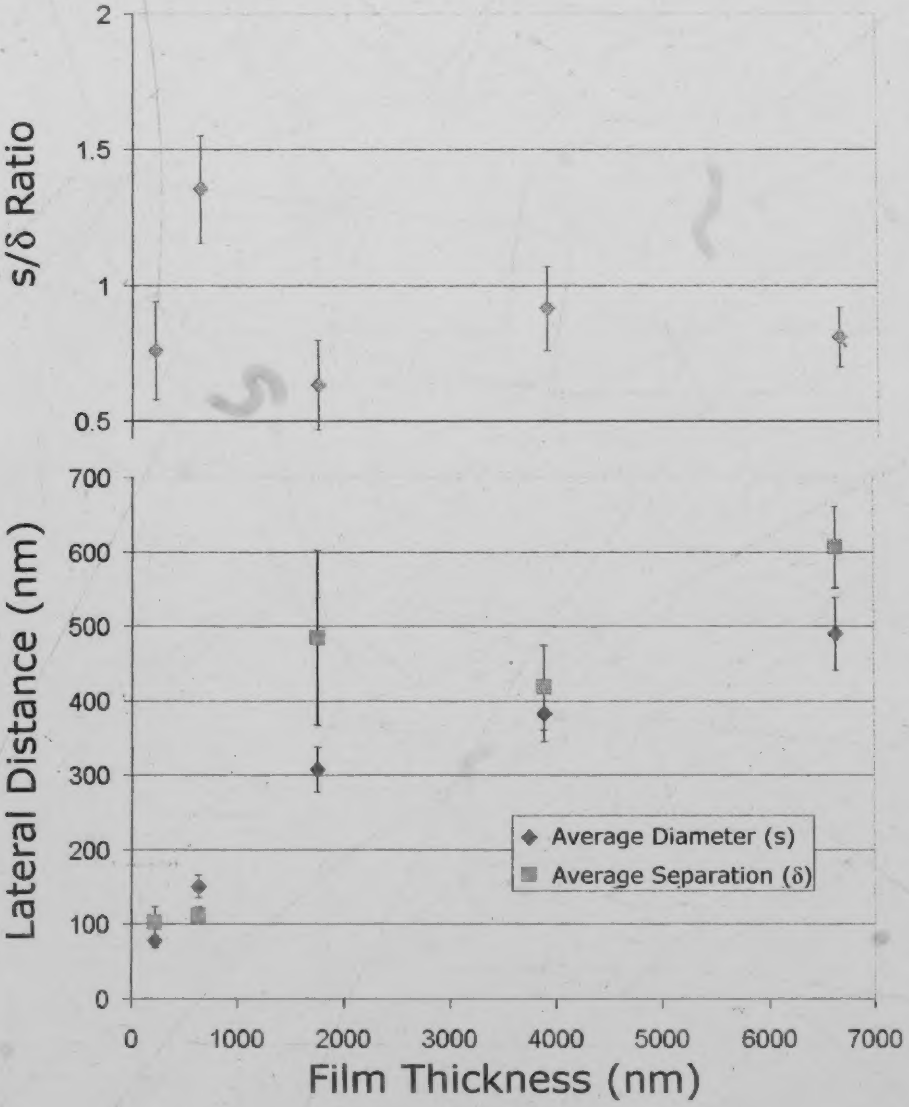

Figure 5.3. Evolution of the pillar diameter and separation during film growth. Estimates of the average diameter and spacing of GLAD pillars is plotted versus film thickness (lower panel). Although these values increase with thickness, their ratio remains approximately constant (top panel).

Although representing preliminary measurements of a single film, Figure 5.3 *suggests* that a constant s/δ value is adhered to throughout the film's growth. This ratio, measured as 1.31±0.16, corresponds to a normalized areal density of 0.47±0.18 assuming each pillar has a circular cross-section. For this calculation, the s/δ factor at a film thickness of 640nm has been excluded, as the measurement for average diameter exceeds that of the average separation between pillars. This indicates an overlap in microstructures on the surface, which does not correspond with SEM images.

The data in Figure 5.3 show significant scatter, particularly for film thicknesses between 500 and 2000 nm. These deviations arise through the difficulty in determining which columns are still contributing to overall film growth. It has been suggested that a ray-tracing program may be applied to this problem to more accurately determine which columns are receiving flux and thus should be used in the s/δ calculation [120]. Until such a study is undertaken, the s/δ factor shown above will be used to help guide later film growth experiments.

To understand how a pre-fabricated seed layer may help diminish the effect of competition within a subsequently grown GLAD film, a simple thought experiment ("Gedankenexperiment") might be applied. Let us consider a seed topography consisting of dots with 50nm diameter, 80nm height, and 600nm separation. The flux incidence angle is set to 85°. For a periodic film, the period of the underlying seed lattice, p, can be substituted for s. Initially, a pillar film grown on this substrate will have a high p/δ factor (i.e. $p/\delta = 125$) compared to a typical value of $s/\delta = 1.25$ to 2.5 for an aperiodic film grown under the same conditions. To compensate for this discrepancy, the pillar diameter increases. During this stage of broadening, the onset of columnar competition is delayed until p/δ reaches its equilibrium or normal value. Competition effects are observed to occur more readily when the pillar diameter reaches the equilibrium s/δ value (i.e. in this case $\delta \sim 240$ to 480nm).

The remaining portion of this chapter describes the investigations on two of the parameters affecting the evolution of GLAD deposited periodic microstructures: flux angular distribution ($\Delta\alpha$), and seed period. In addition, a number of simulations that were undertaken to help further and guide these studies are presented.

5.2 3D SIMULATION WORK AND FINDINGS

As in §4.3, 3D-FILMS (described in detail elsewhere [74] and briefly in §2.4) was again used to provide additional insight into the problem of competitive growth in GLAD films. The choice of using this simulator for this investigation was based on its previous success in describing some of the growth characteristics observed in periodic GLAD films [8].

The parameters adjusted during the simulation runs in this section are shown in Table 5.1.

Table 5.1. Adjusted parameter for 3D-FILMS simulations

Parameter	Simulated values	Section
Seed period	"infinity" i.e. no seeds/flat surface to 100 units	§5.2.1 §5.2.2 §5.2.4
Deposition Angle	α=82.5°, 85°, and 86°	§5.2.1 §5.2.3
Angular Flux Distribution	$\Delta\alpha$=0°, 5°, and 10° (about α)	§5.2.3

All other deposition parameters were kept constant. The area of the simulated surface was set to 200x200 units (1230 x 1230 nm if the simulation is scaled based on the diameters of the experimental seed elements) within which the seed topography was defined. Individual seed elements were described as cylinders with heights of 8 units and diameters of 13 units. Film densities were obtained by taking slices of the film throughout its growth evolution.

5.2.1 Investigations on Film Density

Variation in density with respect to seed period for films grown over seeds is not observed in the simulation runs. Figure 5.4(a) shows that the simulated films quickly reach a constant density that is maintained throughout their growth evolution. Minor perturbations within each density curve result from the limitations of a finite simulated film area, and would be expected to decrease as the simulated area is increased.

Additionally, Figure 5.4(b) supports experimental results indicating that flux angle is the primary factor determining film density. Here, films deposited under identical conditions but with differing incidence angles (α=82.5° and α=86.0°) have been modeled. At lower flux incidence angles, simple geometrical analysis shows that the shadows cast by adatoms or defects on the substrate surface are diminished. Because the substrate temperature is assumed not to change appreciably with flux incidence angle, the adatom diffusion length is constant. Hence, the smaller shadowing distance resulting from a smaller α gives rise to denser films as more regions of the substrate are exposed to incident flux.

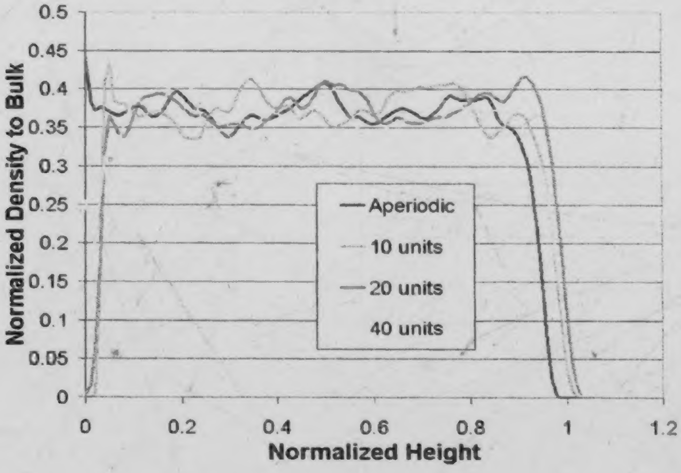

(a)

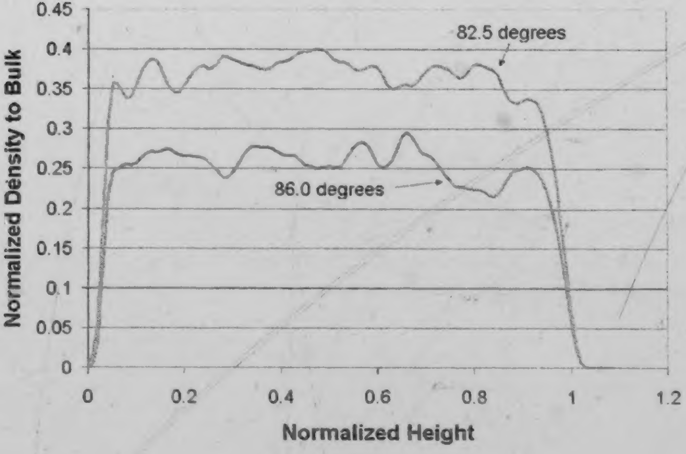

(b)

Figure 5.4. 3D-FILMS simulations of density with respect to seed period (a), and flux incidence (b). Density depends only on the angle of incidence, α.

5.2.2 *Investigations on Pillar Diameter*

Using 3D-FILMS, plan views of the growing film can be obtained at set thickness or time intervals. Figure 5.5 illustrates the effect of competition and seed period on pillar diameter at successive stages of growth for $\alpha=85^\circ$. Since the film density is primarily a function of flux incidence angle, the densities of these films should all approach the same equilibrium value. Hence, pillar diameters should increase with time based on the initial seed separation.

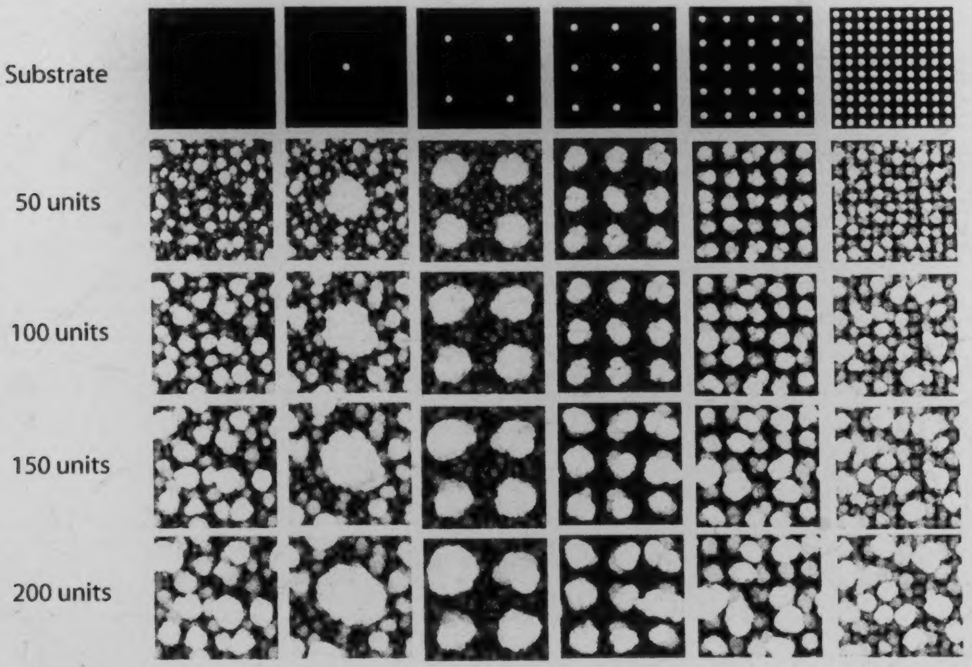

Figure 5.5. Simulated periodic posts at progressive stages of growth are shown as pseudo SEM micrographs. The film thickness, labelled by the number of units of film thickness, increases from top to bottom, while the effect of varying seed period is displayed from left to right.

Simulated films grown at greater initial seed separations exhibit a larger pillar diameter with a corresponding decrease in inter-columnar competition than those films grown on relatively dense seed arrays. At a given film thickness, the cross-over between increased competitive behaviour and increased pillar diameter appears to occur when the seed period is equal to the mean separation of aperiodic pillars grown under similar deposition conditions, s. For example, the 5x5 array has a seed period that is approximately equal to s and, hence, displays more inter-column competition than the 3x3 array. The pillar diameter increases to achieve the equilibrium p/δ factor for films grown on arrays with seed period much larger than *s*. Initially, films begin their growth at a high p/δ factor - based on the underlying seed array - relative to a similarly grown aperiodic film. The film diameter increases to compensate for this disparity, but effectively delays the onset of columnar competition in growth evolution.

Columnar diameters of a growing film are a consequence of both self-shadowing of incoming flux and adatom diffusion length. It is concluded that aperiodic films exhibit an optimal columnar diameter at a given film thickness based on the interplay between these two parameters at the columns location. Hence, for a film grown on a seed period much less than *s*, presuming a requirement for constant film density (or p/δ factor), competition increases in the film because columns are growing within the shadowing region cast by their neighbours. The column diameter cannot grow smaller due to limitations imposed by the diffusion length of incident adatoms on its surface.

5.2.3 Investigations on Flux Angular Distribution

When describing the shadowed region cast by seed elements on the substrate surface, the implicit assumption is that the incoming flux is co-linear (i.e. $\Delta\alpha=0°$). In an evaporation system, with the appropriate system geometry, the angular distribution at the substrate surface can be limited to within ±2° of the expected incidence angle. However, in a sputter deposition the distribution is typically greater than ±5° due to the higher pressures required maintaining the plasma and enabling a sufficient material deposition rate. Here, 3D-FILMS was used to investigate the effects of non-zero flux distribution width. In these simulations the deposition flux was treated as a uniform distribution over $\Delta\alpha$. Therefore if $\alpha=82°$ and $\Delta\alpha = \pm 5°$, the relative amount of incident flux is unity for angles between 77° and 87°, and zero for all other angles. In comparison, one experimental GLAD paper reports the half-width of the flux angular distribution in their sputter set-up as 8° [121]. This value was obtained using the Monte Carlo sputter flux transport simulator SIMSPUD [122]. Hence, the model used in the 3D-FILMS simulations tend to maximize the effect of flux arriving at the outer edge of its angular distribution, compared to what would be observed in an actual deposition.

Figure 5.6 shows the progression of film microstructures grown at Δα= 0° and Δα = ±5°. An additional film set at Δα = ±2.5° was also simulated, but for clarity only the two outer points on the observed trend are shown in this figure.

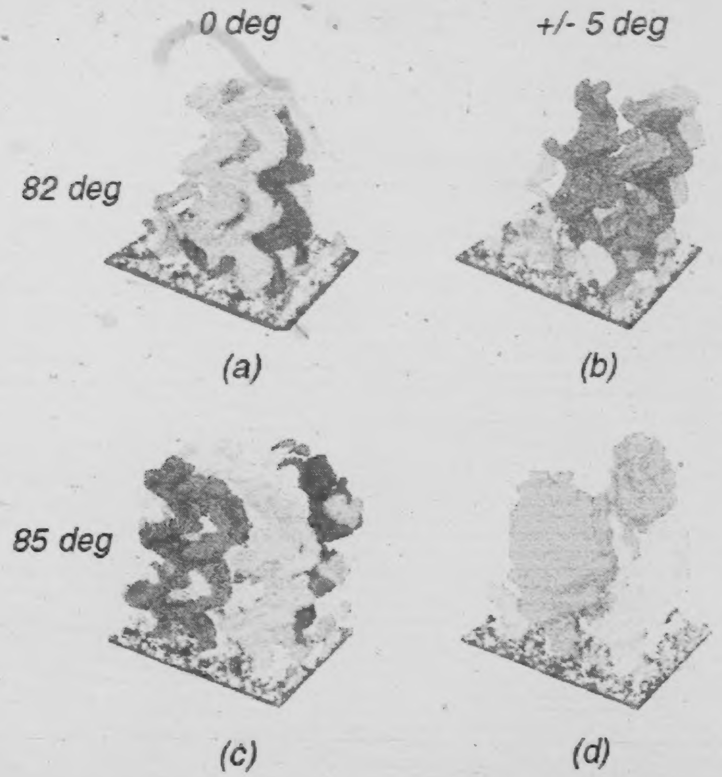

Figure 5.6. Effect of increasing the angular flux distribution width at constant flux incidence and seed separation. All simulations have been run with a seed separation of 60 units. These images have been 'clipped' such that all structures passing outside the simulated cube have been removed in entirety from the view shown. Additionally, the different shading used for the simulated microstructures is only intended to more easily discern individual structures from their neighbours.

For these simulated films, the seed period was kept constant at 60 units. At α=82°, increasing $\Delta\alpha$ from 0° to ±5° appears to have little effect on the overall film microstructure. However, when α=85°, dominant columns on the substrate surface more easily acquire the majority of flux at wider distributions. At α=85°, the corresponding shadowing length cast by individual seeds on the substrate surface is 90 units, which is slightly beyond the seed separation of 60 units. Thus it is expected that dominant columns will shadow neighbours and disrupt the periodic growth. At $\Delta\alpha$=±5°, this shadowed length varies between 79 units (α=80°) and infinity (α=90°). It is probable that it is the portion of the flux incident at the most oblique angles that causes the collapse of the film microstructure to only a few dominant columns. These observations are explored further in §5.3.2f.

5.2.4 Investigations on Seed Period

Figure 5.7 shows the progression of film microstructures for increasing seed separation. For these simulations, both the flux incidence angle and angular distribution were kept constant. The progression from aperiodic (i.e. no seed layer) to highly separated seeds is shown. Under constant density conditions, if the seed period is increased fewer locations for nucleation and growth (shadowing constraints still being in effect) are available. Hence, it is expected that helices should thicken with increasing period to maintain a constant density, provided that p is less than the maximum shadowing length given by Equation 2.5. Helices may thus degenerate into pillars if coil thickening approaches the structure's pitch length. This generalized trend can be observed in the simulated films.

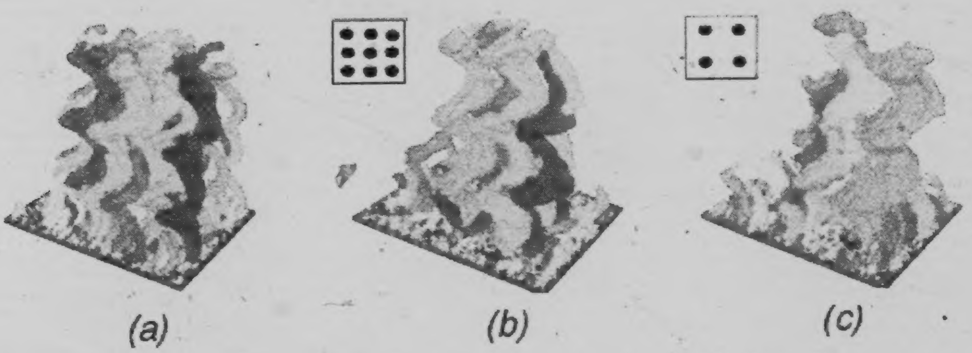

Figure 5.7. Effect of increasing periodicity at constant flux incidence (α=82°) and angular distribution ($\Delta\alpha$=0°): (a) is a simulation on a flat substrate; (b) is a simulation on a seed array with a period of 60 units; and, (c) is a simulation on a seed array with a period of 100 units. The number of array elements within the simulated area is shown in the top left corner of each film image. These images have been 'clipped' in the same manner as in Figure 5.6.

5.2.5 Conclusions

From the simulation results given above, the following observations may be made:

1. Film density is dependent primarily on the incident flux angle.

2. Pillar diameters increase more quickly and are larger before competitive effects between columns begins to occur.
3. Competition occurs more readily in films when the seed separation is much less than the average separation between columns of a similarly deposited film deposited on a flat substrate (s)
4. Helical microstructures are increasingly tolerant to variations in $\Delta\alpha$ as α decreases.
5. Over a limited range, helical microstructures are more easily fabricated as the seed spacing, p, decreases, while the degeneracy and growth of pillar microstructures shows less of a dependence on seed period.
6. There should occur a value of $p_{transition}$ (at a particular α and rotation speed) where the amount of material distributed to the helices (to maintain film density) will make the helical structure indistinguishable from that of a pillar.

In addition, based on previous helical growth work [6, 52, 53], it is observed that the mean separation of helices on a flat surface increases with increasing α. Hence, given the above predictions it can also be hypothesized that:

7. The $p_{transition}$ at which helical growth becomes pillar-like should increase with increasing α, or, conversely,
8. Helical structure at a particular $\Delta\alpha$ and α should degenerate with increasing p.

These observations have been used to guide the research presented in the rest of this chapter.

5.3 EXPERIMENTAL

5.3.1 Set-up

Periodic GLAD films were fabricated using both electron beam evaporation and sputtering on seeded substrates produced by electron beam lithography (EBL). It is useful here to emphasize the difference between these two deposition techniques: Electron-beam evaporation involves the controlled transfer of gaseous atoms from a heated source to a substrate where a film forms. This transfer takes place in an extremely low-pressure environment (between 10^{-6} to 10^{-5} torr), which can be translated into the average travelling distance that a particle will travel before colliding. This distance, referred to as the particle's mean-free path (m.f.p.), is given by [81]:

$$\lambda = \frac{kT}{133 \times P\pi\sqrt{2}\sigma^2} \qquad [5.1]$$

Where, P is the deposition pressure (in torr), T is the system temperature, and σ is the particle's cross-sectional area (typically 3 Å). For a typical evaporation process, $P=10^{-6}$ torr and T ~373 K yielding a mean-free path of λ = 9.7 m. Hence, particles tend to travel in straight-line trajectories between the source and target.

Sputtering is a process whereby the material is ejected (in its atomic form) from a source surface through the impact of gaseous ions of a heavy inert gas (typically argon). Because the mechanism for matter transfer between source and substrate requires the presence of working gas, the deposition pressure during sputtering is much higher than that of evaporation (usually $>10^{-3}$ torr). This relatively large pressure (i.e. low mean-free path) translates into a high degree of scattering in particles (i.e. a large angular distribution in flux) before they arrive at the substrate.

The substrate seed pattern designed for these experiments consisted of five arrays containing a 10x10 seed matrix. Each seed had cylindrical geometry with a height and diameter of approximately 80 nm (measured by SEM). The centre-to-centre separation between seed elements increased between individual arrays; namely, 600, 900, or 1200 nm. Each element was fabricated directly from the PMMA used during the lithographic process, thereby saving further processing steps typically required for lift-off. Further details on these EBL patterns was given in §3.2.

5.3.1.1 Evaporation

Evaporated films of silicon dioxide were deposited at α = 85°. Both periodic and aperiodic films were deposited simultaneously. For post fabrication, the substrate was rotated at 1-2 RPM. The base pressure of the system for this investigation was typically 1.0μTorr (~100μPa), while the deposition pressure did not exceed

6.0μTorr (~800μPa). The source purity of the SiO_2 was 99.99% and the average growth rate (normal incidence) was 30Å/sec.

5.3.1.2 Sputtering

Both the periodic and aperiodic films were deposited at glancing angles with α set to either 82.5° or 86.0°. As opposed to the evaporated films described above, the periodic and aperiodic films were deposited during different deposition cycles due to the constraints imposed by the deposition apparatus available for the sputtering system. The deposition time was 5hrs for the film deposited at 82.5° (~4 complete revolutions), and 7.5 hrs (~6 complete revolutions) for the film deposited at 86°. A schematic of the deposition geometry is shown in Figure 5.8.

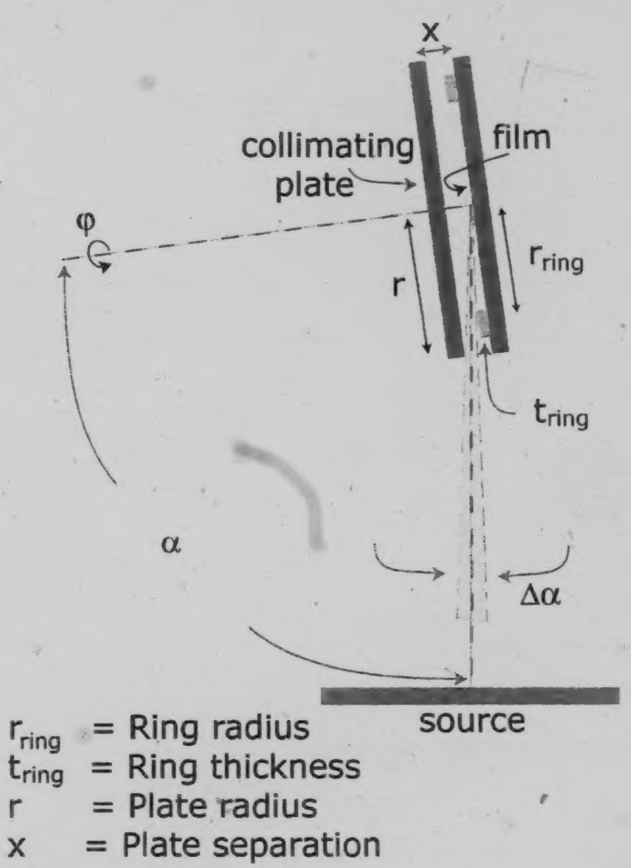
x
collimating plate
film
φ
r
r_ring
t_ring
α
Δα
source
r_ring = Ring radius
t_ring = Ring thickness
r = Plate radius
x = Plate separation

Figure 5.8. Illustration of the deposition geometry for sputtered GLAD films. Flux is collimated by both a secondary plate placed parallel to the substrate at a distance x, and a ring surrounding the substrate. The substrate rotates about the φ axis.

The target was a 7.62cm diameter x 0.32 cm thick tungsten source with a purity of 99.95%. The deposition took place at 300 W (437V) in a background argon pressure of approximately 700μTorr. Using Equation 5.1, the mean-free path for argon atoms can thus be estimated as λ = 6.2 cm. The throw distance was set to 16cm, which is significantly outside the excitation region for argon atoms. To limit the angular distribution induced by scattering, the flux was collimated using a small metal ring with an inside diameter, r_{ring}, of 1.54 cm enclosing the substrate. This ring effectively blocked incoming flux greater than the angle set by ring's thickness, t_{ring} (i.e. α_{max}=90°-$\tan^{-1}(t_{ring}/z)$). To further confine the angular flux distribution at the array, a second plate (diameter = 2.5") was situated parallel to the substrate at a separation x to set a minimum angle on incoming flux (i.e. α_{min}=90°-$\tan^{-1}(x/r)$). Hence, using this set-up, particles entering the gap between the two collimating plates can be thought to be arriving at the substrate with a linear trajectory, though not necessarily with their origin at the source owing to previous collisions within the argon plasma. Table 5.2 shows the parameters for the ring thickness and plate separation distance used for each deposition angle, and the resultant angular flux spread expected. In previous work by Sit *et al.* [121], a 5.08cm diameter target (at a similar throw distance) was used to help limit the flux distribution and grow aperiodic GLAD structures. By using the collimation technique described above, coupled with a slightly lower pressure, a standard 7.62 cm diameter target could be used with equal or better effect.

Table 5.2. Effective angular flux distribution for the experimental set-up

Deposition Angle (α)	**Ring Thickness (t)**	**Plate Separation (z)**	α_{max}	α_{min}	**Flux Spread ($\Delta\alpha=\alpha_{max}-\alpha_{min}$)**
82.5°	2.19mm	1.00cm	85.1°	81.1°	4.0°
86.0°	1.13mm	0.75cm	87.5°	83.2°	4.2°

Substrate rotation was constant and controlled by an external counter sending signals to a vacuum compatible motor inside the chamber. This rate was set to 0.013 RPM for both α=82.5° and α=86°, which resulted in pillar microstructure formation over the majority of the seed arrays, and a helical microstructure in the randomly seeded film. This substrate rotation rate is significantly less the evaporation experiments (see also §4.3) owing to the collimation set-up and sputtering process which resulted in deposition rates of 2.0 nm/min (82.5°) and

1.7 nm/min (86°). Both the evaporated and sputtered films were grown incrementally, with removal of the film from the system between depositions. At each stage of growth, the diameter of the growing pillars was measured using an SEM.

5.3.2 Investigations on Flux Angular Distribution

Generally, GLAD deposition processes require tight flux beam geometry to ensure that the adatom shadowing mechanism on the substrate surface is predominant. Evaporative processes with sources subtending small solid angles from the point of view of the substrate yield this geometry, although they cannot easily be applied to high melting point materials (e.g. tungsten) or to some compound materials.

Standard sputtered physical vapour deposition, in contrast, can deposit a wider range of materials, albeit with a greater flux incidence distribution at the substrate caused by the large target size and flux scattering off the working gas. Several techniques applicable for GLAD have been suggested to narrow the flux distribution incident on the substrate surface, including collimated sputtering [123, 124], ionized PVD [125], and low-pressure, long-throw (LPLT) sputtering [126]. Although Sit *et al.* have shown that by using LPLT sputtering, aperiodic GLAD microstructures might be reliably fabricated [121], it was believed appropriate to follow this lead with a modification of the deposition apparatus to further limit the distribution of flux incident on the surface.

5.3.2.1 Growth of Aperiodic GLAD Films by Sputtering

Using the apparatus set-up shown in Figure 5.8, the results of Sit *et al.* [121] have been confirmed for tungsten films (see Figure 5.9). These films display similar dependencies on the flux incidence angle as evaporated films, particularly an increase of porosity with increasing α. Because the substrate rotation rate was kept constant at 0.013 RPM for both films, the longer deposition time for α=86.0° resulted in tungsten helices with a smaller pitch. Hence, the structure in Figure 5.9(b) is closer to that of a pillar than Figure 5.9(a).

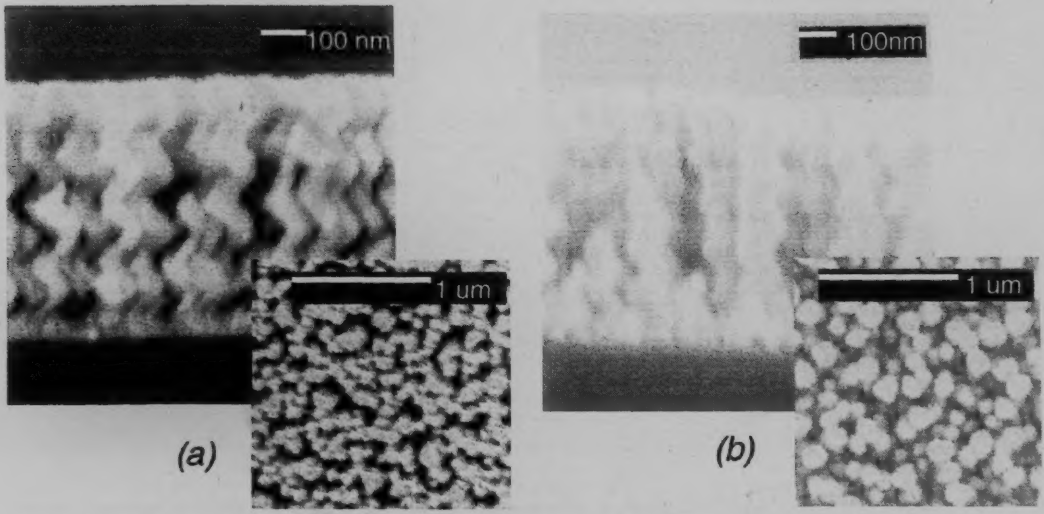

Figure 5.9. Aperiodic tungsten films grown by sputtering at α=82.5° (a) and 86.0° (b). As α increases from 82.5° to 86.0°, the average separation distance between microstructures increases, while the film growth rate changes from 2.0nm/sec at α=82.5° to 1.7nm/sec at α=86.0°.

5.3.2.2 Growth of Periodic GLAD films by Sputtering

Growth at α=82.5°

Tungsten films were sputtered onto periodic lattices at α=82.5°, and are shown in Figure 5.10. According to Eq 2.5, for α=82.5°, the approximate shadowing length cast by the seeds is 607 nm. Hence, increased film growth between columns should occur for seed periods larger than this separation. This effect is clearly observed in Figure 5.10(a,b,c), where film growth between columns for p=1200nm is greater than that for p=600nm.

The transition point between helical growth and pillar growth occurs at a seed separation between 150 and 300nm. Pillars are observed to grow on the majority of the seed arrays, although a slight helical structure appears on the 300nm lattice. A more identifiable helical structure is apparent in the 150nm lattice film (Figure 5.10(e)). The helical structure within the lattice is obscured by growth on the lattice edge. Plan views of each film indicate that the structures are both separated and periodic with an increase in the rate of columnar extinction with smaller lattice periods.

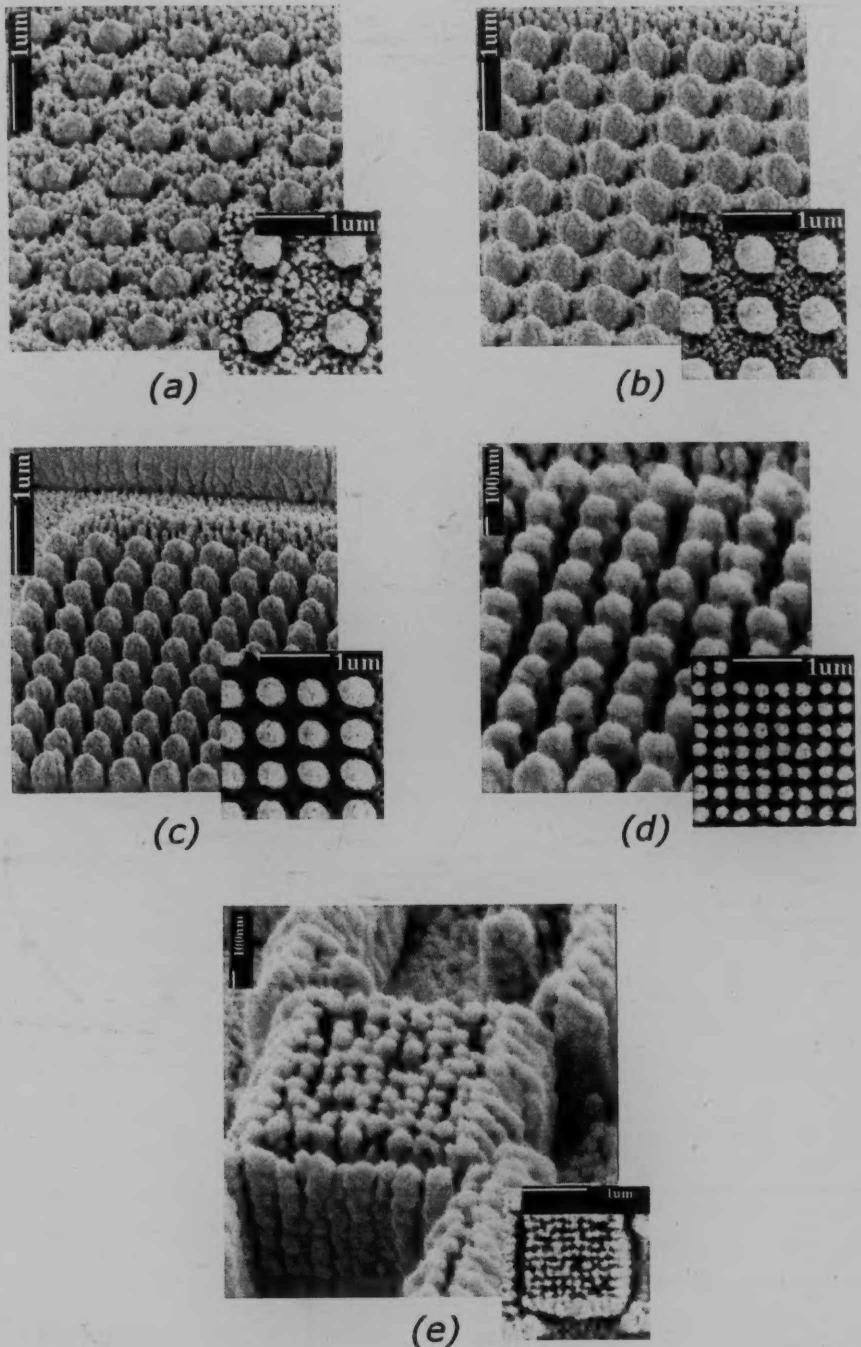

(a) (b)

(c) (d)

(e)

Figure 5.10. Periodic tungsten films grown by sputtering at α=82.5°. The lattice separations for each film are (a) 1200nm, (b) 900nm, (c) 600nm, (d) 300nm, and (e) 150nm. Note that all films were deposited simultaneously, with only the seed period as the independent parameter. A quasi-helical structure is observable in the 300nm lattice film, although it is more clearly identified in the 150 nm lattice film. The growth of structures within the 150 nm array is partially obscured by the lattice edge.

The simulated results at large $\Delta\alpha$ show better helical growth than that observed experimentally. It is thought that for the experimental films the substrate rotation speed needs to be further decreased to grow improved helical microstructures on the array elements.

Growth at α=86.0°

Figure 5.11 shows periodic tungsten films grown at α=86° by sputtering. The transition between pillar and quasi-helical growth occurs gradually, allowing for only a 'region' of transition to be estimated. The quasi-helical structure at 300nm (highlighted within a blue circle in the figure) is more easily visible in comparison to the film grown at 82.5°, which implies that the helical region has been shifted to higher seed separations at α=86° compared to α=82.5°. These observations are in accordance with our simulated results.

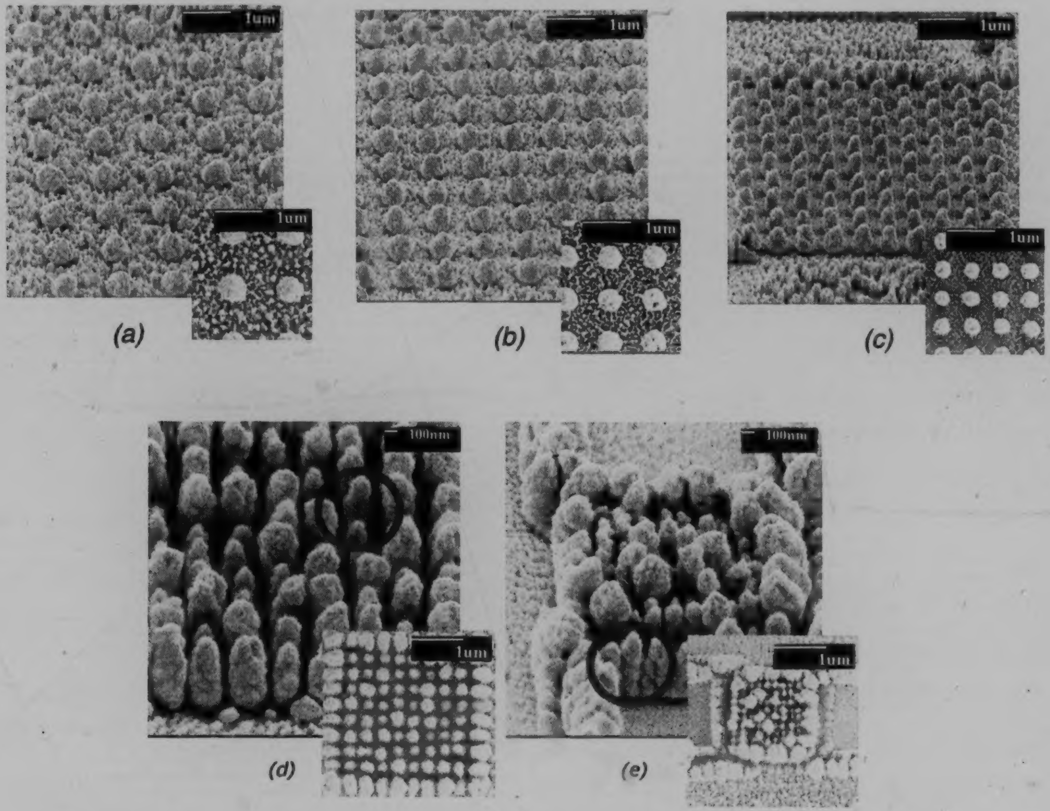

(a) (b) (c)

(d) (e)

Figure 5.11. Periodic tungsten films grown by sputtering at α=86.0°. The lattice separations for each film are (a) 1200nm, (b) 900nm, (c) 600nm, (d) 300nm, and (e) 150nm. Quasi-helical growth is initially observed in (d), where it is highlighted in blue (note the coils banding upwards from right to left). This helical growth is more clearly observed in (e).

5.3.3 Investigations on Competitive Growth

A comparison between films deposited under similar conditions indicates that columnar competition occurs more readily in sputtered films compared with evaporated films (Figure 5.12). This fact may be due to the different material properties, a shift in the equilibrium separation of structures caused by the difference in flux incidence angle between the two films, and/or the increase in angular flux distribution at the surface. Of these factors, however, the angular flux distribution width is the largest effect. Quantitatively, competition is observed clearly in the sputtered film by 1μm of film thickness, while a similar effect is not observed in the evaporated films until almost 1.7μm. Pillar diameters also appear larger and have a broader size distribution in the sputtered films than in those grown by evaporation due to the enhanced competition observed in sputtered films.

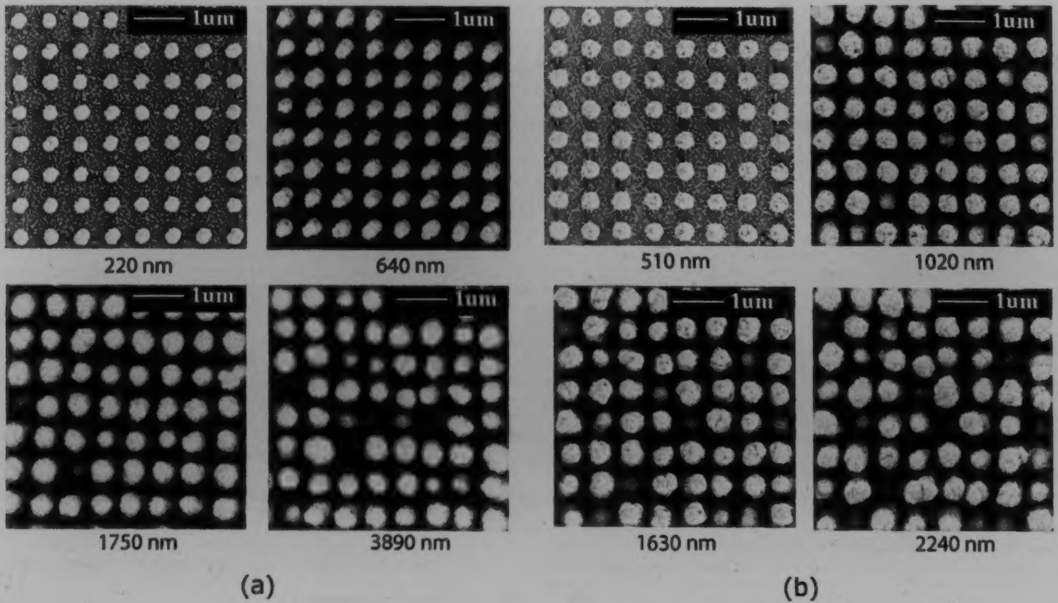

Figure 5.12. Comparison between periodic GLAD films grown by evaporation and sputtering, using plan views of their growth over time. Each film was grown on a seed array with p=600nm and is shown at four stages in its growth evolution (film thicknesses are shown below each image panel): (a) shows an evaporated SiO_2 film grown at $\alpha=85^o$ ($\Delta\alpha=2^o$), while (b) shows a sputtered W film grown at $\alpha=86^o$ ($\Delta\alpha=6^o$).

In §5.2.4 it was shown that helical growth in sputtered GLAD films can degenerate into only a few dominant columns because of the large $\Delta\alpha$ of arriving flux. Why does this effect occur? Let us first consider what is meant when incident flux has a given angular flux distribution; for example, if $\alpha=85^o$ and

$\Delta\alpha$=4°, the majority of flux arrives between $\alpha_{min} = 83° < \xi < \alpha_{max} = 87°$. Recall that a pillar is simply a helical microstructure within which the pitch is indistinguishable. Hence for large seed separations (i.e. on the order of 1μm), although a helical structure may form at α=85°, the component of incoming flux arriving at the lower angles fills in gaps between film structures. Simultaneously, flux arriving at the higher angles tends to smooth out the fine structure within the helical coils. At smaller seed periods, shadowing by neighbouring structures diminishes this "filling" effect as higher incidence flux is blocked. Competition effects increase resulting in an increase in columnar extinction and a decrease in flux accumulating between film structures. As a result, when the seed period is less than *s*, the equilibrium spacing of structures in an aperiodic film, quasi-helices are formed. When $p > s$, helices degenerate into posts with film growth between the structures, while a transitional region between pillars and quasi-helical behaviour is observed to exist about $p = s$.

5.3.4 Investigations on Pillar Diameter

The onset of columnar competition can also be observed in periodic films by plotting the pillar diameters and average column count per unit area at a given film thickness. Size parameters were estimated using plan view SEM micrographs of the film surface, while AFM topography scans were used to estimate the pillar count density. Plots for both the sputtered and evaporated films are shown in Figure 5.13 and Figure 5.14 respectively.

Pillar diameters in aperiodic films are observed to increase with increasing film thickness with a proportional decrease in the number of columns per unit area (see Figure 5.1), resulting in a constant film density throughout the film's growth evolution. Simulated periodic films (Figure 5.5) also exhibit this trend, as do the experimentally grown films imaged in Figure 5.12.

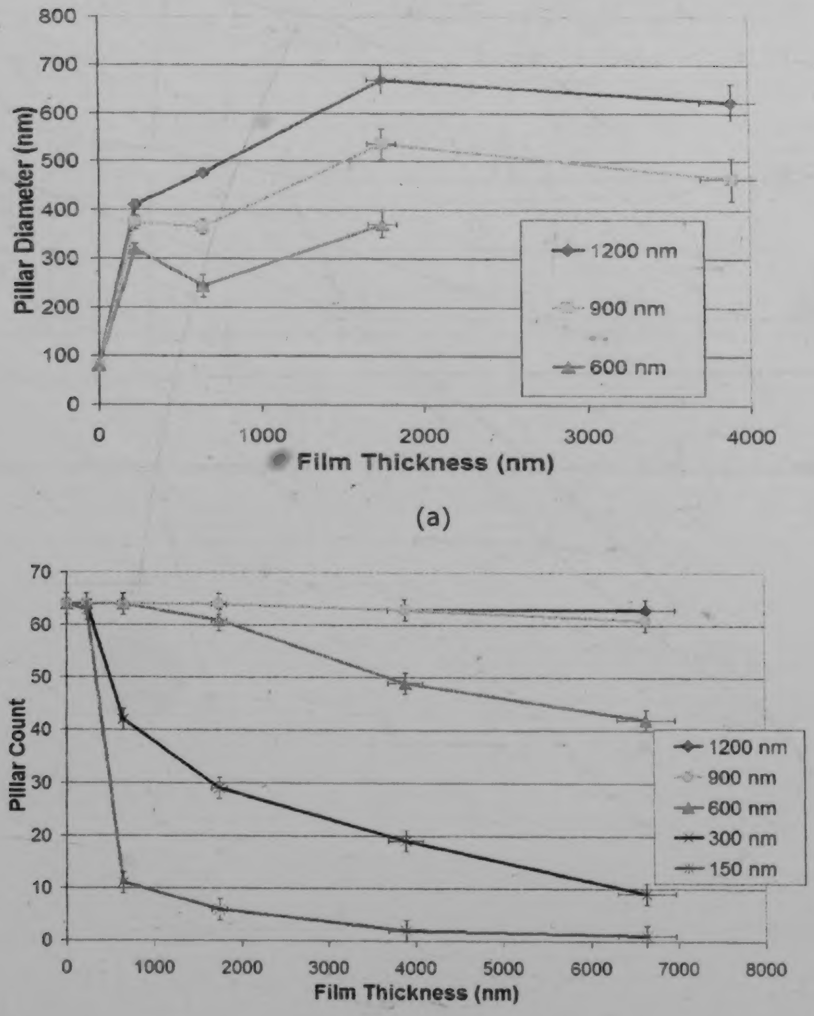

(a)

(b)

Figure 5.13. Increase of pillar diameter (a) and decrease in average pillar count density (b) for periodic silicon dioxide films deposited by evaporation at α=85°. Because of the rapid increase in competition for seed arrays less than 600 nm (as is evidenced in the rapid fall off of pillar count density observed in (b)), only pillar diameters of this seed period and higher could accurately be determined throughout the film growth cycle.

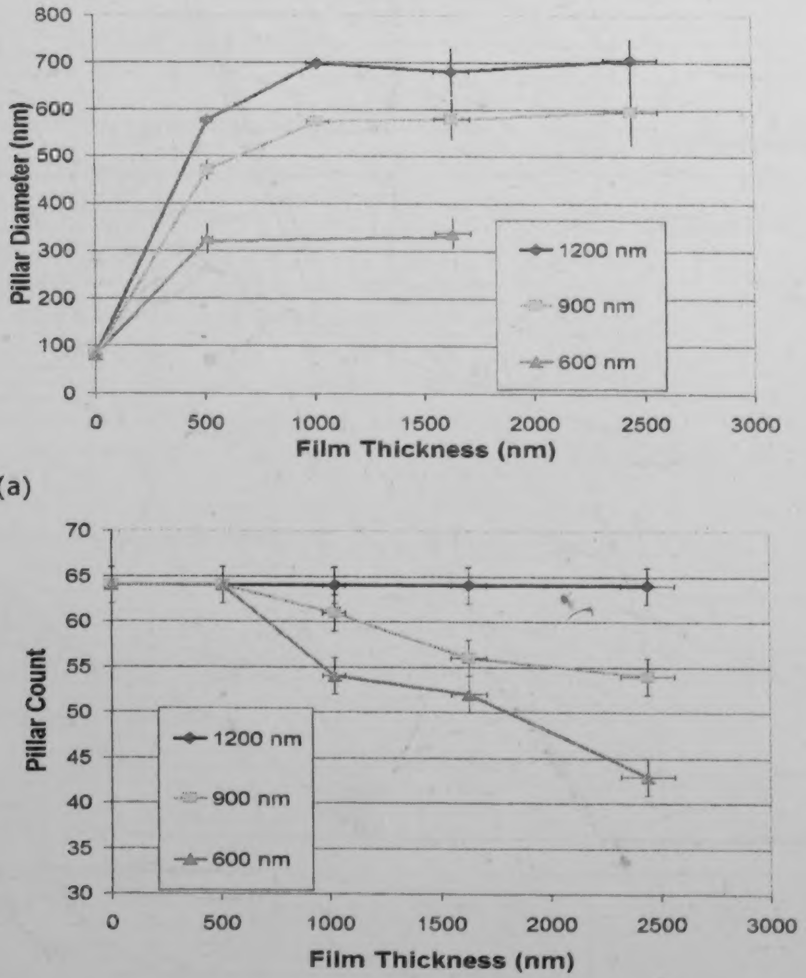

(a)

(b)

Figure 5.14. Increase of pillar diameter (a) and decrease in average pillar count density (b) for periodic tungsten films deposited by sputtering at $\alpha=86^{\circ}$. As with the SiO_2 films deposited by evaporation, columnar competition for films grown on seed arrays of less than 600 nm makes pillar diameter measurements increasingly inaccurate such that no data for film thicknesses greater than 2000 nm have been included in Figure 5.14(a).

Both the evaporated and sputtered films show a rapid increase in pillar diameter at the start of their evolution. This rate of increase fell off with film thickness, and in most cases the diameters were observed to reach a relatively stable value at a thickness that increases with the increasing period of the underlying seed array. This steady-state condition corresponds to a pillar diameter that is *relatively* constant (within its measurement error), but is thought to increase slightly as the pillar density continues to fall. Evaporated films (Figure 5.13) reach a steady pillar diameter between 1μm (600 nm seed period) and 2μm

(1200 nm seed period). The corresponding pillar count densities generally decrease with film thickness as the pillar diameters increase. This supports our assumption that the films try to attain a constant density throughout growth.

The rate of decrease in pillar count density is dependent on the seed period. For large seed periods (i.e. 1200 nm), this density is relatively constant, reflecting the fact that the pillar diameter does not reach a competitive stage over the film thickness shown. In other words, individual columns are not yet being overshadowed by their neighbours (i.e. the film period is less than the preferred period of aperiodic growth). This occurrence corresponds with a rapid increase in pillar diameter at large seed periods, and an increase of deposited flux between columns relative to films grown at smaller seed periods. Deposition of inter-columnar flux diminishes as the pillar diameter grows towards a point where space between columns is effectively shadowed, although for square lattices there will always be channels along which films can grow for brief periods during substrate rotation. At this point the columns begin to compete with one another, which is observed as a decrease in columnar density. The columnar density rapidly decreases for the evaporated films grown at 150nm, suggesting a highly competitive environment. This is not surprising as this seed separation is considerably less than the equilibrium separation, *s,* of similarly deposited aperiodic structures during their initial growth evolution (see Figure 5.1). Correspondingly, the column count for evaporated film growth at 1200nm is constant over the growth thickness tested, indicating that the onset of competition either has not begun or has not progressed far enough to be observed as a decrease in column density. It also suggests that the diameters of pillars grown at 1200nm (evaporated) will continue to increase, albeit it at a progressively slower rate. Despite the apparent equilibrium state of the results shown in Figure 5.13(a), it is thought that the trend is still towards an increasing pillar diameter.

For the sputtered films, both the column count and pillar diameters were limited to those films grown on seed arrays of 600nm and greater. This limitation was due to the large amount of column competition on seed arrays of 150 and 300nm separation, which made measurements of these values both difficult and inaccurate. However, over the limited seed period range tested, a similar behaviour between evaporated and sputtered films was observed. Sputtered films (Figure 5.14) reach stability at between 0.5µm (600nm) and 1µm (1200nm), with a corresponding count density that is rapidly decreasing for the 600nm film (indicating a highly evolved competitive environment) and a relatively constant count for the 1200nm (indicating that competition may only be in its initial stages). The onset of competitive behaviour occurs at a lower value than for the evaporated films, as described earlier.

Pillar diameters increase rapidly until the onset of competition, at which the increase is more gradual. It is likely that with increasing film thicknesses beyond 2500 nm, films grown on both the 900nm seed array and then the 1200 nm seed array will become less regular in their pillar diameters. This suggests that as film thickness increases, column count is expected to continue to fall as observed in aperiodic films. Periodic films, however, show a delay in competitive behaviour relative to an aperiodic film grown under similar conditions. This result is significant, as it may enable engineering of more precise structures in periodic films than aperiodic films. Continued optimization of the underlying seed structure may lead to a preferred shadowing condition at the start of deposition, further delaying the onset of the mechanism of columnar competition in films deposited by GLAD.

5.4 CONCLUSIONS

The following trends were observed in the fabricated films.

1. If seed period (*p*) for a periodic film is much greater than the equilibrium separation (*s*) of an aperiodic film deposited under similar conditions, the onset of column competition is delayed, with a corresponding decrease in the rate of decrease in pillar count density with thickness.
2. Alternatively, if this seed period is much less than the aperiodic film's equilibrium spacing the occurrence of column competition is advanced, with a corresponding increase in the rate of decrease in pillar count density with thickness.
3. At a given film thickness, the cross-over between increased competitive behaviour and increased pillar diameter appears to occur at $p=s$.

4. As the angular flux distribution width increases,
    a. The sensitivity of film growth (in regards to column competition and pillar count density) to seed period increases.
    b. Structural appearance becomes increasingly non-regular.
    c. Periodic helices are more prone to degenerate into pillars at high seed separations. Conversely, helical microstructures are more easily fabricated as the seed separation decreases.
    d. The transition region where helices degenerate into pillars adjusts to higher seed separations at increasing flux incidence angles.
    e. Competition effects such as the accumulation of the majority of flux in single columns increase with decreasing seed separations and increasing flux angular distribution and incidence angle.

It has been shown that although sputtering can form periodic quasi-helical microstructures, the quality of these structures is limited by the seed separation. Optimizing the deposition parameters (based primarily on flux incidence angle) for a particular material is required to ensure that the seed spacing can be minimized without causing the structure growth to coalesce with neighbouring structures.

As a final statement (one that deserves further study), it is noted that competition effects observed in pillar microstructures are significantly diminished in evaporated aperiodic and periodic helices. Possibly, this observation is due to the self-correcting nature of helical growth, and its ability to adjust its pitch arm diameter to counter additional competitive pressures during growth.

Chapter 6 – Study on the Magnetic Properties of GLAD films

6.1 INTRODUCTION

In addition to growth mechanics, researchers at the University of Alberta and elsewhere have investigated film properties related to potential GLAD applications/devices. A selected number of these properties, encompassing both periodic and aperiodic GLAD microstructure arrays, are summarized in Table 6.1.

Table 6.1. Investigations/Applications of selected GLAD film properties

Film Property	Investigations/Potential Applications	References
Optical	LCD displays, birefringent media, three dimensional photonic crystals, rugate filters, and diffraction gratings	[11, 127-132]
Mechanical	Microactuators	[17]
Thermal	Thermal barrier coatings	[16]
Electrical properties	Humidity and chemical sensors, supercapacitors, field emission displays	[14, 17, 18, 104, 133]
Catalysis	Microcalorimetric hydrocarbon sensors, photocatalysis	[15, 75, 134]
Biomedic	Microfluidics, lab-on-a-chip	[135, 136]

One area of interest that has not been adequately researched is that of the magnetic properties of GLAD films, though a few exceptions do exist including a group at the Center for Materials for Information Technology (MINT) research facility at the University of Alabama, which briefly examined the effect of film morphology on the hysteresis curves of iron [9] at the relatively conservative deposition angle of 75°, and of cobalt [10] at 75° and 83°. The lack of significant research efforts in this field is unfortunate as the facility to fabricate structures with controlled geometry offered by the advanced GLAD technique may yield unique insight into micro-magnetics, an area that is generally poorly understood [62]. For example, the ability to control the size, shape, orientation, and composition of the magnetic structure on a nanometer (or sub-domain) scale offers a greater range in magnetic properties that can be controlled. This level of control can be applied not only to magnetic recording media (i.e. to increase storage densities) [62, 137, 138], but also leads to the ability to test micromagnetic theories/modeling and the fabrication of more innovative magnetic materials and devices.

This section reports a preliminary study of the utility of the GLAD process in fabricating magnetic microstructures for such applications as micromagnetic modeling and high-density magnetic recording media.

6.2 THEORY AND PRINCIPLES

Before jumping into a description of the depositions undertaken to study magnetic phenomena in GLAD films, some theory is required.

The following vectors are defined [138, 139]:

Magnetization (**M**)	The total vector sum of magnetic dipole moments per unit volume
Magnetizing Field (**H**)	The applied magnetizing field

Many of the basic characterization properties of a magnetic material may be obtained via an analysis of its hysteresis loop, which is simply a plot of one of the above quantities against another (see Figure 6.1). The area enclosed by the magnetic hysteresis loop describes the energy taken from the driving magnetic field and converted to heat during each loop cycle [138]. If a sufficiently high magnetic field is applied, memory of previous, "minor" loops is removed, and further properties of the media can be obtained from the "major" loop.

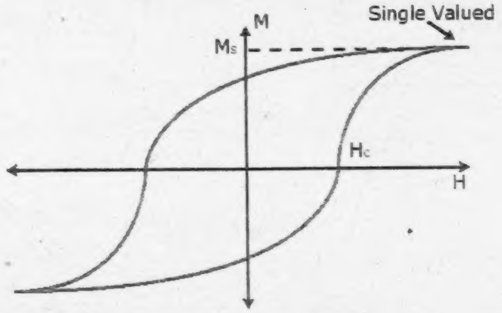

Figure 6.1. The "major" hysteresis loop describing the relationship between magnetization (M) and magnetizing field (H).

A few other notable medium properties can be defined:

Easy axis	The energetically favourable axis i.e. the magnetization will more easily align to this axis
Hard axis	The magnetization direction that is weakly favourable (very easy to adjust with external fields)
Magnetocrystalline anisotropy	A material property describing the tendency of the magnetization vector to align along a film structure crystal axes. A material having this property is cobalt.
Shape anisotropy	A structure property describing the tendency of the magnetization vector to align along one of the geometric axes of the thin film structure. Columns have this property.

6.3 FILM CHARACTERIZATION[†]

6.3.1 GLAD Fabrication Parameters

Thin films consisting of posts, helices, and chevron structures were fabricated at varying deposition angles using electron beam evaporation, and nickel (purity = 99.995%) or cobalt (99.95%) as the source material. The deposition conditions for these films are shown in Table 6.2. The base pressure and deposition pressure during each run was 2.5×10^{-4} Pa (1.8×10^{-6} torr) and $<5.3\times10^{-4}$ Pa (4.0×10^{-6} torr) respectively.

Table 6.2. Film Deposition parameters for study on magnetic properties

Source Material	α	**Deposition Rate**	**Microstructure**
Cobalt	84°	15Å/sec	Post
Nickel	86°	2Å/sec	Helix
Nickel	80°	2Å/sec	Post
Cobalt	84°	15Å/sec	Chevron

[†] This section has been partially excerpted from the article: B.Dick, M.J. Brett, T.J. Smy, M.R. Freeman, M. Malac, R.F. Egerton, "Periodic magnetic microstructures by Glancing Angle Deposition", J. Vac. Sci. Technol. A. **18**, 1838 (2000), and is used with the permission of the American Vacuum Society (2003).

To add further control to magnetic field alignment and properties, these films were deposited on silicon wafers coated with a 70nm layer of SiO_2 and a subsequent 100nm layer of chromium. The SiO_2 layer simply serves to buffer the chromium layer from the underlying silicon substrate. Here, the chromium layer is referred to in the literature as a magnetic underlayer, and has been found to promote the coercivity of subsequently deposited pure cobalt. It has been speculated that the Cr underlayer, whose grain size increases with thickness and deposition temperature, controlled the grain size of the Co layer by means of a lattice-matching epitaxial growth process [140, 141]. No underlayer was used to promote crystalline structure or the magnetic properties of the nickel films deposited and analyzed in this chapter.

6.3.2. *Film Morphology*

In addition to the method identified in §5.1.2, an alternative means to calculate the average period of randomly seeded posts can be identified. Here, an analysis of the surface topography obtained using the Dimension 3100 Atomic Force Microscope in the University of Alberta NanoFab is undertaken. Taking a one-dimensional (1D) Fourier Transform (FT) of a line profile drawn across the surface topography yields the frequency (i.e. the spacing) of surface structures. Using the line profile and topographic image as a guide, an estimate of the frequency corresponding to the average structure spacing can be obtained. The film thickness can be determined by scanning electron microscopy (SEM).

Although the posts are randomly positioned on the small scale (assuming an absolutely smooth substrate surface), over a larger film area the 1D FT shows an average period dependent on material and angle of incidence (among other factors). This average period was obtained with a degree of subjectivity, and so the results obtained can only be taken as a relative measure. Pillars that have only recently stopped contributing to the overall film growth (due to being out-competed by their neighbours) are still represented on the overall frequency spectrum as a significant peak. Hence, it was necessary to choose a frequency component that best fit the observed AFM profile in terms of columns still contributing to film growth. A two-dimensional FFT, although more appropriate for calculating average periods across the surface, magnified the difficulties in ascertaining this appropriate frequency and hence was not used in the analysis of column separation shown in this section.

Using the 1D FFT method, the average period of the cobalt posts was calculated to be 200nm with an 800nm film thickness, while the nickel posts were measured at 225nm and 500nm for the average period and film thickness respectively. Variation in film thickness was determined using AFM scans taken at random sampling intervals over the substrate. This variation was found to be 5 and 9% of the total film thickness across a 10cm^2 area for cobalt and nickel respectively.

As previously described in §4.2, the film porosity for each microstructure type is highly dependent on the deposition angle, and this is illustrated by the low porosity of the nickel helices shown in Figure 6.3(b) (α=80°) compared with the higher porosity in the other films (α>84°).

6.3.3. *Magnetic Properties*

The normalized hysteresis loops for these films are shown in Figure 6.3, and were obtained using a Quantum Design 9T PPMS DC magnetometer/AC susceptometer. Coercivities in the perpendicular and parallel field direction were subsequently derived for each film and are shown in Table 5.3. As the volume of each sample was not consistent a comparable measurement of magnetic saturation (M_S) could not be calculated. The magnetic anisotropy in the randomly seeded nickel posts is apparent; with the measured perpendicular coercive field approximately twice that of the parallel field, although both fields are relatively weak. Normally, one would expect the magnetization field in the pillars to align more easily along the axis due to the shape anisotropy. The observed alignment of the easy axis parallel to the substrate may be due to the close packing of the nickel pillars that contribute a strong demagnetizing effect perpendicular to the plane of the film. From the hysteresis curves, the magnetic susceptibility shown by the nickel posts and helices has a similar anisotropy between parallel and perpendicular directions.

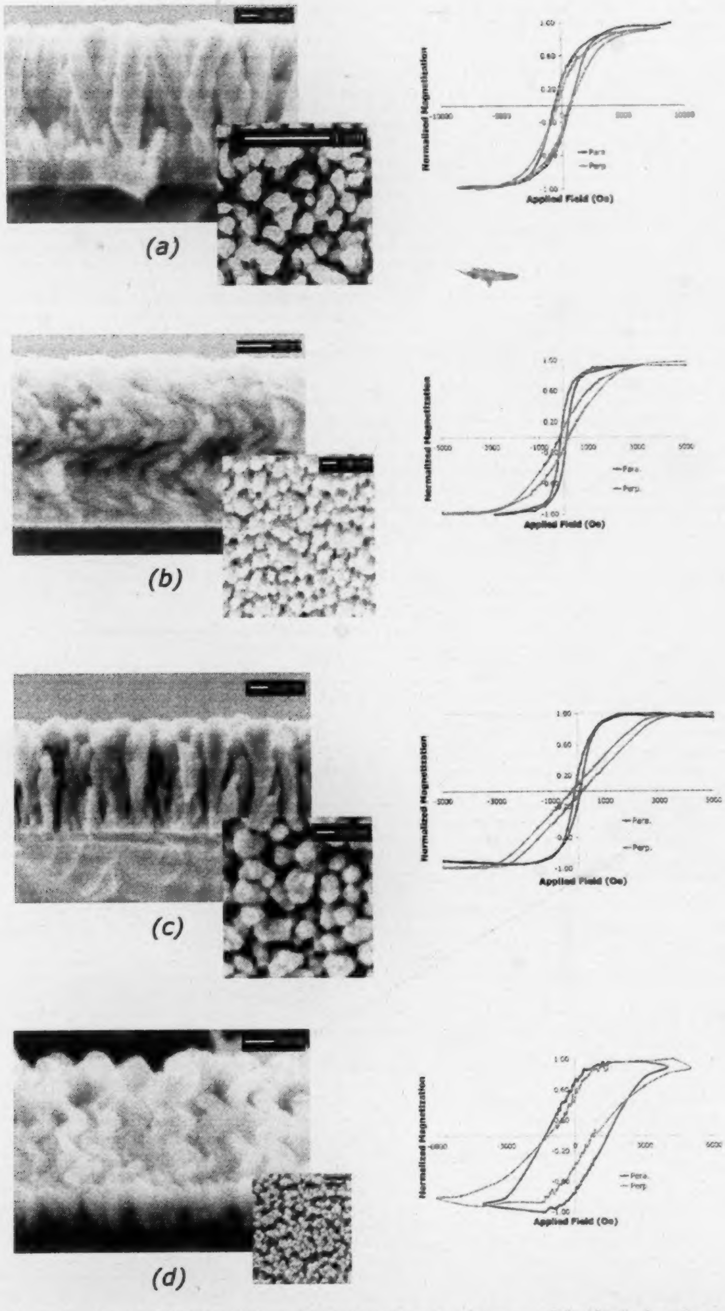

(a)

(b)

(c)

(d)

Figure 6.3. Randomly seeded GLAD microstructures shown with their hysteresis curves measured at room temperature. Both the hysteresis perpendicular (perp.) and parallel (para.) to the substrate field is shown for each microstructure under an applied field: (a) cobalt posts deposited at α=84°; (b) nickel helices (α=80°); (b) nickel posts (α=86°); (d) cobalt chevrons (α=85°). The dense thin film immediately shown as a first layer in Figure 6.3(a,d) is the chromium underlayer. Note that the SEM depth of field obscures the porosity of a sample in the side view.

Table 6.3. Measurements of magnetic saturation and coercivity for different source materials and microstructures

Figure/Sample #	Measurement	Coercivity (Oe)
Figure 6.3(a) Co posts	Parallel Perpendicular	692±19 484±14
Figure 6.3(b) Ni helices	Parallel Perpendicular	111±10 177±6
Figure 6.3(c) Ni posts	Parallel Perpendicular	90±10 185±10
Figure 6.3(d) Co chevrons	Parallel Perpendicular	1410±45 720±22

Because of the strong magnetocrystalline anisotropy for cobalt, both transmission electron microscopy (TEM) and x-ray diffraction (XRD) analyses were used to determine the crystalline orientation within the cobalt post microstructure. The equipment used was a Rigaku Geigerflex Power Diffractometer and a Hitachi H-800 200kV scanning TEM with a tungsten thermionic filament. The XRD analysis is shown in Figure 6.4(a), while the electron diffraction (ED) image of single cobalt posts is shown as both a micrograph and diffraction pattern in Figure 6.4(b). The ED and XRD spectra are consistent with the cobalt posts having a largely monocrystalline, hexagonal close-packed (hcp) structure orientated along the <002> axis. This result agrees with earlier reports of cobalt and cobalt alloy films grown on a chromium underlayer [142].

The randomly seeded cobalt posts exhibit some perpendicular anisotropy with a high coercive field found in the plane of the film. The films are less anisotropic than expected, perhaps due to coupling between pillars in the low porosity film. Demagnetization effects perpendicular to the plane of the substrate may cause this coupling, though it is more likely the coupling is due to the small amount of film growth (<75nm) observed between pillars. It is hypothesized that growing pillars on periodic lattices may minimize both the inter-pillar film growth and potential dipole coupling by allowing adjustments to both pillar diameter and separation. It has also been suggested that this underlying "forest" of film growth at the base of the pillars could be absorbed into the microstructures if an annealing cycle was performed [143], and although this process may have the additional advantage of increasing the crystallinity of the film, it could also degrade the film microstructure and increase its oxygen content. Hence, this cycle was not performed as it was expected to diminish the magnetic properties of the film.

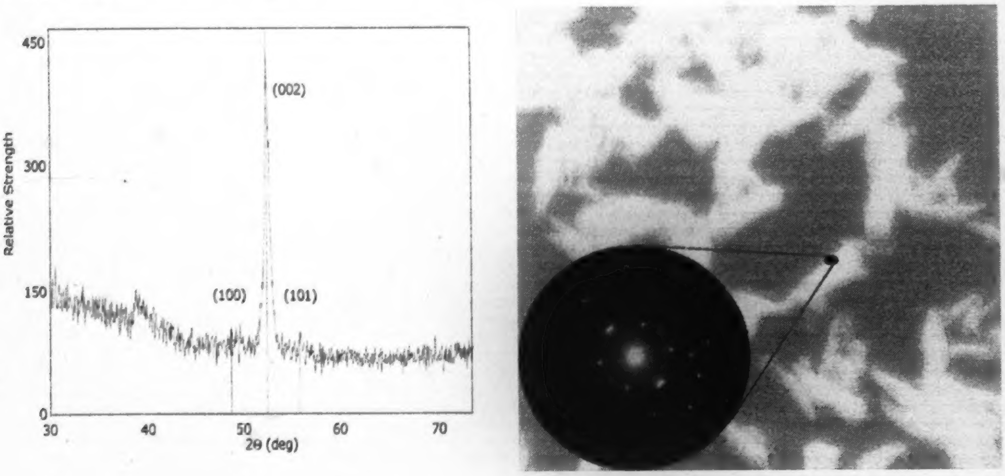

(a) (b)

Figure 6.4. Crystal analysis of the randomly seeded cobalt posts. (a) XRD analysis of the microstructure, and (b) TEM diffraction pattern and sample image.

6.4 CONCLUSIONS

Originally, it was thought that GLAD pillars arranged in a periodic lattice (as described in §2.3.2.5) might serve as a suitable material for high-density storage media. Perpendicular storage media (i.e. where the magnetization vector is aligned normal to the substrate surface) is one of the suggestions for alleviating some of the difficulties which occur with increasing storage densities, including the signal to noise ratio, transition noise at bit boundaries [137], tracking difficulties, and read/write limitations [62]. Indeed, this was the primary motivation for exploring magnetic characterization of these films. Periodic structures exhibiting the equivalent of approximately 3 Gigabits / in^2 (assuming each particle consisted of a single bit) were grown [8], and subsequent research by Malac *et al.* using a TEM to etch a small sample indicated that nickel films might be grown with periods of less than 10nm [106]. However, magnetic force microscopy (MFM) imaging of the domain structure for these and previous films was inconclusive, and subsequent developments in this field (namely, demonstrated storage density of over 25.7 Gigabits/in^2 in a commercial device by IBM using anti-ferromagnetically coupled media coating [144], and research on the so-called Millipede project which uses arrays of resistively heated AFM tips pressing into a polymer substrate to potentially obtain storage densities of 1 Terabit/in^2 [145]) rapidly outpaced potential GLAD development.

Chapter 7 – List of Recommendations and Conclusion

7.1 LIST OF RECOMMENDATIONS

> *The degree to which we understand the growth of GLAD structures, is easily overshadowed by our ignorance: the more we learn, the more we realize how much we do not understand.*

The purpose of this thesis was to expand the parameter space within which GLAD film growth was understood, and provide a framework for future investigations. Hence, much study is still required to fully characterize the growth mechanisms and properties for thin films deposited at glancing incidence. During the course these investigations, a number of areas arose that require further examination. This section describes a few of these possibilities:

7.1.1 Fundamental Studies

7.1.1.1 Rotation

As documented in this thesis, substrate rotation is a key growth parameter for GLAD films. If the substrate is rotated quickly, pillars are grown; rotate the substrate less quickly and eventually a helical structure is formed; don't rotate the substrate at all, and the well-documented oblique columns arise. In §4.3, however, the "simplicity" of this growth mechanism was brought into question. Films grown do not necessarily exhibit this expected morphological trend, especially in circumstances where geometry (i.e. shadowing) is not the primary growth mechanism.

An in-depth investigation of material dependency on GLAD morphology (particularly at extremely high substrate rotations) is justified. For example, in §4.3.4.2 the film's crystal structure was suggested as a superseding growth mechanism to adatom shadowing for GLAD films. To confirm this suggestion, a number of experiments may be undertaken:

a) Selective area TEM and XRD: to determine if there is a difference in crystal structure and orientation between the 'flat top' and 'peaked top' aluminum films. A measured difference may indicate that one of these structures is in a thermodynamically stable state while the other is in a kinetic state.

b) Assuming that the 'peaked top' structure is found to be the kinetically formed structure, a vacuum furnace can be used to anneal the film so that it reverts (at least partially) to its thermodynamic state.

c) The crystal structure of the bismuth films must be measured to determine whether they are amorphous (as my argument suggested) or crystalline.

d) Growth of alternative materials with a similar crystal structure to aluminum, which are known to grow epitaxially on Si (100). With respect to substrate rotation, is a similar growth morphology to aluminum observed?

e) Growth of an aluminum film (using the same conditions described in §4.3) on a Si(111) substrate. Does the underlying substrate orientation effect the resulting Al film morphology?

Final Word on Substrate Rotation

The work presented in this thesis has utilized revolutions per minute (RPM) as the primary parameter describing structure transition observed in GLAD films. In the present circumstance, this use is accurate as the majority of films were grown at the same deposition rate. Generally, however, it is more appropriate to report the structure transition in terms of a function, γ, describing the thickness of film grown per substrate revolution (i.e. pitch length). In such a methodology, the transition between pillars and helices would be expected to occur at the point where this function is approximately equal to the coil diameter of the helix (i.e. the pitch is sufficiently small as to render the structure indistinguishable from that of a post). For example, from Table 4.7(a), the average deposition rate for SiO_2 was measured to be approximately 2.9 Å/sec. The structure grown at $d\varphi/dt = 0.479$ RPM appears to occur at or near the transition between helical and pillar like growth. At this substrate rotational speed, $\gamma = 36$ nm/rev which is on the order of the observed coil diameter in this film within each helical turn. Hence, ignoring the effects of increased substrate heating and adatom burial rate, increasing the deposition rate requires a decrease in $d\varphi/dt$ to maintain the same structure.

It is suggested that future investigations on the growth GLAD structures should utilize γ to help estimate where structure transitions may occur. Among other factors, γ is dependent on both α and source material. Therefore, a useful project may be to map out this factor for a variety of materials and flux incidence angles to be later used in describing and optimizing GLAD film growth.

7.1.1.2 Density and Growth

In Chapter 5, it was shown that the s/δ (or p/δ) factor might be used to optimize film growth in periodic GLAD microstructures. Additional (and more accurate) measurements of pillar diameter, average separation, and density for aperiodic films are required to better map the parameter space of this factor in relation (primarily) of flux incidence angle and source material.

7.1.1.3 Evolution of Helical and Oblique structures

The research presented in this thesis on the growth behaviour of GLAD thin films has primarily concentrated on the pillar microstructure due to its ease of measurement. This structure, however, represents just one of the numerous geometries that can be fabricated using the GLAD technique. Although it is generally believed that the density of these films should not be dependent on their morphology, this does not require that they will enjoy the same growth evolution. Periodic GLAD helices, for example, seem to exhibit a larger tolerance to changes in their underlying seed period at low $\Delta\alpha$. As the angular flux distribution is increased, however, their growth can easily degenerate into a pillar (see §5.3.2). As a further example, oblique columns exhibit a degree of 'fanning-out' during their evolution (as illustrated in Chapter 1) that is not significantly present in either helical or pillar microstructures. These and other film morphologies require an in-depth study to examine their particular growth characteristics so that their structures may be controlled for use in future applications.

7.1.2 Alternative seed lattice materials and fabrication processes

Chapter 3 lists a number of techniques that can be used to fabricate seed arrays for growing periodic GLAD structures. Of these, only two were examined; namely, electron beam lithography and plastic embossing.

During the course of this research, however, opportunities arose to examine a few of the alternate processes. For example, with limited success films were deposited on both microsphere arrays and arrays etched by focussed ion beam (FIB). The FIB arrays were patterned by Rob Patterson at Fibics Inc in Ottawa. The possibility of utilizing laser interference lithography as a pattern generator, and poly(dimenthylsiloxane) (PDMS) as a medium in which a pattern may be created were also briefly explored. These last two items, described briefly in following paragraphs, require further research to determine their feasibility as processing tools to quickly and effectively fabricate seeding arrays over large areas as required for most applications envisioned for periodic GLAD structures.

7.1.2.1 Poly(dimenthylsiloxane) mediums

Poly(dimenthylsiloxane) is widely used in various industries. In microfabrication, for example, it can be used as a positioning agent for microspheres [146]. The benefit of PDMS arises from its ease of application; a 1:10 mixture of the curing agent to plastic is applied to a mould and then allowed to set. Unlike embossing, no external pressure is typically required, and the hardness of the plastic film formed is based on amount of cure in the mixture (i.e. increase the ratio of curing agent to plastic and the resulting film is harder). Using PDMS, a number of small projects have been conducted:

1. Fabrication of a two-dimensional interference grating using substrate patterned with 1μm diameter vias in photoresist as a mould. When peeled from the substrate, SEM imaging showed that the resulting PDMS film contained arrays of 1μm diameter half-spheres with approximately a 2.5μm period. A laser beam shone through the film also confirmed this lattice period.

2. Attempt to flow the PDMS mixture into a GLAD film by constraining the plastic-curing agent mixture over a GLAD film using a hollow aluminium tube (approximately 1 cm diameter, 2 cm height). Unfortunately, this attempt was not successful as some materials (e.g. cobalt) tended to adhere more strongly to the PDMS than the substrate, and were removed from the substrate when the film was peeled away. Other materials (e.g.

nickel) repelled the PDMS and so didn't allow it flow between its microstructures at all. This investigation would be interesting to explore further. If PDMS can be made to flow between the GLAD structures, it provides an addition means to contain GLAD structures within a rigid medium.

3. Seeding lattices consisting of 500nm dots separated by 1μm were fabricated by placing a small amount of the plastic-curing agent mixture over the mould. The PDMS film was then simply peeled away from the mould after setting overnight. An example of one of these films is shown in Figure 7.1. To fabricate the moulds, photolithography was used to create vias in photoresist spun on a layer of nickel. A nickel etch was then applied to form the vias in the underlying film layer, after which the photoresist was removed by acetone.

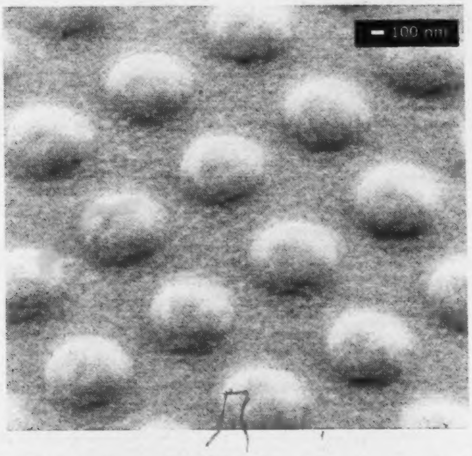

Figure 7.1. Seed layer produced by PDMS using vias in photoresist as a mould.

4. Based on the success in forming 500 nm diameter seeding elements, Miro Belov fabricated the inverse of the structure shown in Figure 3.2 using electron beam lithography. A small amount of the plastic-curing agent mixture was placed over the mould and allowed to set overnight. The PDMS was then peeled from mould and imaged using an SEM (see Figure 7.2). The pattern has partially replicated itself in the PDMS consisting of seeds with features sizes less than 100 nm, although the background structures were large. These small bumps can be observed overtop of the larger morphology features in Figure 7.2(c). As there was insufficient time to pursue this project further, it is not certain if this was just a bad

batch of PDMS or a property inherent in the processing. For example, is an applied pressure required to flatten the background features? If these features can be removed, the fabrication of 100 nm seeding structures opens the possibility of a quick means for stamping large arrays of small-scale structures from one or two initial moulds. Currently, the time required to fabricated large arrays (>cm^2) using conventional EBL is prohibitive.

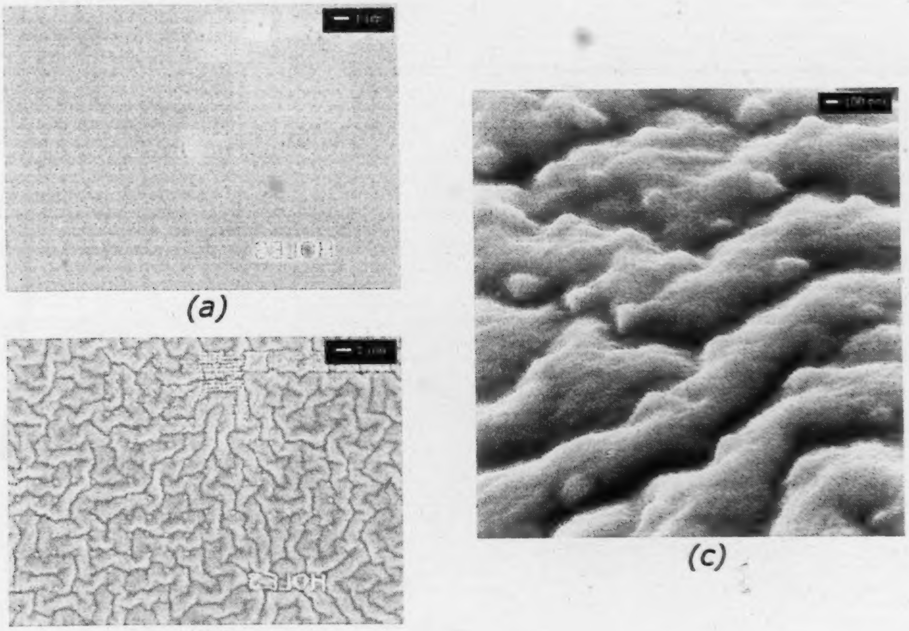

(a)

(b)

(c)

Figure 7.2. EBL-produced mould for production of seed layers in PDMS: a) Mould produced in PMMA by electron beam lithography, (b) PDMS seed layer, and (c) a blow-up of the individual PDMS seed elements.

7.1.2.2 Laser (Optical) Interference Lithography (LIL)

The use of laser (or optical) interference lithography (LIL) [84] – also referred to as holographic lithography – appears to have been growing in popularity over the last decade. A number of papers have been published utilizing this technique in a variety of areas including the fabrication of periodic magnetic structures [65, 93, 147] and field emitter arrays [148, 149]. This technique has been shown to accurately create structures with pattern densities exceeding 10^9 dots/cm^2 [148] over a 2-inch diameter region.

Optical interference lithography creates a pattern on the substrate during the photoresist development stage. The basic process is illustrated in Figure 7.3.

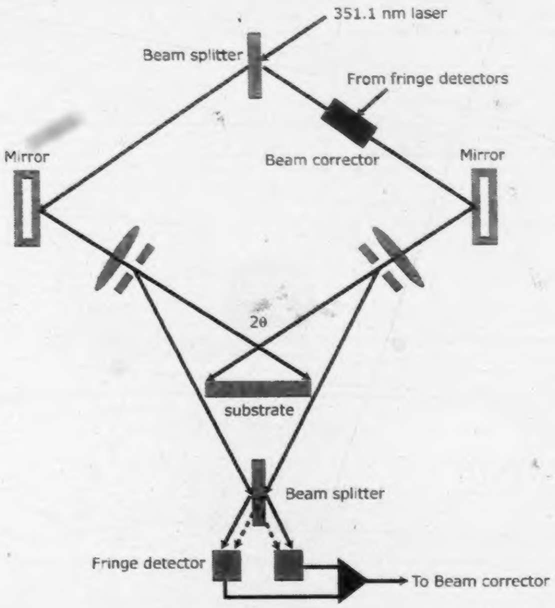
351.1 nm laser
Beam splitter
From fringe detectors
Mirror
Beam corrector
Mirror
2θ
substrate
Beam splitter
Fringe detector
To Beam corrector

Figure 7.3. Laser Interference Lithography (LIL) set-up. Adapted from Ref. [150].

LIL consists of a single laser split into two paths, which recombine at the substrate surface. The interference pattern formed at the surface selectively exposes the photoresist layer on the substrate - maximum exposure where the beams reinforce, and minimum exposure where the beams cancel. This effect creates a sinusoidal exposure pattern within the photoresist layer, which can be used for later etching processes. The periodic of the interference is given by [148]:

$$p = \frac{\lambda}{2\sin(\theta)} \qquad [7.1]$$

Where λ is the laser wavelength, and 2θ is the angle between the interfering beams. It is difficult to expose gratings and lattices of 100 nm period due to the difficulty in obtaining laser sources with the temporal and spatial coherence and output power sufficient for conventional LIL at much smaller wavelengths than $\lambda = 257$ nm [83]. However, achromatic interference lithography, an LIL technique utilizing gratings to remove the dependent of the pattern period on the incidence wavelength, has accurately created patterns with a 100 nm structure period [82, 83, 148, 150].

One of the perceived limitations of this technique is its inability to fabricate different seed periods within a given array (in contrast to EBL, for example). However, for many application purposes, a single period array is required. In addition, the fabrication time for LIL arrays is limited to the photoresist processing, as the laser exposure time is minimal. Hence, LIL fabricated structures would have a much higher throughput than EBL.

7.2 CONCLUSION

This thesis has presented both experimental and simulation work characterizing the fundamental growth mechanisms and properties for films produced using the GLAD technique.

A background to the GLAD technique was provided in Chapter 2, and included references to the 3D-FILMS ballistic deposition simulator and developments on growing GLAD microstructures in a periodic lattice using a pre-defined seed layer. The techniques for producing these seeding structures were studied in Chapter 3 and included two processes: Electron-beam lithography (EBL) and plastic embossing. EBL was used to fabricate seed arrays of 80 nm (in PMMA) or 175 nm (in epoxy novolak SU-8) diameter dots with lattice periods of 150 nm through 1.2μm, and was found to be an ideal research tool for determining the effect of seed topography on the subsequently grown GLAD structures. Plastic embossing provided a potential means to quickly and easily produce seeding structures over a large area for the growth of a periodic GLAD films. In this thesis, a 'proof-of-concept' study was completed, whereby multiple arrays of seeding elements with diameters down to 75 nm were stamped from a master pattern into epoxy. Periodic GLAD pillars and oblique columns were subsequently grown.

Chapter 4 describes the investigations on two key parameters for GLAD film growth: flux incidence angle and substrate rotational speed. In both studies, specialized deposition apparatus were constructed to allow for the simultaneous growth of several films at either different substrate angles (a range of 10 degrees in α) or multiple rotational speeds (a range of two orders of magnitude in $d\varphi/dt$).

In the first section of this chapter the morphological evolution of SiO_2 GLAD films deposited at $\alpha=83°$ through $\alpha=89°$ was qualitatively investigated. At $\alpha=83°$, a fine helical structure was apparent in the relatively dense GLAD, while the film deposited at $\alpha=89°$ showed the effects of a highly competitive growth environment. Small advantages in film topography are believed to allow for only a few structures to obtain the majority of the flux, thus obscuring the finer structure of the film. Hence, this work suggests that GLAD microstructures are more readily formed when $\alpha < 87°$, and best optimized when $\alpha < 85°$. A simple expression for film density within the GLAD regime was formulated and found to compare well with experimental results.

The second section of Chapter 4 described research on substrate rotation speed. Films of Al, Bi, Si, and SiO_2 were deposited at $d\varphi/dt$ = 0.0043 RPM through $d\varphi/dt$ = 42 RPM. Amorphous (SiO_2) and high temperature materials (Si) were shown to follow the standard GLAD morphological trend: low substrate rotational speeds ($d\varphi/dt$ < 0.1 RPM) yield oblique columns or helices, while high speeds ($d\varphi/dt$ > 1RPM) yield posts. Crystalline (Al) and low-temperature materials (Bi) were found to have morphologies which include structures outside of the standard model. For example, aluminum films exhibited posts with flat tops at rotational speeds around 1 RPM, and peaked tops for rotational speeds of over 40 RPM. These growth characteristics were reproduced in the 3D-FILMS simulator, and suggest that adatom diffusion length decreases with increased substrate rotation speed. Additionally, the preferred crystal plane is thought to reorient for values of $d\varphi/dt$ which create a non-equilibrium shadowing condition at the substrate surface. This latter observation suggests that GLAD films grown at rotational speeds within the transitional region between helical and post formation will yield poorly formed structures.

Incremental growth studies of both sputtered and evaporated periodic GLAD films was undertaken in Chapter 5 to determine how changing seed period, angular flux distribution width, and flux incidence angle affected the resulting GLAD microstructure. 3D-FILMS simulations complemented this study. The central finding of work was the confirmation of the s/δ (or s/p in periodic films) factor as a governing parameter for controlled growth. Columnar competition was observed to increase when the seed period (p) was much less than the equilibrium separation (s) of an aperiodic film deposited under similar conditions, while these affects were lessened when $p >> s$. Under conditions of increased angular flux distribution width ($\Delta\alpha$), the sensitivity of film growth to seed period increased. Specifically, helices were found to degenerate more readily to pillars at higher seed separations as $\Delta\alpha$ increased. Again, the aperiodic structure separation, s, appeared to governing the position of the transitional region between pillar and helical growth.

Chapter 6 summarized research conducted characterizing the magnetic properties of GLAD films. Hysteresis measurements for several GLAD microstructures types (including structures) were briefly studied. It was found that GLAD structures may be of possible use in micro-magnetic studies and simulations.

7.3 FINAL WORD

This research contained within this thesis has expanded the parameter space within which GLAD film growth is understood, and articulated future directions of study (see §7.1), which can be undertaken to take this work further. The reader may use this work to help build investigative roadmaps for optimizing GLAD film structures for a particular application.

Appendix A – Glossary

3D-FILMS	A three-dimensional (3D), Monte-Carlo ballistic simulator, based on the SIMBAD program, which models the creation and dynamic evolution of 3D microstructures in PVD thin films.
Adatoms	Incident atoms which have transferred their kinetic energy to the substrate lattice and become loosely bound to the surface.
Aperiodic GLAD films	Term used in this thesis to describe GLAD films grown on flat substrates.
BD	Ballistic Deposition – Modeling which treats flux as arriving co-linearly at the substrate surface. Adatom diffusion and surface shadowing are the primary growth mechanisms.
Bulk diffusion	Movement of atoms within the film. This process is characteristic of Zone III films as described by the Movchan and Demchishin structure zone model.
Chirality	Material property describing its non-symmetric geometry. A chiral object cannot be superimposed by rotation and translation onto its mirror image.
Collimated sputtering	The process by which sputtered atoms outside a desirable incidence angle range are mechanically inhibited from striking the substrate. A honeycomb sheet-metal array is placed perpendicular and between the target and substrate plane. Although $\Delta\alpha$ is minimized, the deposition rate at the substrate surface is significantly reduced.
Column competition	The process by which thin film columns extinguish their neighbours due to shadowing at extremely oblique flux incidence angles. The resulting decrease in column number density is compensated by an increase in individual column diameters, leaving the overall film density constant.

Columnar growth	The tendency of PVD thin films to grow columnar microstructures. These columns are oriented in the direction of the flux source.
CVD	Chemical Vapour Deposition – A volatile material compound reacts chemically with other gases to produce a non-volatile solid that deposits onto a substrate as a film.
EBL	Electron Beam Lithography - Technique for creating extremely high resolution patterns. EBL consists of scanning an electron beam across a resist sensitive to electron irradiation, while controlling the beam to create any desired two-dimensional pattern. The technology is capable of creating an infinite number of patterns in a variety of materials at sub-50 nm resolution. However, although very versatile, EBL is more expensive and considerably slower than photolithography.
Evaporation	The controlled transfer of gaseous atoms from a heated source to a substrate where film forms.
Porosity	A solidity measurement for a thin film. This parameter is inversely proportional to the density of the thin film compared to its bulk counterpart, and is sometimes used as an expression of surface area. Film porosity tends to increase with increasing flux incidence angle, and, most significantly, within the glancing incidence regime ($\alpha>80^{o}$).
GLAD	Glancing Angle Deposition – The use of substrate rotation and flux incidence angle variations to fabricate a range of thin films morphologies with controlled structure and porosity. This technique requires columnar vapour flux to be deposited at extremely oblique incidence angles ($\alpha>80^{o}$).
Incident flux	Term used to describe source vapour arriving at the substrate. Usually implies a directional component.
LPLT sputtering	Low-pressure, long-throw sputtering – Technique by which the sputtering target and substrate are separated

	by a relatively large distance (typically greater than 15 cms), and the plasma is ignited under low chamber pressures (p_c < 1mTorr (0.1 Pa)). This process attempts to minimize $\Delta\alpha$ by increasing the mean-free path of particles in the chamber. Flux arrives at the substrate with a linear trajectory, though not necessarily with an origin at the source due to collisions with the working gas atoms.
Movchan and Demchishin SZM	One of the first structure zone models to classify continuous film structure according to substrate temperature during deposition. Three 'zones' of film texture are identified: Zone 1, where atomic shadowing effects predominate ($T/T_m < 0.3$); Zone 2, where surface diffusion effects predominate ($0.3<T/T_m<0.5$); and, Zone 3, where bulk diffusion effects predominate ($T/T_m>0.5$).
Motohiro-Taga interface	The transition region occurring when the column angle is abruptly altered through a change of flux incidence angle. The resulting microstructure is similar in form to a chevron, with the apex being the Motohiro-Taga interface.
Normal incidence	A condition for deposition where the substrate is held perpendicular to the incident flux. This substrate configuration typically maximizes the film deposition rate while minimizing surface shadowing effects.
Oblique deposition	A condition for deposition where the substrate is inclined relative to the incident flux. Columnar growth is inclined towards the flux source.
Plastic embossing	The reproduction of nano- and microrelief structures by compressing polymers in a mould. This mould serves as a master template and is the inverse of the end topography desired. This technique is extensively used in the large-scale production of compact discs and holograms, and can be used to fabricate microstructures on the order of 20nm over areas as large as 16cm^2.
PVD	Physical Vapour Deposition – term used to encompass both evaporation and sputtering. Deposition occurs by

	the physical removal of atoms or molecules at the source, and their subsequent deposition on a substrate surface some distance away.
Sputtering	The ejection of atoms from a source surface through the impact of gaseous ions.
SEM	Scanning Electron Microscopy
SIMBAD	A film growth simulator utilizing two dimensional (2D) discs launched ballistically at the substrate surface to simulate film growth. The discs are incorporated at a point in the film which minimizes the local chemical potential, and is within one diffusion length of the impact site. Each disc represents the average behaviour of thousands of atoms, and approximately 50 000 discs are used in a simulation of a 4μm wide region. Advanced features of the SIMBAD simulator include 3D simulation, ion bombardment, bulk diffusion, CVD, flux transport from a sputter target, multilayer coatings, nucleation and grain growth kinetics.
SPM	Scanning Probe Microscopy
STF	Sculptured Thin Films - Manipulation of the columnar growth direction during film deposition through active rotation of the substrate. Although the deposition apparatus is similar to that of the GLAD process, STFs are usually (though not exclusively) grown at less oblique flux incidence angles, resulting in denser films.
Sputter yield	Measured in sputtered atoms per incident ion. This rate is dependent on a number of factors including the ionized gas species, the source material, the ionization energy, and the angle of incidence. In most circumstances, sputter yields are approximately 0.5 to 3 atoms/incident ion, with 2 atoms/incident ion being a typical value.
Surface diffusion	Movement of adatoms on the substrate or film surface. This process is characteristic of Zone II films as described by the Movchan and Demchishin structure zone models.
Surface shadowing	Phenomenon arising from the geometric constraint

	imposed by the roughness of the substrate surface or growing film, and the line-of-sight impingement of arriving atoms. This process is characteristic of Zone I films as described by the classic structure zone models.
SZM	Structure Zone Model – A model that is used to classify continuous and porous film structure according to a limited number of deposition parameters.
Tait's Rule	Geometrical formula relating flux incidence angle and the column inclination angle under conditions of limited surface diffusion and collimated flux. Reasonable guide for most materials deposited at $\alpha>60°$.
Tangent Rule	Empirically derived expression relating the flux incidence angle and the column inclination angle. Reasonable guide for most materials deposited at $\alpha<60°$.
TEM	Transmission Electron Microscopy
VFIGS	Virtual Film Growth System – Three-dimensional simulator developed to enable large-scale 3D simulation on a low-cost personal computer.
XRD	X-Ray Diffraction

Appendix B – List of Publications

B.1 REFERRED JOURNAL PUBLICATIONS

1. **B. Dick**, M.J. Brett, T. Smy, "Controlled Growth of Periodic Pillars by Glancing Angle Deposition"; J. Vac. Sci. Technol. B **21**, 23 (2003).
2. **B. Dick**, M.J. Brett, T.J. Smy, M. Belov, M.R. Freeman, "Periodic Sub-Micron Structures by Sputtering"; J. Vac. Sci. Technol. B **19**, 1813 (2001).
3. M. Seto, **B. Dick**, M.J. Brett, "Microsprings and microcantilevers: studies of mechanical response"; J. Micromech. Microeng. **11**, 582 (2001)
4. **B. Dick**, J.C. Sit, M.J. Brett, I.M.N.Votte, C.W.M. Bastiaansen, "Embossed Polymeric Relief Structures as a Template for the Growth of Periodic Inorganic Microstructures"; Nanolett. **1**, 71 (2001).
5. **B. Dick**, M.J. Brett, T. J. Smy, M. Malac, R.F. Egerton, "Periodic Magnetic Microstructures Produced by Glancing Angle Deposition"; J. Vac. Sci. Technol. A **18**, 1838 (2000).
6. M. Malac, R.F. Egerton, M.J. Brett, **B. Dick**, "Fabrication of Submicrometer Regular Arrays of Pillars and Helices"; J. Vac. Sci. Technol. B **17**, 2671 (1999).

B.2 CONFERENCE PROCEEDINGS/SUBMITTED ARTICLES TO REFEREED JOURNALS

1. **B. Dick**, M.J. Brett, T. Smy, "Effect of Substrate Rotation on the Growth of Microstructures at Glancing Incidence"; Submitted to JVST B (Feb/03).
2. **B. Dick**, M.J. Brett, "NanoFabrication by Glancing Angle Deposition"; Requested chapter submission to the *Encyclopedia of Nanoscience and Nanotechnology* (Oct/02).
3. M. Seto, **B. Dick**, M.J. Brett, "Nanoindentation of Microspring Thin Films"; MRS Proceedings **657**, EE5.15.1 (2001).
4. D. Vick, T.J. Smy, **B. Dick**, S.R. Kennedy, M.J. Brett, "Growth Behaviour of Engineered Porous Thin Films - Measurement and Modeling"; MRS Proceedings **648**, P3.43.1 (2001).

B.3 CONFERENCE PRESENTATIONS

1. **B. Dick**, M.J. Brett, T.J. Smy, "Growth Mechanics Affecting Films Deposited At Glancing Incidence"; Poster, MRS Conference in Boston, MA (Dec/02)
2. **B. Dick**, M.J. Brett, T.J. Smy, "Sculptured Thin Films Grown by Glancing Angle Deposition"; Poster, Frontiers to Integration in Edmonton, AB (Oct/02)
3. **B. Dick**, M.J. Brett, T.J. Smy, "Sculptured Thin Films Grown by Glancing Angle Deposition"; Poster, NanoTech 2002 in Houston, TX (Sept/02)
4. **B. Dick**, D. Vick, M.J. Brett, T.J. Smy, "Engineering of Porous Thin Films by Modification of Substrate Topography"; Poster, AVS 48th Ann. Int'l Symp. in San Francisco, CA (Oct/01)
5. **B. Dick**, D. Vick, M.J. Brett, T. J. Smy, "Periodic Sub-Micron Structures by Sputtering and Evaporation"; Poster, Canadian Semiconductor Conference in Ottawa, Ont (Aug/01)
6. D. Vick, T. Smy, **B.Dick**, S.R. Kennedy, M.J. Brett, "Growth Behaviour of Engineered Porous Thin Films - Measurement and Modelling"; Poster, MRS Conference in Boston, MA (Nov/00)
7. **B. Dick**, M.J. Brett, T.J. Smy, M. Belov, M.R. Freeman, "Sputtered Fabrication of Periodic Sub-Micron Structures"; Oral, AVS 47th Ann. Int'l Symp. in Boston, MA (Oct/00)
8. **B. Dick**, M.J. Brett, T.J. Smy, M. Malac, R.F. Egerton, T. Smy, "Periodic Magnetic Microstructures using Glancing Angle Deposition"; Oral, AVS 46th Ann. Int'l Symp. in Seattle, WA (Oct/99)
9. **B. Dick**, M.J. Brett, M. Aktary, M.T. McDermott "Fabrication of Magnetic Microstructures by Glancing Angle Deposition"; Oral, MRS Conference in San Francisco, CA (Apr/99)

B.4 OTHER PUBLICATIONS

1. **B. Dick**, *The Radio Access Unit (RAU) Test Software Suite,* School of Engineering Science, Simon Fraser University, Canada, 1997

References

[1] M. Ohring, *The Materials Science of Thin Films*, 2nd ed. Toronto, Ont: Academic Press, 2002.
[2] E. D. Nicholson, *Gold Bull*, **12**, 161, (1979).
[3] M. Faraday, *Phil. Trans. Roy. Soc. Lond.*, **147**, 145, (1857).
[4] K. Robbie, L. J. Friedrich, S. K. Dew, T. Smy, and M. J. Brett, *J. Vac. Sci. Technol. A.*, **13**, 1032, (1995).
[5] K. Robbie, "Glancing Angle Deposition", Ph.D Thesis, University of Alberta: Edmonton (1998).
[6] K. Robbie and M. J. Brett, US Patent #5,866,204 (1999).
[7] K. Robbie and M. J. Brett, US Patent #6,248,422 (2001).
[8] B. Dick, M. J. Brett, T. Smy, M. R. Freeman, M. Malac, and R. F. Egerton, *J. Vac. Sci. Technol. A.*, **18**, 1838, (2000).
[9] F. Liu, M. T. Umlor, L. Shen, J. Weston, W. Eads, J. Barnard, and G. J. Mankey, *J. Appl. Phys.*, **85**, 5486, (1999).
[10] F. Liu, C. Yu, L. Shen, J. Barnard, and G. J. Mankey, *IEEE Trans. Mag.*, **36**, 2939, (2000).
[11] S. Kennedy, M. J. Brett, O. Toader, and S. John, *Nanolett.*, **2**, 59, (2002).
[12] J. C. Sit, S. Kennedy, D. J. Broer, and M. J. Brett, *Proc. SPIE*, **4107**, 133, (2000).
[13] J. C. Sit, "Thin Film/Liquid Crystal Composite Optical Materials and Devices", Ph.D Thesis, University of Alberta: Edmonton (2002).
[14] K. D. Harris, A. Huizinga, and M. J. Brett, *Electrochem. Solid-State Lett.*, **5**, H27, (2002).
[15] K. D. Harris, J. R. McBride, K. E. Nietering, and M. J. Brett, *Sens. Mat.*, **13**, 225, (2001).
[16] K. D. Harris, D. Vick, E. J. Gonzalez, T. Smy, K. Robbie, and M. J. Brett, *Surf. Coat. Technol.*, **138**, 185, (2001).
[17] M. Seto, B. Dick, and M. J. Brett, *J. Micromech. Microeng.*, **11**, 582, (2001).
[18] M. J. Colgan, D. Vick, and M. J. Brett, *Mat. Res. Soc. Proc.*, **636**, D9.24.1, (2001).
[19] D. Vick, T. Smy, and M. J. Brett, *J. Mat. Res.*, **17**, 2904, (2002).
[20] C. Tang, S. Alexander, and R. Bruinsma, *Physical Review Letters*, **64**, 772, (1990).
[21] G. S. Bales, R. Bruinsma, E. A. Eklund, R. P. U. Karunasiri, J. Rudnick, and A. Zangwill, *Science*, **249**, 264, (1990).
[22] J. M. Nieuwenhuizen and H. B. Haanstra, *Phil. Tech. Rev.*, **27**, 87, (1966).
[23] R. W. Vook, *Int. Metals Rev.*, **27**, 209, (1982).
[24] D. W. Pashley and M. J. Stowell, *J. Vac. Sci. Technol.*, **3**, 156, (1966).
[25] B. A. Movchan and A. V. Demchishin, *Phys. Met. Metallogr.*, **28**, (1969).
[26] J. A. Thornton, *Ann. Rev. Materi. Sci.*, **7**, 239, (1977).
[27] T. G. Knorr and R. W. Hoffman, *Phys. Rev.*, **113**, 1039, (1959).
[28] D. O. Smith, *J. Appl. Phys.*, **30**, 264S, (1959).
[29] D. O. Smith, M. S. Cohen, and G. P. Weiss, *J. Appl. Phys.*, **31**, 1755, (1960).
[30] R. N. Tait, T. Smy, and M. J. Brett, *Thin Solid Films*, **226**, 196, (1993).

[31] H. J. Leamy, G. H. Gilmer, and A. G. Dirks, "The Microstructure of Vapour Deposited Thin Films," in *Current Topics in Materials Science*, vol. 6, E. Kaldis, Ed.: North-Holland Publishing Company, 1980, pp. 309.

[32] A. G. Dirks and H. J. Leamy, *Thin Solid Films*, **47**, 219, (1977).

[33] L. Abelmann and C. Lodder, *Thin Solid Films*, **305**, 1, (1997).

[34] R. Messier, T. Gehrke, C. Frankel, V. C. Venugopal, W. Otano, and A. Lakhtakia, *J. Vac. Sci. Technol. A.*, **15**, 2148, (1997).

[35] L. Holland, *J. Opt. Soc.*, **43**, 376, (1953).

[36] M. S. Cohen, *J. Appl. Phys.*, **32**, 87S, (1961).

[37] I. Hodgkinson, Q. H. Wu, and A. McPhun, *J. Vac. Sci. Technol. B.*, **16**, 2811, (1998).

[38] R. Fiedler and G. Schirmer, *Thin Solid Films*, **167**, 281, (1988).

[39] N. O. Young and J. Kowal, *Nature*, **183**, 104, (1959).

[40] T. Motohiro and Y. Taga, *Appl. Opt.*, **28**, 2466, (1989).

[41] A. Lakhtakia and R. Messier, *Opt. Eng.*, **33**, 2529, (1994).

[42] R. Azzam, *Appl. Phys. Lett.*, **61**, 3118, (1992).

[43] A. Lakhtakia and W. S. Weiglhofer, *Proc. Roy. Soc. Lond.*, **A448**, 419, (1995).

[44] A. Lakhtakia, R. Messier, M. J. Brett, and K. Robbie, *Innov. Mat. Res.*, **1**, 165, (1996).

[45] O. R. Monteiro, A. Vizar, and I. G. Brown, *J. Phys. D: Appl. Phys.*, **31**, 3188, (1998).

[46] G. Y. Slepyan and A. S. Maksimenko, *Opt. Eng.*, **37**, 2843, (1998).

[47] A. Lakhtakia and R. Messier, *Optics & Photonics News*, 27, (2001).

[48] M. J. Brett, S. K. Dew, and T. J. Smy, *Thin Films*, **22**, 1, (1996).

[49] T. Smy, S. K. Dew, D. A. Tilroe, T. A. Janacek, N. Behzad, and G. Whyte, (1996).

[50] R. N. Tait, S. K. Dew, T. Smy, and M. J. Brett, *J. Appl. Phys.*, **70**, 4295, (1991).

[51] K. Robbie, M. J. Brett, and A. Lakhtakia, *J. Vac. Sci. Technol. A.*, **13**, 2991, (1995).

[52] K. Robbie, C. Shafai, and M. J. Brett, *J. Mat. Res.*, **14**, 3158, (1999).

[53] K. Robbie, J. C. Sit, and M. J. Brett, *J. Vac. Sci. Technol. B.*, **16**, 1115, (1998).

[54] R. Messier, V. C. Venugopal, and P. D. Sunal, *J. Vac. Sci. Technol. A.*, **18**, 1538, (2000).

[55] K. Robbie and M. J. Brett, *J. Vac. Sci. Technol. A.*, **15**, 1460, (1997).

[56] K. D. Harris, D. Vick, M. J. Brett, and K. Robbie, *Mat. Res. Soc. Proc.*, **555**, 97, (1999).

[57] M. Suzuki and Y. Taga, *Jap. J. Appl. Phys.*, **40**, L358, (2001).

[58] O. Toader and S. John, *Science*, **292**, 1133, (2001).

[59] S. John, *Phys. Rev. Lett.*, **58**, 2486, (1987).

[60] E. Yablonovitch, *Phys. Rev. Lett.*, **58**, 2059, (1987).

[61] S. John, O. Toader, and K. Busch, *Encyclopedia of Physical Science and Technology*, **12**, 133, (2002).

[62] S. Y. Chou, *Proc. IEEE*, **85**, 652, (1997).

[63] M. Malac, R. F. Egerton, M. J. Brett, and B. Dick, *J. Vac. Sci. Technol. B.*, **17**, 2671, (1999).

[64] B. Dick, J. C. Sit, M. J. Brett, I. M. N. Votte, and C. W. M. Bastiaansen, *Nanolett.*, **1**, 71, (2001).

[65] T. A. Savas, F. Farhoud, H. I. Smith, M. Hwang, and C. A. Ross, *J. Appl. Phys.*, **85**, 6160, (1999).

[66] K. Hara, *J. Sci. Hiroshima Univ.*, **Ser A-II**, 139, (1970).

[67] K. Hara, M. Kamiya, T. Hashimoto, K. Okamoto, and H. Fujiwara, *J. Mag. Mag. Mater.*, **73**, 161, (1988).

[68] S. Lichter and J. Chen, *Phys. Rev. Lett.*, **56**, 1396, (1986).

[69] J. B. Bindell and T. C. Tisone, *Thin Solid Films*, **23**, 31, (1974).

[70] G. S. Bales and A. Zangwill, *J. Vac. Sci. Technol. A.*, **9**, 145, (1991).

[71] R. Messier, A. Lakhtakia, V. C. Venugopal, and P. D. Sunal, *Vac. Technol. & Coat.*, 40, (2001).

[72] P. Meakin, *Phys. Rev.*, **A38**, 994, (1988).

[73] D. Henderson, M. H. Brodsky, and P. Chaudhari, *Appl. Phys. Lett.*, **25**, 641, (1974).

[74] T. Smy, D. Vick, M. J. Brett, S. K. Dew, A. T. Wu, J. C. Sit, and K. D. Harris, *J. Vac. Sci. Technol. A.*, **18**, 2507, (2000).

[75] M. Suzuki and Y. Taga, *J. Appl. Phys.*, **90**, 5599, (2001).

[76] R. N. Tait, T. Smy, and M. J. Brett, *J. Vac. Sci. Technol. A.*, **10**, 1518, (1992).

[77] M. J. Brett and S. K. Dew, *Thin Films*, **22**, (1996).

[78] M. Gesley, *J. Appl. Phys.*, **65**, (1989).

[79] Y. Ochiai, Y. Kojima, and S. Matsui, *J. Vac. Sci. Technol. B.*, **6**, (1988).

[80] S. A. Campbell, *The Science and Engineering of Microelectronic Fabrication*. New York: Oxford University Press, 1996.

[81] L. I. Maissel and R. Glang, *Handbook of Thin Film Technology*. Toronto, Ont: McGraw-Hill Book Company, 1970.

[82] E. H. Anderson, K. Komatsu, and H. I. Smith, *J. Vac. Sci. Technol. B.*, **6**, 216, (1987).

[83] T. A. Savas, S. N. Shah, M. L. Scattenburg, J. M. Carter, and H. I. Smith, *J. Vac. Sci. Technol. B.*, **13**, 2732, (1995).

[84] E. H. Anderson, H. I. Smith, and M. L. Schattenburg, US Patent (1991).

[85] F. Rousseaux, D. Decanini, F. Carcenac, E. Cambril, M. F. Ravet, C. Chappert, N. Bardou, B. Bartenlian, and P. Veillet, *J. Vac. Sci. Technol. B.*, **13**, 2787, (1995).

[86] X. Bao, F. Li, and R. M. Metzger, *J. Appl. Phys.*, **1996**, 4866, (1996).

[87] G. Zangari and D. N. Lambeth, *IEEE Trans. Mag.*, **33**, 3010, (1997).

[88] W. Xu, J. Wong, C. C. Cheng, R. Johnson, and A. Scherer, *J. Vac. Sci. Technol. B.*, **13**, 2372, (1995).

[89] P. R. Krauss, P. B. Fisher, and S. Y. Chou, *J. Vac. Sci. Technol. B.*, **12**, 3639, (1994).

[90] S. Y. Chou, P. R. Krauss, and P. J. Renstrom, *Appl. Phys. Lett.*, **67**, 3114, (1995).

[91] S. Y. Chou, P. R. Krauss, and P. J. Renstrom, *Science*, **272**, 85, (1996).

[92] B. Cui, W. Wu, L. Kong, X. Sun, and S. Y. Chou, *J. Appl. Phys.*, **85**, 5534, (1999).

[93] C. A. Ross, H. I. Smith, T. A. Savas, M. Schattenburg, M. Farhoud, M. Hwang, M. Walsh, M. C. Abraham, and R. J. Ram, *J. Vac. Sci. Technol. B.*, **17**, 3168, (1999).

[94] R. F. Egerton and L. Wan, *Journal of Microscopy*, **191**, 113, (1998).

[95] K. Y. Lee, N. LaBianca, S. A. Rishton, S. Zoghamain, J. D. Gelorme, J. Shaw, and T. H.-P. Chang, *J. Vac. Sci. Technol. B.*, **13**, 3012, (1995).

[96] W. H. Wong and E. Y. B. Pun, *J. Vac. Sci. Technol. B.*, **19**, 732, (2001).

[97] M. Aktary, K. L. Westra, M. O. Jensen, M. J. Brett, and M. R. Freeman, *Submitted to JVST B (Oct/02)*).

[98] M. Malac and R. F. Egerton, *J. Vac. Sci. Technol. A.*, **19**, 158, (2001).

[99] A. van der Drift, *Phil. Res. Rep.*, **22**, 267, (1967).

[100] *Private communication with Mary Seto*

[101] K. D. Harris, D. Vick, T. Smy, and M. J. Brett, *J. Vac. Sci. Technol. A.*, **20**, 1, (2002).

[102] B. Dick, M. J. Brett, and T. Smy, *J. Vac. Sci. Technol. B.*, (In Press (2003)).

[103] B. A. Orlowski, W. E. Spicer, and A. D. Baer, *Thin Solid Films*, **34**, 31, (1976).

[104] J. N. Broughton and M. J. Brett, *Electrochem. Solid-State Lett.*, **5**, A279, (2002).

[105] K. Robbie, M. J. Brett, and A. Lakhtakia, *Nature*, **384**, 616, (1996).

[106] M. Malac and R. F. Egerton, *Nanotech.*, **12**, 11, (2001).

[107] *Quoted from www.webelements.com*

[108] E. Bauer, "Growth of Oriented Films on Amorphous Surfaces," in *Single Crystal Films*, M. H. Francombe and H. Sato, Eds. Oxford: Pergamon, 1964, pp. 43.

[109] C. Zhu, S. Misawa, and S. Tsukahara, *Surface Science*, **325**, 279, (1995).

[110] A. W. Fortuin, P. F. A. Alkemade, A. H. Verbruggen, A. J. Steinfort, H. Zandbergen, and S. Radelaar, *Surface Science*, **366**, 285, (1996).

[111] N. Thangaraj, K. H. Westmacott, and U. Dahmen, *Appl. Phys. Lett.*, **61**, 913, (1992).

[112] M. Sosnowski, S. Ramac, W. L. Brown, and Y. O. Kim, *Appl. Phys. Lett.*, **65**, 2943, (1994).

[113] M.-A. Hasan, G. Radnoczi, J.-E. Sundgren, and G. V. Hansson, *Surface Science*, **236**, 53, (1990).

[114] A. Tanaka, M. Hatano, K. Takahashi, H. Sasaki, S. Suzuki, and S. Sato, *Surface Science*, **433-435**, 647, (1999).

[115] *Private communication with Dr. Arthur Mar*

[116] R. Messier and J. E. Yehoda, *J. Appl. Phys.*, **58**, 3739, (1985).

[117] R. P. U. Karunsiri, R. Bruinsma, and J. Rudnick, *Phys. Rev. Lett.*, **62**, 788, (1989).

[118] M. Malac, R. F. Egerton, and M. J. Brett, *Vac. Technol. & Coat.*, 48, (2001).

[119] D. Vick, T. Smy, B. Dick, S. Kennedy, and M. J. Brett, *Mat. Res. Soc. Proc.*, **648**, P3.43.1, (2001).

[120] *Private communcation with Dr. Doug Vick*

[121] J. C. Sit, D. Vick, K. Robbie, and M. J. Brett, *J. Mat. Res.*, **14**, 1197, (1999).

[122] S. K. Dew, T. Smy, and M. J. Brett, *Japanese Journal of Applied Physics*, **33**, 1140, (1994).

[123] R. N. Tait, S. K. Dew, W. Tsai, D. Hodul, T. Smy, and M. J. Brett, *J. Vac. Sci. Technol. B.*, **14**, 679, (1996).

[124] S. M. Rossnagel, D. Mikalsen, H. Kinoshita, and J. J. Cuomo, *J. Vac. Sci. Technol. A.*, **9**, 261, (1991).

[125] S. M. Rossnagel and J. Hopwood, *Appl. Phys. Lett.*, **63**, 3285, (1993).

[126] J. N. Broughton, M. J. Brett, S. K. Dew, and G. Este, *IEEE Trans. Semicond. Manu.*, **9**, 122, (1996).

[127] J. C. Sit, D. J. Broer, and M. J. Brett, *Liq. Cryst.*, **27**, 387, (2000).

[128] J. C. Sit, D. J. Broer, and M. J. Brett, *Adv. Mat.*, **12**, 371, (2000).

[129] S. Kennedy, J. C. Sit, D. J. Broer, and M. J. Brett, *Liq. Cryst.*, **28**, 1799, (2001).

[130] I. Hodgkinson, Q. Wu, A. Lakhtakia, and K. Robbie, *Appl. Opt.*, **39**, 642, (2000).

[131] K. Robbie, A. J. P. Hnatiw, M. J. Brett, R. I. MacDonald, and J. N. McMullin, *Elect. Lett.*, **33**, 1213, (1997).

[132] A. Y. Elezzabi, J. C. Sit, J. F. Holzman, K. Robbie, and M. J. Brett, *Elect. Lett.*, **35**, 1, (1999).

[133] A. T. Wu and M. J. Brett, *Sens. Mat.*, **13**, 399, (2001).

[134] M. Suzuki, T. Ito, and Y. Taga, *Appl. Phys. Lett.*, **78**, 3968, (2001).

[135] K. D. Harris, M. J. Brett, T. Smy, and C. Backhouse, *J. Electrochem. Soc.*, **147**, 2002, (2000).

[136] K. Fluri, G. Fitzpatrick, N. Chiem, and D. J. Harrison, *Anal. Chem.*, **68**, 4285, (1996).

[137] R. White, R. New, and R. Pease, *IEEE Trans. Mag.*, **33**, (1997).

[138] J. C. Mallinson, *The Foundation of Magnetic Recording*, 2nd ed. Toronto: Academic Press, 1993.

[139] J. Judy, "Fundamentals of Magnetic Materials (Short Course)," presented at American Vacuum Society, 1995.

[140] J. S. Gau, *J. Mag. Mag. Mater.*, **80**, (1989).

[141] T. C. Arnoldussen, *Magnetic Recording Technology, 2nd Edition (Chapter 4)*. Toronto: McGraw-Hill, 1996.

[142] Y. Shiroishi, Y. Hoscoe, A. Ishikawa, Y. Yahisa, Y. Sugita, H. Suzuki, T. Ohno, and M. Ohura, *J. Appl. Phys.*, **73**, 5569, (1993).

[143] *Private communication with Dr. Ken Harris*

[144] *Quoted from www-916.ibm.com/press/prnews.nsf/print/ F8DE74C08688375E85256A5300483B8F*

[145] P. Vettiger, G. Cross, M. Despont, U. Drechsler, U. Durig, B. Gotsmann, W. Haberle, M. A. Lantz, H. E. Rothuizen, R. Stutz, and G. K. Binnig, *IEEE Trans. Nanotech.*, **1**, 39, (2002).

[146] M.-H. Wu and G. M. Whitesides, *Appl. Phys. Lett.*, **78**, 2273, (2001).

[147] M. Farhoud, M. Hwang, H. I. Smith, M. Schattenburg, J. M. Bae, K. Youcef-Toumi, and C. A. Ross, *IEEE Trans. Mag.*, **34**, 1087, (1998).

[148] J. P. Spallas, A. M. Hawryluk, and D. R. Kania, *J. Vac. Sci. Technol. B.*, **13**, 1973, (1995).

[149] C. O. Bozler, C. T. Harris, S. Rabe, D. D. Rathman, M. A. Hollis, and H. I. Smith, *J. Vac. Sci. Technol. B.*, **12**, 629, (1993).

[150] M. Schattenburg, C. Chen, P. N. Everett, J. Ferrera, P. Konkola, and H. I. Smith, *J. Vac. Sci. Technol. B.*, **17**, 2692, (1999).